Ground Station Reception System for LEO Incoming Signal

Felipe Rodrigues Sobrinho

DISSERTAÇÃO DE MESTRADO

DEPARTAMENTO DE ENGENHARIA ELÉTRICA

UNIVERSIDADE DE BRASÍLIA

FACULDADE DE TECNOLOGIA

Universidade de Brasília
Faculdade de Tecnologia
Departamento de Engenharia Elétrica

Ground Station Reception System for LEO Incoming Signal

Felipe Rodrigues Sobrinho

DISSERTAÇÃO DE MESTRADO SUBMETIDA AO PROGRAMA DE PÓS-GRADUAÇÃO EM ENGENHARIA ELÉTRICA DA UNIVERSIDADE DE BRASÍLIA COMO PARTE DOS REQUISITOS NECESSÁRIOS PARA A OBTENÇÃO DO GRAU DE MESTRE.

APROVADA POR:

Prof. Sébastien Roland Marie Joseph Rondineau, D.Sc. (ENE-UnB)
(Orientador)

Prof. Gefeson Mendes Pacheco, D.Sc. (ITA)
(Examinador Externo)

Prof. Adoniran Judson de Barros Braga, D.Sc. (ENE-UnB)
(Examinador Interno)

Publicação: PPGEE.DM 834/25

Brasília/DF, 30 de Setembro de 2025.

FICHA CATALOGRÁFICA

SOBRINHO, FELIPE RODRIGUES

Ground Station Reception System for LEO Incoming Signal . [Distrito Federal] 2025.

x, 93 p., 210 x 297 mm (ENE/FT/UnB, Mestre, Dissertação de Mestrado, 2025).

Universidade de Brasília, Faculdade de Tecnologia, Departamento de Engenharia Elétrica.

Departamento de Engenharia Elétrica

1. RF Systems
2. Satellite Communications
3. Antenna
4. Quad-Ridge Antenna
5. Feed Horn
6. Array Calibration
7. RF Front-end
8. Receiver Synchronization

I. ENE/FT/UnB
II. Título (série)

REFERÊNCIA BIBLIOGRÁFICA

SOBRINHO, F. R. (2025). Ground Station Reception System for LEO Incoming Signal . Dissertação de Mestrado em Engenharia Elétrica, Publicação PPGEE.DM-834/25, Departamento de Engenharia Elétrica, Universidade de Brasília, Brasília, DF, 113 p.

CESSÃO DE DIREITOS

AUTOR: Felipe Rodrigues Sobrinho

TÍTULO: Ground Station Reception System for LEO Incoming Signal .

GRAU: Mestre ANO: 2025

Felipe Rodrigues Sobrinho

Universidade de Brasília (UnB)

Campus Darcy Ribeiro

Faculdade de Tecnologia - FT

Departamento de Eng. Elétrica (ENE)

Brasília - DF CEP 70919-970

To my beloved family.

Acknowledgements

I would like to express my most sincere gratitude to the many individuals whose support and guidance were instrumental in the completion of this dissertation.

First, my deepest gratitude goes to my advisor, Professor Sébastien. Thank you for your invaluable guidance throughout this project, for your patience, and for the wisdom that shaped this research.

I owe a special debt of gratitude to my family for their unconditional love and support in all moments of my life.

To my brothers, Gabriel Williams and Lucas Pinheiro, thank you for all the fruitful discussions, invaluable help, and the happy moments we shared.

My thanks extend to my laboratory colleagues for the constant partnership and for making the daily journey lighter and more enjoyable.

I am grateful to all my professors, whose teaching and mentorship guided me and revealed the enormous possibilities that academic life can provide.

My sincere thanks also go to LABMET at UFCG for hosting me and for their assistance with the antenna measurements.

You are all forever in my memory.

Abstract

The growing demand for LEO satellite communication necessitates the development of low-cost, high-performance ground stations. This dissertation addresses this need by presenting the comprehensive design, validation, and calibration of the key components for a reconfigurable phased array system. The work details a two-stage development of a broadband, dual-polarized quad-ridge horn feed. An initial square prototype highlighted significant manufacturing challenges, leading to a novel modular and tunable conical horn design that has been successfully fabricated and validated through measurements, achieving a 63 % fractional bandwidth and 10.1 dBi peak gain. The complete system architecture, comprising individual RF front-ends and SDRs for each of the 16 array elements, has been designed and simulated. A detailed link budget analysis confirmed a positive link margin of over 3 dB for the target VCUB1 satellite, while the proposed synchronization scheme using distributed GPSDOs has been experimentally verified to ensure array coherence. To address real-world non-idealities, a robust two-stage calibration algorithm has been developed and validated in simulation. The algorithm first corrects for physical antenna position errors using a practical method based on the Euclidean Distance Matrix, and then compensates for gain and phase imbalances in the RF channels using a minimal number of pilot signals. Simulations confirmed the algorithm effectiveness, achieving a low RMSE (<-30 dB) between the calibrated and ideal array responses. Collectively, this research provides a validated, novel and manufacturable antenna to a complete system architecture and effective calibration strategies—for the development of next-generation, low-cost phased array ground stations for LEO satellite communication.

Keywords: RF Systems, Satellite Communications, Antenna, Quad-Ridge Antenna, Feed Horn, Array Calibration, RF Front-end, Receiver Synchronization

Resumo Estendido

Título: Sistema de Recepção de uma Estação de Base para Sinais de Satélites LEO.

Autor: Felipe Rodrigues Sobrinho

Orientador: Prof. Dr. Sébastien Roland Marie Joseph Rondineau

Programa de Pós-Graduação em Engenharia Elétrica, 30 de Novembro de 2025.

A crescente demanda por comunicação via satélites de baixa órbita (LEO) impulsiona a necessidade de estações terrenas de baixo custo, alta performance e reconfiguráveis. As tradicionais estações, baseadas em grandes refletores parabólicos com sistemas de apontamento mecânico, possuem um custo elevado de implementação e manutenção, além de limitações na capacidade de rastrear múltiplos satélites simultaneamente. Como alternativa, os arranjos de antenas em fase (*phased arrays*) oferecem vantagens significativas, como o apontamento eletrônico do feixe, interferometria do sinal e a possibilidade de comunicação com múltiplos satélites. Esta dissertação aborda este desafio através do projeto, caracterização e desenvolvimento de metodologias de calibração de uma estação terrena baseada em um arranjo de antenas em fase, com foco em soluções de baixo custo e reconfigurabilidade. O trabalho está fundamentado em três pilares principais: o desenvolvimento de uma antena alimentadora de corneta de *quad-ridge* (*quad-ridge horn*) de banda larga e dupla polarização, o projeto de um *front-end* de RF e arquitetura do sistema de recepção, e a implementação de algoritmos de calibração para corrigir as não idealidades do arranjo. Além disso é parte do projeto Estação Terrena Autônoma Distribuída de Baixo Custo e Alta Taxa de Download, Processo CNPq: 405635/2022-2, CHAMADA CNPq Nº 20/2022 - Faixa A, sob coordenação do Prof. Sébastien Roland Marie Joseph Rondineau.

O primeiro esforço prático deste trabalho concentrou-se no desenvolvimento da corneta alimentadora. O protótipo inicial, uma Antena Corneta Quadrada *Quad-Ridge* (SQRA), foi projetado, fabricado e testado com foco na frequência central de 2.445 GHz do satélite VCUB1 da Visiona. Embora funcional, este primeiro modelo revelou desafios relacionados à fabricação

com chapas metálicas, que resultaram em imprecisões dimensionais e, portanto, desvios no desempenho elétrico. Além disso, seu grande tamanho e peso foram considerados inadequados para a aplicação como alimentador de um refletor parabólico de 2.4 m, pois gerariam uma região de sombreamento no refletor, degradando a eficiência total da antena.

Com base na experiência do primeiro protótipo, uma antena corneta cônica *quad-ridge* foi desenvolvida, com foco em modularidade, compactação e, principalmente, ajuste pós-fabricação. O projeto incorporou três inovações chave: uma montagem modular que simplifica a fabricação e manutenção; um alimentador quadraxial para excitação diferencial, melhorando a imunidade a ruído; e um mecanismo de ajuste do posicionamento dos *ridges*. Este último, realizado através de ranhuras usinadas e parafusos de ajuste para os *ridges*, permitiu relaxar as tolerâncias de fabricação e possibilitou uma sintonia fina das propriedades elétricas da antena mesmo após sua montagem completa. Esta capacidade de reconfiguração mecânica é uma das principais contribuições deste trabalho, em conjunto com a alimentação diferencial quadraxial, pois aborda um dos maiores desafios na fabricação de antenas de banda larga e com tolerâncias estreitas.

O sucesso do projeto da corneta cônica foi validado através da sua fabricação e de um rigoroso processo de medição em câmara anecoica. Os resultados experimentais demonstraram um excelente desempenho, superando as metas de projeto. A antena alcançou uma largura de banda fracionária de 63% (de 2.1 GHz a 3.9 GHz), com uma perda de retorno medida inferior a -13 dB e um ganho de pico de 10.1 dBi em 2.2 GHz. A excelente concordância entre os resultados medidos e simulados validou não apenas o modelo eletromagnético, mas também a eficácia do método de fabricação e ajuste proposto. Concluiu-se, portanto, que a antena cônica modular e ajustável é perfeitamente adequada para sua função como alimentador no arranjo de antenas parabólicas.

Paralelamente ao desenvolvimento das antenas, a arquitetura completa do sistema de recepção foi concebida. O sistema consiste em um arranjo de 16 refletores parabólicos, cada um equipado com seu próprio *front-end* de RF e um Rádio Definido por Software (SDR) para digitalização do sinal. A transmissão dos dados de cada antena para o *cluster* computacional central é realizada via fibra óptica, garantindo alta velocidade e imunidade a interferências. O *front-end* de RF foi projetado e simulado detalhadamente no software Cadence AWR em nível de sistema, com a seleção de componentes de baixo ruído. As simulações demonstraram que a cadeia de RF atende aos requisitos críticos de figura de ruído (inferior a 2.65 dB) e linearidade,

essenciais para a recepção de sinais de baixa potência de satélite.

Dois aspectos críticos a nível de sistema foram validados: a viabilidade do link de comunicação e a sincronização do arranjo. Foi realizada uma análise detalhada do *Link Budget* para o satélite alvo, o VCUB1, que confirmou a robustez do projeto ao apresentar uma margem de link positiva de 3.07 dB. Este resultado garante que o sistema pode receber os dados do satélite com sucesso sob as condições de operação especificadas. Além disso, a sincronização de tempo e *clock* entre os múltiplos SDRs distribuídos fisicamente foi abordada através do uso de Osciladores Disciplinados por GPS (GPSDOs) em cada antena. Testes experimentais validaram esta abordagem, mostrando que os GPSDOs corrigem eficazmente os desvios dos osciladores internos dos SDRs, mantendo a coerência de fase em todo o arranjo.

Para corrigir os desvios de implementação real do sistema, uma metodologia de calibração em duas etapas foi desenvolvida e simulada. A primeira etapa aborda os erros de posicionamento físico das antenas, um problema comum em instalações de campo. Foi proposto um algoritmo prático baseado na Matriz de Distâncias Euclidianas (EDM), que utiliza medições de distância entre as antenas para estimar e corrigir seus verdadeiros posicionamentos. As simulações mostraram que este método é altamente preciso, alcançando um erro de estimação de apenas 0.25% para um desvio padrão de 20 cm nas medições. Esta etapa é fundamental para desacoplar os erros mecânicos dos eletrônicos, simplificando a calibração subsequente.

A segunda etapa da calibração foca nos desbalanços de ganho e fase dos canais de RF individuais. Foi desenvolvido um método que utiliza uma matriz de calibração global, estimada a partir de apenas dois sinais pilotos (sinais de calibração) com direções de chegada conhecidas. Esta abordagem é significativamente mais prática para aplicações de campo do que os métodos que exigem uma grade densa de pontos de calibração. As simulações confirmaram a alta eficácia do algoritmo, que alcançou um Erro Quadrático Médio (RMSE) entre o vetor de direção ideal e o calibrado inferior a -30 dB. Em conjunto, este trabalho apresenta um projeto completo e validado, que abrange desde a fabricação de hardware até o desenvolvimento de algoritmos de calibração, fornecendo um roteiro para a criação de estações terrenas de arranjo de fase de baixo custo e alto desempenho para a comunicação com satélites LEO.

Contents

Table of contents i

List of Figures iv

List of Symbols vii

List of Abbreviations viii

Glossary x

1 Introduction 1

1.1 State-of-the-art 1

1.2 Contextualization 1

1.3 Main Objectives 2

1.4 Organization of this work 3

2 Theoretical Foundation 4

2.1 Antenna Parameters 4

2.1.1 Energy Flux and Radiating Intensity 4

2.1.2 Directivity, Gain and Beamwidth 6

2.2 Radiation from apertures 9

2.3 Quad-ridge Horn Antennas. 11

2.4 Parabolic Reflectors 13

2.5 Satellite communications 15

2.5.1 Satellite Specifications 15

2.5.2 Link budget . . . 15
2.5.3 Antenna Noise Temperature . . . 16
2.5.4 System Noise Temperature . . . 17
2.6 Antenna arrays . . . 19

3 Quad-Ridge Feed Horn 21

3.1 Square Quad-Ridge Horn Antenna . . . 22
3.1.1 Design Procedure . . . 22
3.1.2 Ridge waveguide characteristics . . . 23
3.1.3 Transition design . . . 24
3.1.4 Ridge Shape . . . 25
3.1.5 Complete simulation . . . 26
3.1.6 Yield Analysis . . . 27
3.1.7 Fabrication and Measurement . . . 29
3.2 Low-Cost Tunable Compact and Modular Broadband Dual-Polarization Conical Horn Antenna . . . 31
3.2.1 Design and Optimization . . . 31
3.2.2 Manufacturing . . . 34
3.2.3 Simulations and Measurements . . . 34
3.2.4 Simulated and Measured Results . . . 35

4 System Design 38

4.1 System Overview . . . 38
4.2 Link Budget Analysis . . . 39
4.3 RF front-end . . . 40
4.4 Software Defined Radio . . . 47

5 Array Calibration 50

5.1 System Model . . . 51
5.2 Array Calibration . . . 52
5.2.1 Position Correction . . . 52

5.2.2 Phase and Amplitude Correction 54
5.3 Simulation Results 54

6 Conclusion **57**

Appendix **59**

A Quad Ridge PCB Schematics **60**

References **71**

List of Figures

1.1 Aerial picture of the phased array mounted in this project. . . . 2

2.1 Reference polar and rectangular coordinate systems. . . . 5
2.2 Radiated power into solid angle dΩ. . . . 5
2.3 Example of two systems with the same EIRP, where (a) represents a system using an isotropic antenna and (b) a system using a directive antenna. . . . 7
2.4 Relationship between the transmitted power, P_T, and radiated power, P_{rad}. . . . 8
2.5 Field distribution on the aperture surface. . . . 10
2.6 Modal distribution in (a) quad-ridge square waveguides and in (b) quad-ridge circular waveguides. . . . 11
2.7 Modal behavior with the change of the width of the waveguide ridges, fixing the ridge height at 26 mm. . . . 12
2.8 Modal behavior with the change of the height of the waveguide ridges fixing the width at 8 mm. . . . 12
2.9 Parabolic reflector parameter. . . . 13
2.10 Link between antennas. . . . 15
2.11 Antenna receiving system. . . . 16
2.12 Device noise model. . . . 17
2.13 Noise in cascaded devices. . . . 18
2.14 Translational antenna array. . . . 19

3.1 Design of the quad-ridge horn antenna. . . . 22
3.2 Modes in the quad-ridge waveguide by excitation from a coaxial pin with 1 V 23
3.3 Propagation of modes in a square quad-ridge waveguide in function of frequency. . . . 23
3.4 Dimensions of the quad-ridge waveguide. The variables values are $W_{wg} = 40$ mm, $W_{gap} = 3.3$ mm, $W_1 = 6.35$ mm, $W_2 = 1.95$ mm, $L_{rd} = 16.15$ mm. . . . 24
3.5 Dimensions of the length and width of the backshort. . . . 25
3.6 The horn and ridge dimensions are $g = 3.3$ mm, $h_{wg} = 40$ mm, $R_A = 355$ mm, $A = 32$ mm. . . . 26
3.7 Simulated variation in S_{11} parameter in function of variation of the variable value. . . . 26
3.8 Polarization and cross polarization. . . . 27
3.9 Estimated variation in S_{11} parameter at 2.2 GHz as a function of variation of the variable value. . . . 29
3.10 Manufactured square quad-ridge horn antenna: (a) a diagonal view, and (b) a side view. . . . 29
3.11 Manufactured square quad ridge horn antenna: (a) a rear view, and (b) a side view. . . . 30

3.12 Measured S-parameters of the square quad-ridge horn. 30
3.13 Exploded view of the modular horn antenna. 31
3.14 Dimensions of the horn antenna in (a) the aluminium backplate design; (b) a detailed view of the throat section; (c) a transverse section cut of the antenna. In red is the ridge groove and in blue is the PTFE spacer. 32
3.15 Field distribution for 1 V of differential pair excitation in dB(V m^{-1}) inside the PCB cavity when (a) the cavity is guided and (b) when cavity is not guided by the aluminium backplate extruded paths. 33
3.16 Pictures of the manufactured antenna (a) exposed PCB and brass pins soldered in; (b) grooves for ridge adjustment; (c) ridge after mounting and adjusting on the grooves; (d) top view of the antenna fully assembled except for the radome. . . 35
3.17 Comparison between the possible tuning attempts (faded lines) and the final adopted (opaque lines). 36
3.18 Pictures of the Federal University of Campina Grande (UFCG) anechoic chamber setup:(a) the horn antenna fixed at the tripod on the rotative table and (b) measure setup using a reference horn antenna. 37
3.19 Measured (red) and simulated (dashed) antenna co-polar normalized gain in (a) H-plane and (b) E-plane. The shaded area is the simulated pattern below −10 dB at 2.2 GHz. 37

4.1 Phased array system overview. 39
4.2 RF front-end receiver block diagram. 41
4.3 Balun S-parameters characterization. 41
4.4 Images for the LNA evaluation boards (a) Qorvo QPL9065 and (b)Skyworks SKY67151, and (c) is the testing setup for the Y-factor measurement. 42
4.5 Performance characterization for LNA (a) gain and (b) noise figure. As the QLP9065 have two gain steps, the circuit is characterized twice. 42
4.6 S-parameters characterization of the SKY67151 LNA. 43
4.7 Dimensions in [mm] of the Chebyschev Hairpin Filter. 44
4.8 Frequency response of the 4th order hairpin filter. 44
4.9 Group delay and phase behavior as a function of the frequency for the 4th order hairpin filter. 45
4.10 System-level simulation of the elements shown in Figure 4.2, including implementation losses. 46
4.11 USRP B210 and ANTSDR E200 with internal frequency clock reference. 47
4.12 USRP B210 and ANTSDR E200 synchronized with an external reference provided by the Keysight N9020B Signal Analyzer. 48
4.13 USRP B210 and ANTSDR E200 synchronized with GPSDO reference clock. 48

5.1 Antenna array coordinate system and its layout. 51
5.2 Performance evaluation of position correction algorithms over variations in noise standard deviation in EDM. 55
5.3 Position estimation after applying noise with 1 m of standard deviation. 55
5.4 Averaged RMSE between estimated and real steering vectors under direction-independent perturbations. Deviation perturbations applied uniformly to the relative amplitude and phase. 56

5.5 Averaged RMSE between estimated and real steering vector direction-independent perturbations. Deviation perturbations applied uniformly to the relative amplitude and phase. 56

List of Symbols

$\vec{F}(\theta, \phi)$	Radiation vector
A	Physical aperture area of an antenna
$D(\theta, \phi)$	Directivity (Directive Gain)
e_a	Total aperture efficiency
$G(\theta, \phi)$	Antenna Gain (Power Gain)
P_{rad}	Total radiated power
$U(\theta, \phi)$	Radiation Intensity
$\boldsymbol{\rho}$	Vector of antenna gain and phase error parameters
δ	Position error vector
$\mathbf{a}(u), \mathbf{a}(v)$	Steering vectors for the array
$\mathbf{H}$	Channel matrix
$\mathbf{Q}$	Global calibration matrix
$\mathbf{X}$	Matrix of received signals from the array
$A(\vec{k})$	Array Factor
d_x, d_y	Array element spacing in x and y directions
M	Total number of antenna elements in the array
λ	Wavelength
θ, ϕ	Elevation and Azimuth angles
f	Frequency
k	Wave number, $2\pi/\lambda$
B	Bandwidth
E_b/N_0	Energy per bit to noise power spectral density ratio
F	Noise Figure of a device
k	Boltzmann's constant
L_f	Free-space path loss
P_R	Received power
P_T	Transmitted power
T_{sys}	System noise temperature

List of Abbreviations

ADC Analog-to-Digital Converter. 51
AWGN Additive White Gaussian Noise. 53

BPF Band-Pass Filter. 42

CNC Computer Numerical Control. 30

DoA Direction-of-Arrival. 51

EIRP Effective Isotropic Radiated Power. 7
ERP Effective Radiated Power. 7

FPGA Field-Programmable Gate Array. 48

GPS Global Positioning System. 48

HFSS High Frequency Structure Simulator. 24

IIP3 Third-Order Input Intercept Point. 46

LEO Low Earth Orbit. 1
LNA Low-Noise Amplifier. 42

MIG Metal Inert Gas. 30

OIP3 Third-Order Output Intercept Point. 47
OMT Orthomode Transducer. 22

PCB Printed Circuit Board. 33
PPS Pulse Per Second. 48
PTFE Polytetrafluoroethylene. 34

QRA Quad-Ridge Antenna. 23

RF Radio Frequency. 1, 2
RMSE Root Mean Square Error. 55

SDR Software-Defined Radio. 39
SNR Signal-to-Noise Ratio. 4

SQRA Square Quad-Ridge Horn Antenna. 23

VNA Vector Network Analyzer. 31

Glossary

Euclidean Distance Matrix A matrix containing the squared distances between a set of points in Euclidean space. In the context of array calibration, it is used with measured inter-antenna distances to estimate and correct for physical position errors in the array.. 53

GPS Disciplined Oscillator A high-precision oscillator whose frequency is continuously controlled and corrected by timing signals from Global Positioning System (GPS) satellites. It is used to provide a stable and accurate clock and time reference (PPS) for synchronizing multiple receivers in a distributed array.. 48

Link Budget A comprehensive accounting of all power gains and losses in a communication system, from the transmitter to the receiver. It is used to predict the signal-to-noise ratio and determine the system's performance margin.. 16

Steering Vector A complex vector that mathematically describes the response of an antenna array to a plane wave arriving from a specific direction (DoA). It contains the relative phase shifts of the signal at each antenna element based on the array's geometry and the signal's arrival angle.. 52

Chapter 1

Introduction

1.1 State-of-the-art

A ground station for Low Earth Orbit (LEO) satellites is based on a parabolic antenna between 10 m and 11 m of diameter, combined with a mechanical system that allows it to track one satellite at a time. To enhance its transmission rate, such base stations are located in sub-polar regions that maximize the daily data transmission window [13]. Taking into account such factors, a ground station located in Poker Flats, Alaska, US, costs between $2 M and $4 M to build and a similar value to maintain, and have approximately six months of operating.

Another approach to track satellites is the use of a distributed, phased-array-like antenna system. A set of smaller antennas is easier to build and maintain. Moreover, spreading the arrays over a large territory makes it possible to maximize the area covered with optimal placement of the ground stations as demonstrated in [49] and [53].

Another advantage of the use of a phased array of antennas is the possibility of partitioning the array into sub-arrays and tracking more than one satellite at the same time. Such approach enables the base station to be used by multiple users simultaneously, making it a shared platform. This is particularly interesting for the defense application, as it makes it possible to investigate the satellite traffic [11].

As a first step towards the construction of this kind of base station, this work aims to design and characterize the elements of the phased array that include the parabolic feed antenna, Radio Frequency (RF) front-end and the phased array calibration algorithms. Some of these elements are entirely simulated and manufactured in this work, while others have only been simulated.

1.2 Contextualization

The feasibility of such a system has been demonstrated in [13] and [12] theoretically and experimentally. The actual project implementation is about a phased array of sixteen elements of 2.4 m parabolic dish reflectors as shown in Figure 1.1.

The main objective is to adapt fixed parabolic dishes with motors to point the antenna towards the satellite automatically. The band of interest is the S-band since this project envisions a link with Brazilian national satellites. Furthermore, the antenna system must

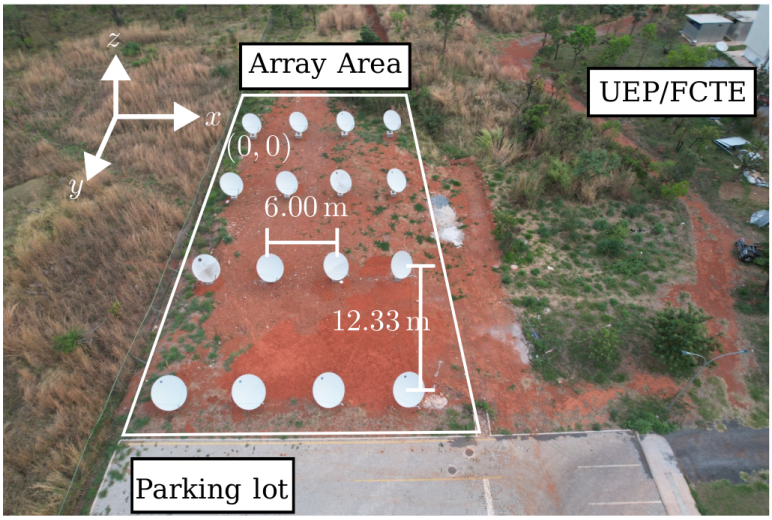

Figure 1.1: Aerial picture of the phased array mounted in this project.

digitize and store the signals in a computational cluster in order to integrate the data with other remote base stations. This project is granting by the Brazilian National Council of Research and Technology (CNPq) with title *Estação Terrena Autônoma Distribuída de Baixo Custo e Alta Taxa de Download*, N. 405635/2022-2, 20/2022 - Faixa A.

The accomplishment of this project involves a set of multidisciplinary sub-projects, including, but not limited to:

- Design of the RF receiver;
- Design of the feed horn antenna for the different operating bands;
- Phased array calibration algorithms considering the outdoor environment and the large spacing between the antennas;
- Algorithm to predict the satellite orbit;
- Mechanical and electronic system to follow the satellites;
- Software to handle the array data and properly store them;
- The post-processing Software to combine the phased array signals and demodulate the information.

In the future, more degrees of complexity can be applied in order to build a robust and stable system suitable to meet the needs of the defense and aerospace industry.

1.3 Main Objectives

The objectives are listed as:

- The simulation, manufacturing and characterization of two quad-ridge antennas candidates to be the antenna feed of the parabolic reflector;
- The conceptual design, simulation and characterization of a RF reception chain to process the signal in both the analog and digital domains;
- Development of algorithms for calibration of large-spaced array antennas in an outdoor environment.

1.4 Organization of this work

The dissertation is organized as follows:

- Chapter 2 aims to create a baseline for understanding the developments of this work.
- Chapter 3 exposes the feed horn development based on a square and conical quad-ridge horn antennas.
- Chapter 4 develops the proposed system for the base station operation and signal handling.
- Chapter 5 discusses the method for calibrating the phased array uncertainties.

Chapter 2

Theoretical Foundation

Antenna parameters are key to the correct design for a defined application. For instance, applications involving mobile devices require antennas with low gain, nearly omnidirectional patterns, and circular polarization; conversely, point-to-point communications normally involves long-distance scenarios where antennas with higher gain and linear polarization are suitable [35], [33].

The antenna parameters are highly dependent on each other; therefore, antenna design demands a deep understanding of each parameter and its relationship with the other metrics to achieve the best combination for a specific application.

For satellite communications, specifically for base stations, high gain and dual-polarized antennas are suitable in order to establish a reliable link over unpredictable environmental changes, since the channel is a path through the entire atmosphere.

Such specifications are quantified in the link budget table, which maps the signal and noise power throughout the system. The key metric is the Signal-to-Noise Ratio (SNR) margin, a parameter that describes the system performance overhead that makes it robust to link variations [46].

This chapter presents the mathematical description of all the main antenna parameters necessary to design an antenna for satellite communication. It also describes the quantities needed to correctly implement the link budget table and, finally, provides a brief discussion on phased array antennas.

2.1 Antenna Parameters

2.1.1 Energy Flux and Radiating Intensity

The electromagnetic flux is given by the time-averaged Poynting vector, $\vec{\mathcal{P}}$, calculated in terms of the radiation fields $\vec{E}$ and $\vec{H}$. Considering the coordinate system shown in Figure 2.1:

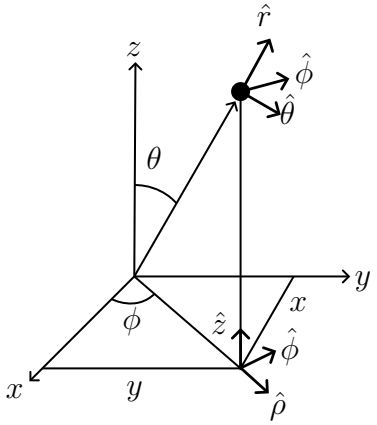

Figure 2.1: Reference polar and rectangular coordinate systems.

$$\vec{\mathcal{P}} = \frac{1}{2}\,\mathrm{Re}(\vec{E} \times \vec{H}^*) = \frac{1}{2}\left(-jk\eta\frac{e^{-jkr}}{4\pi r}\right)\left(jk\frac{e^{jkr}}{4\pi r}\right)\mathrm{Re}[(\hat{\theta}F_\theta + \hat{\phi}F_\phi) \times (\hat{\phi}F_\theta^* - \hat{\theta}F_\phi^*)], \tag{2.1}$$

where F_θ and F_ϕ are the polar components of the radiation vector $\vec{F} = \int_V \vec{J}(\vec{r'})e^{j\vec{k}\cdot\vec{r'}}\ \mathrm{d}^3\vec{r'}$, where $\vec{k} = k\hat{r}$ and k is the wave number. Since $\hat{\theta} \times \hat{\phi} = \hat{r}$, it follows that:

$$(\hat{\theta}F_\theta + \hat{\phi}F_\phi) \times (\hat{\phi}F_\theta^* - F_\theta^* - \hat{\theta}F_\phi^*) = \hat{r}(|F_\theta|^2 + |F_\phi|^2) = \hat{r}|\vec{F}_\perp(\theta,\phi)|^2.$$

Following this identity, the time-averaged Poynting vector is expressed as:

$$\vec{\mathcal{P}} = \hat{r}\mathcal{P}_r = \hat{r}\frac{\eta k^2}{32\pi^2 r^2}|\vec{F}_\perp(\theta,\phi)|^2. \tag{2.2}$$

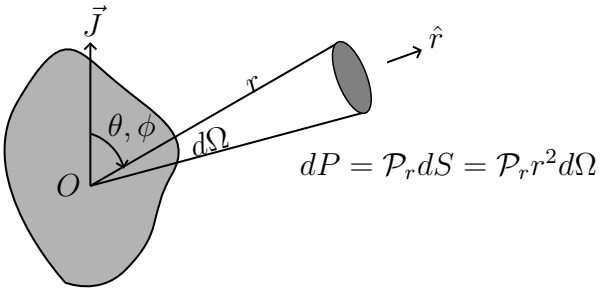

Figure 2.2: Radiated power into solid angle $\mathrm{d}\Omega$.

With reference to Figure 2.2, the power $\mathrm{d}P$ intercepting the area element $dS = r^2 d\Omega$ in the (θ, ϕ)-direction defines the power per unit area as

$$\frac{\mathrm{d}P}{\mathrm{d}S} = \frac{\mathrm{d}P}{r^2\mathrm{d}\Omega} = \mathcal{P}_r = \frac{\eta k^2}{32\pi^2 r^2}|\vec{F}_\perp(\theta,\phi)|^2. \tag{2.3}$$

The radiation intensity $U(\theta, \phi)$ is defined as the power radiated per unit solid angle $\mathrm{d}\Omega$:

$$U(\theta,\phi) = \frac{\mathrm{d}P}{\mathrm{d}\Omega} = r\mathcal{P}_r = \frac{\eta k^2}{32\pi^2}|\vec{F}_\perp(\theta,\phi)|^2. \tag{2.4}$$

Integrating the radiation intensity over all solid angles $\mathrm{d}\Omega = \sin(\theta)\mathrm{d}\theta\mathrm{d}\phi$, yields the total radiated power P_{rad}:

$$P_{rad} = \int_0^{\pi}\int_0^{2\pi} U(\theta,\phi) \quad \mathrm{d}\Omega. \tag{2.5}$$

For an isotropic radiator, the total power is distributed over the entire solid angle of a sphere, $\Omega_{\mathrm{sphere}} = 4\pi$ st.. Therefore, the isotropic radiation intensity is the total radiated power divided by the total solid angle:

$$U_I = \left(\frac{\mathrm{d}P}{\mathrm{d}\Omega}\right)_I = \frac{P_{rad}}{\Omega_{\mathrm{sphere}}} = \frac{P_{rad}}{4\pi} = \frac{1}{4\pi}\int_0^{\pi}\int_0^{2\pi} U(\theta,\phi) \quad \mathrm{d}\Omega. \tag{2.6}$$

Following the same principle, the power density for an isotropic radiator is:

$$\left(\frac{\mathrm{d}P}{\mathrm{d}S}\right)_I = \frac{U_I}{r^2} = \frac{P_{rad}}{4\pi r^2}. \tag{2.7}$$

2.1.2 Directivity, Gain and Beamwidth

The directivity, $D(\theta,\phi)$, quantifies an antenna ability to direct power in a specific direction (θ,ϕ) and is defined as the radiation intensity normalized by the corresponding isotropic intensity:

$$D(\theta,\phi) = \frac{U(\theta,\phi)}{U_I} = \frac{U(\theta,\phi)}{P_{rad}/4\pi} = \frac{4\pi}{P_{rad}}\frac{\mathrm{d}P}{\mathrm{d}\Omega}. \tag{2.8}$$

In the direction of maximum radiation, (θ_0,ϕ_0), the maximum directivity is defined as:

$$D_{max} = D(\theta_0,\phi_0) = \frac{U(\theta_0,\phi_0)}{U_I} = \frac{U_{max}}{U_I}. \tag{2.9}$$

The directivity is usually expressed in dB as $D_{\mathrm{dB}} = 10\log_{10} D_{max}$. Applying the directivity definition into the radiation intensity expression yields:

$$\frac{\mathrm{d}P}{\mathrm{d}\Omega} = U(\theta,\phi) = D(\theta,\phi)U_I = \frac{P_{rad}D(\theta,\phi)}{4\pi}. \tag{2.10}$$

The same procedure can be followed for the power intensity:

$$\frac{\mathrm{d}P}{\mathrm{d}S} = \frac{\mathrm{d}P}{r^2\mathrm{d}\Omega} = \frac{P_{rad}D(\theta,\phi)}{4\pi r^2}. \tag{2.11}$$

The isotropic power density described by Equation 2.7 can be generalized for any antenna using Equation 2.11. The quantity $P_{rad}D(\theta,\phi)$ is defined as the Effective Radiated Power (ERP) towards the (θ,ϕ)-direction. In the direction of maximum gain, the quantity $P_{rad}D_{max}$ is defined as Effective Isotropic Radiated Power (EIRP). The EIRP defines the maximum power density the antenna is capable of producing:

$$\left(\frac{\mathrm{d}P}{\mathrm{d}S}\right)_{\max} = \frac{P_{\mathrm{EIRP}}}{4\pi r^2}, \quad \text{where } P_{\mathrm{EIRP}} = P_{rad}D_{max}. \tag{2.12}$$

EIRP is a system-level metric that is independent of the individual tranmitter power or antenna gain values. For instance, the two systems observed in Figure 2.3 have the same EIRP value; however, the first uses an isotropic antenna while the second uses a highly directional antenna. The advantage of the second system is the lower transmitter power required to establish the transmission link, at the expense of the signal area coverage.

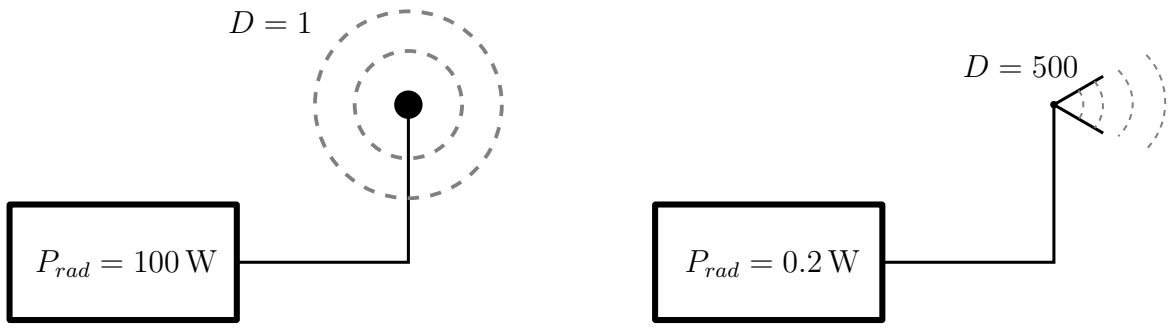

Figure 2.3: Example of two systems with the same EIRP, where (a) represents a system using an isotropic antenna and (b) a system using a directive antenna.

The gain (or power gain),G, of an antenna is defined by Equation 2.13. The difference between gain and directivity is that the radiation intensity is normalized by the transmitted power instead of the radiated power. The transmitted power, P_T, is related to the power at the output of the transmitter and disregards losses from the transmission line and the antenna own ohmic losses. The relationship between the total radiated power and the transmitted power is further clarified by the Figure 2.4.

$$G(\theta,\phi) = \frac{U(\theta,\phi)}{P_T/4\pi} = \frac{4\pi}{P_T}\frac{\mathrm{d}P}{\mathrm{d}\Omega}. \tag{2.13}$$

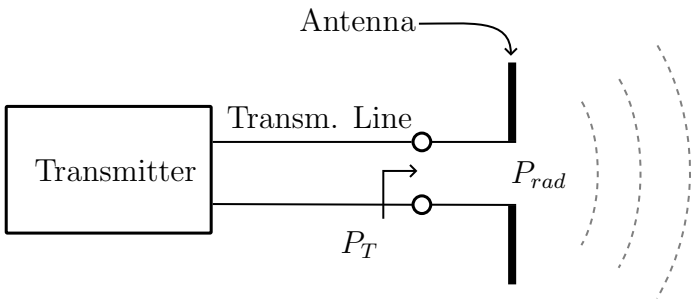

Figure 2.4: Relationship between the transmitted power, P_T, and radiated power, P_{rad}.

Since $P_{rad} \leq P_T$, the two quantities can be related by a radiation efficiency factor, e :

$$e = \frac{P_{rad}}{P_T}. \tag{2.14}$$

Furthermore, as the difference between the antenna directivity and gain is related only to the antenna efficiency, they can be related using the efficiency factor as follows:

$$G(\theta, \phi) = eD(\theta, \phi). \tag{2.15}$$

It follows that the effective radiated power can also be written in terms of gain as $P_{\text{ERP}} = P_{rad}D(\theta, \phi) = P_T G(\theta, \phi)$, and the EIRP as $P_{\text{EIRP}} = P_{rad}D_{max} = P_T G_{max}$. The use of the ERP and EIRP in terms of antenna gain and transmitter power is the more usual in link budget estimations.

Since the spatial functions are all proportional to each other, a normalized power pattern, $g(\theta, \phi)$, can be introduced, as shown in Equation 2.16.

$$g(\theta, \phi) = \frac{G(\theta, \phi)}{G_{max}}, \tag{2.16}$$

which, following the proportionality principle, leads to:

$$g(\theta, \phi) = \frac{G(\theta, \phi)}{G_{max}} = \frac{D(\theta, \phi)}{D_{max}} = \frac{U(\theta, \phi)}{U_{max}} = \frac{|F_\perp(\theta, \phi)|^2}{|F_\perp|^2_{max}}. \tag{2.17}$$

In the context of high-gain antennas, the concept of antenna beam solid angle is useful, as it describes the radiated power P_{rad} into a small solid angle $\Delta\Omega$. The radiation intensity in the solid angle is given by Equation 2.18.

$$U = \frac{\Delta P}{\Delta\Omega} \simeq \frac{P_{rad}}{\Delta\Omega}, \tag{2.18}$$

where $\Delta P \simeq P_{rad}$, considering that the energy outside the solid angle is negligible. Extending this definition to the maximum directivity gives:

$$D_{max} = \frac{4\pi U}{P_{\text{rad}}} = \frac{4\pi}{\Delta\Omega}. \tag{2.19}$$

Equation 2.19 shows that the smaller the beam solid angle, the more directive the antenna. Isolating Equation 2.19 in terms of the beam solid angle yields:

$$\Delta\Omega = \frac{4\pi}{D_{max}} = \frac{4\pi U_I}{U_{max}} = \frac{1}{U_{max}} \int_0^{\pi} \int_0^{2\pi} U(\theta, \phi) \quad \mathrm{d}\Omega,$$

or, in terms of normalized pattern:

$$\Delta\Omega = \int_0^{\pi} \int_0^{2\pi} g(\theta, \phi) \quad \mathrm{d}\Omega. \tag{2.20}$$

Therefore, for first order approximation, it is possible to consider $P_{rad} = U_{max}\Delta\Omega$. Furthermore, assuming an uniform gain within the beam solid angle is also a valid approximation:

$$g(\theta, \phi) = \begin{cases} 1, & \text{if } 0 \leq \theta \leq \Delta\theta_B/2 \\ 0, & \text{if } \Delta\theta_B/2 \leq \theta \leq \pi \end{cases} .$$

Applying this result to Equation 2.20 gives:

$$\Delta\Omega = \int_0^{\Delta\theta_B/2} \int_0^{2\pi} \quad \mathrm{d}\Omega = \int_0^{\Delta\theta_B/2} \int_0^{2\pi} \sin(\theta) \quad \mathrm{d}\theta\mathrm{d}\phi = 2\pi \left(1 - \cos\left(\frac{\Delta\theta_B}{2}\right)\right). \tag{2.21}$$

Using a second-order Taylor approximation for small beamwidths, where $\cos(x) \simeq 1 - x^2/2$:

$$\Delta\Omega = \frac{\pi}{4}(\Delta\theta_B)^2. \tag{2.22}$$

Applying Equation 2.22 to Equation 2.19 to express the maximum directivity for small beamwidths:

$$D_{max} = \frac{16}{\Delta\theta_B^2}. \tag{2.23}$$

These definitions will be useful to estimating the parabolic reflector gain.

2.2 Radiation from apertures

Section 2.1 briefly discussed the metrics used to evaluate antenna performance mathematically. This section deals with the more fundamental phenomenon of how fields behave when radiated from apertures, such as slots, open-ended waveguides, horns, and reflector and lens antennas.

The radiated fields, $(\vec{E}, \vec{H})$, are extracted from the equivalent electric and magnetic surface currents, $(\vec{J}_s, \vec{J}_{ms})$ through the field equivalence principle. Equation 2.24 states the equivalent surface currents through the electric field $\vec{E}_a$ and the magnetic field $\vec{H}_a$ on the aperture:

$$\vec{J}_s = \hat{n} \times \vec{H}_a, \tag{2.24}$$

$$\vec{J}_{ms} = -\hat{n} \times \vec{E}_a. \tag{2.25}$$

The fields at an antenna aperture are therefore described by its surface currents and can be calculated by the surface integrals as:

$$\vec{E} = \frac{1}{j\omega\varepsilon} \int_A [(\vec{J}_s \cdot \nabla')\nabla' G + k^2 \vec{J}_s G - j\omega\varepsilon \vec{J}_{ms} \times \nabla' G] \quad \mathrm{d}S', \tag{2.26}$$

$$\vec{H} = \frac{1}{j\omega\mu} \int_A [(\vec{J}_{ms} \cdot \nabla')\nabla' G + k^2 \vec{J}_{ms} G + j\omega\mu \vec{J}_s \times \nabla' G] \quad \mathrm{d}S'. \tag{2.27}$$

where

$$G = G(\vec{r} - \vec{r'}) = \frac{e^{-jk|\vec{r} - \vec{r'}|}}{4\pi|\vec{r} - \vec{r'}|}$$

is the Green function, k is the wave number and ω is the angular frequency of the monochromatic regime. Equations 2.26 and 2.27 can be expressed in terms of surface fields on the aperture, as illustrated in Figure 2.5:

$$\vec{E} = \frac{1}{j\omega\varepsilon} \int_A [(\hat{n} \times \vec{H}_a) \cdot \nabla'(\nabla' G) + k^2 (\hat{n} \times \vec{H}_a) G + j\omega\varepsilon (\hat{n} \times \vec{E}_a) \times \nabla' G] \quad \mathrm{d}S', \tag{2.28}$$

$$\vec{H} = \frac{1}{j\omega\mu} \int_A [-(\hat{n} \times \vec{E}_a) \cdot \nabla'(\nabla' G) - k^2 (\hat{n} \times \vec{E}_a) G + j\omega\mu (\hat{n} \times \vec{H}_a) \times \nabla' G] \quad \mathrm{d}S'. \tag{2.29}$$

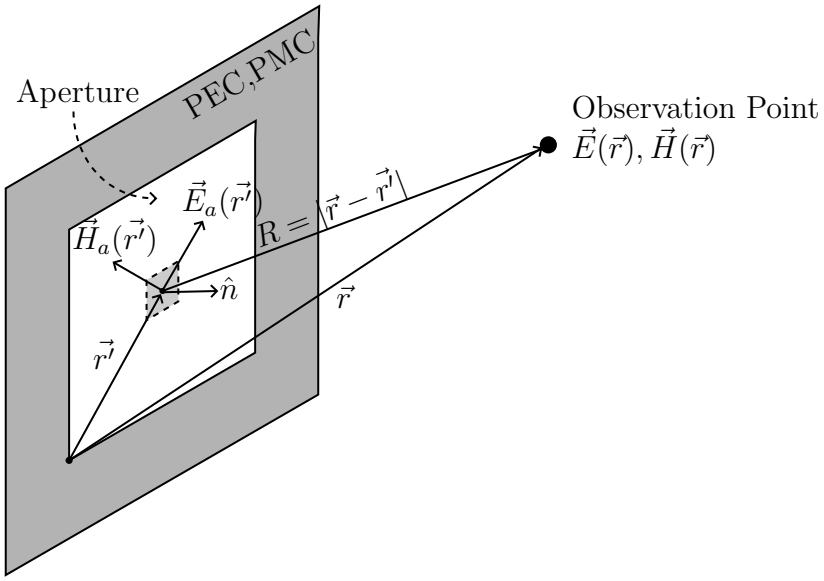

Figure 2.5: Field distribution on the aperture surface.

Under far-field conditions, the radiation vectors are given by the two-dimensional Fourier transform integrals, as described in Equation 2.30, since the aperture surface is usually flat.

$$F(\theta,\phi) = \int_A \vec{J}_s(\vec{r'}e^{j\vec{k}\cdot\vec{r'}} \quad \mathrm{d}S') = \int_A \hat{n} \times \vec{H}_a(\vec{r'})e^{j\vec{k}\cdot\vec{r'}} \quad \mathrm{d}S', \tag{2.30}$$

$$\vec{F}_m(\theta,\phi) = \int_A \vec{J}_{ms}(\vec{r'})e^{j\vec{k}\cdot\vec{r'}} \quad \mathrm{d}S' = -\int_A \hat{n} \times \vec{E}_a(\vec{r'})e^{j\vec{k}\cdot\vec{r'}} \quad \mathrm{d}S'. \tag{2.31}$$

where the Fourier transforms on the aperture are given by:

$$f(\theta,\phi) = \int_A \vec{E}_a(\vec{r'})e^{j\vec{k}\cdot\vec{r'}} \quad \mathrm{d}S', \tag{2.32}$$

$$g(\theta,\phi) = \int_A \vec{H}_a(\vec{r'})e^{j\vec{k}\cdot\vec{r'}} \quad \mathrm{d}S'. \tag{2.33}$$

2.3 Quad-ridge Horn Antennas

Waveguides are widely used to carry signals with low loss. This feature enables the carrying of large amounts of power since the energy propagates through the air (or the dielectric with which the waveguide is loaded). The bandwidth of a square waveguide, based on the cutoff frequencies of its first two modes (TE_{10}, TE_{11}) cutoff frequencies , is about 34 % of the center frequency. For circular waveguides, the TE_{11} and TM_{01} bandwidth is around 26.5 % [1].

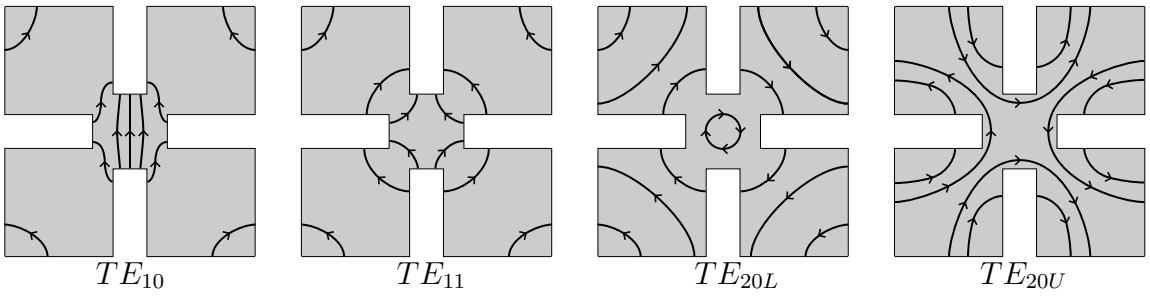

(a)

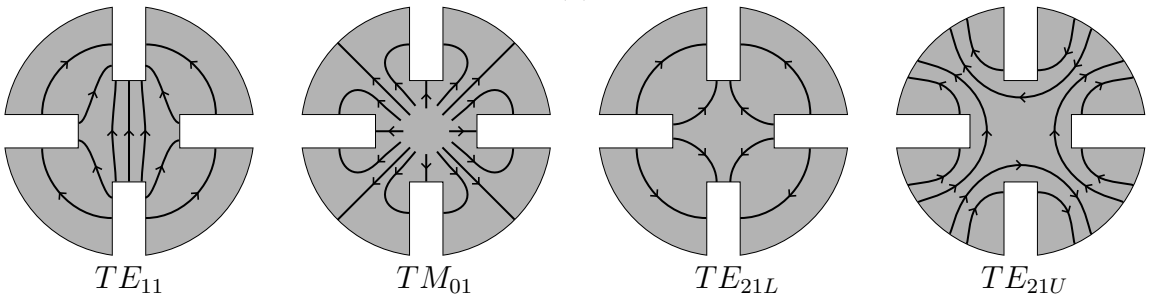

(b)

Figure 2.6: Modal distribution in (a) quad-ridge square waveguides and in (b) quad-ridge circular waveguides.

To increase the bandwidth by maintaining mode purity over a wider frequency range, the waveguide can be loaded with ridges. This technique introduces new degrees of freedom in the

modal distribution at the expensive of carrying less power, since the cross-sectional area of the propagation mode is reduced. However, the introduction of ridges increase the complexity of the boundary conditions, and therefore, as no analytical solutions exist for the field equations, numerical solvers must be employed [7], [9].

Modal analysis enables bandwidth increases. Early works, such as [7], [9] and [20], have investigated the modal distribution of ridge-loaded waveguides, focusing mainly on the lowest-order modes. Figure 2.6 illustrates the first modal distributions of square and circular waveguides. An in-depth analysis of the higher modes of quad-ridge waveguides is provided in [34] and [30], but such modes have high cutoff frequencies, above of the band of interest for this work.

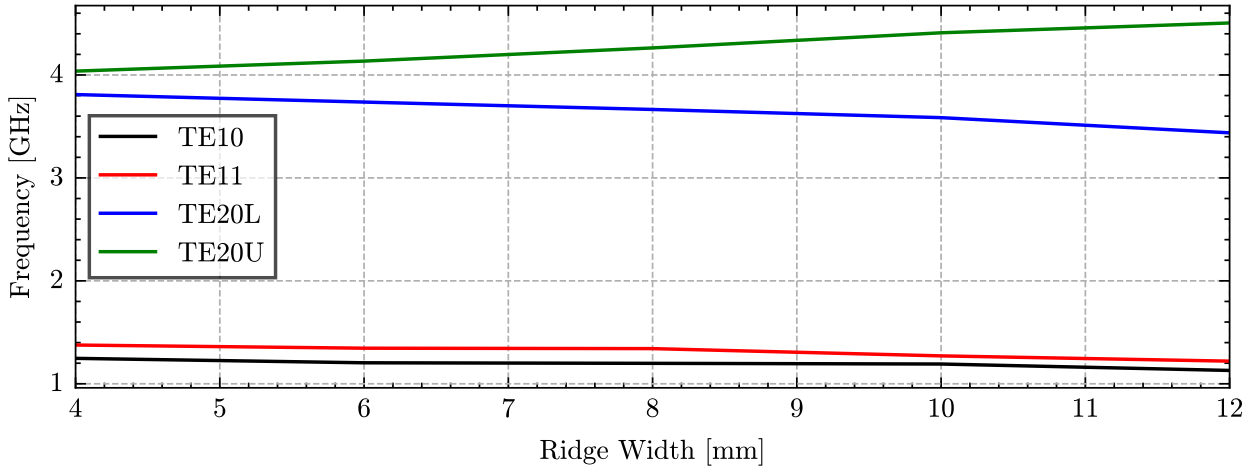

Figure 2.7: Modal behavior with the change of the width of the waveguide ridges, fixing the ridge height at 26 mm.

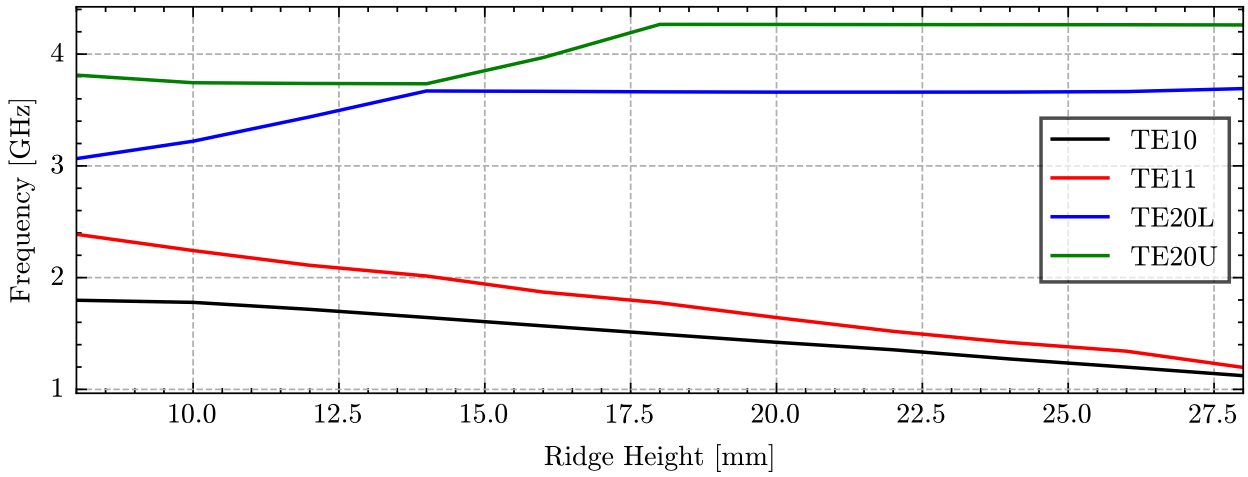

Figure 2.8: Modal behavior with the change of the height of the waveguide ridges fixing the width at 8 mm.

Figures 2.7 and 2.8 show the cutoff frequency for each mode as a function of the variation of ridge width and height for a 40 mm × 40 mm square waveguide. The modal analysis suggests

that for a greater height value (a narrower gap between ridges) the TE20 mode splits, lifting an orthogonal degeneracy, and rises in frequency, thereby increasing the bandwidth. For modes TE10 and TE11, the cutoff frequency tends to decrease, which contributes also to increasing the bandwidth.

The primary concern is the relationship between the TE10 and TE11 modes. The excitation of these modes depends on the waveguide excitation geometry. Bandwidth broadening is achieved when the excitation geometry privileges the excitation of the mode TE10. Such excitation geometries are further investigated in Section 3.1.2.

In the context of antennas, the presence of ridges inside the throat section increases the band of operation, since the main limitation on bandwidth is the waveguide size and its inherent modal properties.

2.4 Parabolic Reflectors

Parabolic reflectors are high-gain antennas commonly used in line-of-sight communication. Due to the low power of satellite signals, parabolic reflectors make a significant contribution to the link budget by improving the relationship of gain and temperature G/T° figure of merit.

A derivation of parabolic reflector parameters is available in [35].

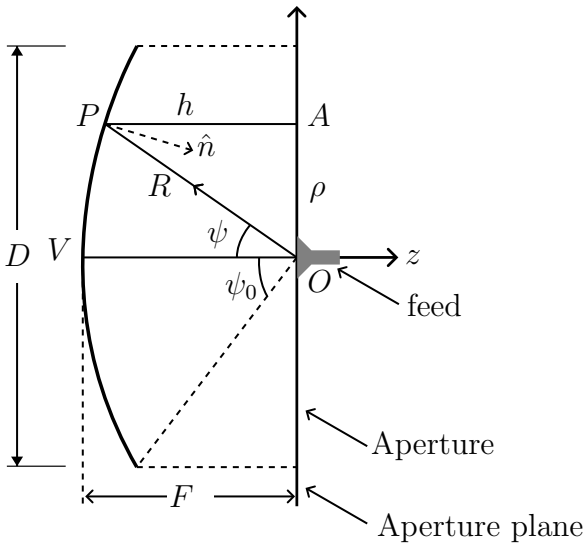

Figure 2.9: Parabolic reflector parameter.

The gain of an aperture is given by Equation 2.34.

$$G_a = \frac{4\pi U_{max}}{P_a}, \tag{2.34}$$

where P_a, the amount of power incident on the aperture, is defined by Equation 2.35 using the parameters from Figure 2.9.

$$P_a = \frac{1}{2\eta}\int_A |\vec{E}_a|^2 \quad \mathrm{d}A = \int_0^{\psi_0}\int_0^{2\pi} U_{feed}(\psi,\chi)\sin(\psi) \quad \mathrm{d}\psi\mathrm{d}\chi. \tag{2.35}$$

As the reflector antenna performance depends on the radiation power of its feeder, the gain becomes:

$$G_{ant} = \frac{4\pi U_{max}}{P_{feed}} = \frac{4\pi U_{max}}{P_a}\frac{P_a}{P_{feed}} = G_a e_{spl}, \tag{2.36}$$

where the factor $e_{spl} = P_a/P_{feed}$ is the spillover efficiency and represents the fraction of power from the feed that is effectively reflected by the parabolic dish.

The aperture gain is also represented by the geometrical aperture area and the aperture taper and phase error efficiencies as shown in Equation 2.37.

$$G_a = \frac{4\pi A}{\lambda^2} e_{atl} e_{pel}, \tag{2.37}$$

which extends to the overall antenna gain:

$$G_{ant} = G_a e_a = \frac{4\pi A}{\lambda^2} e_{atl} e_{pel} e_{spl}. \tag{2.38}$$

The factor $e_a = e_{atl}e_{pel}e_{spl}$ is called the total aperture efficiency. The aperture taper efficiency, e_{atl}, is defined as:

$$e_{atl} = \frac{\left|\int_A |E_a| \quad \mathrm{d}A\right|^2}{A\int_A |E_a|^2 \quad \mathrm{d}A}. \tag{2.39}$$

In association with other losses, a practical value for parabolic reflector aperture efficiency is around 0.55-0.65. The parabolic gain expressed in terms of diameter is given by Equation 2.40.

$$G_{ant} = e_a \frac{4\pi A}{\lambda^2} = e_a \left(\frac{\pi D}{\lambda}\right)^2. \tag{2.40}$$

The 3-dB beamwidth of a reflector antenna with diameter D can be estimated by the approximation:

$$\Delta\theta_{3\,\mathrm{dB}} = 70^\circ \frac{\lambda}{D}\ [^\circ]. \tag{2.41}$$

2.5 Satellite communications

2.5.1 Satellite Specifications

The satellite considered in this work is the VCUB1 from Visiona. It was launched on April 15$^{\text{th}}$, 2023, becoming the first Earth Observation Satellite designed by the Brazilian national industry. VCUB1 is a LEO satellite in Sun-Synchronous Orbit (inclination of 98°) transmitting signals within the S-band.

Due the confidential nature of the satellite full specifications, Table 2.1 shows only the downlink parameters for the payload imagery:

Table 2.1: Simplified data from Visiona VCUB1.

Feature	**Detail**
Downlink Frequency	2.244 GHz
Antenna EIRP	40.5
Payload Image	10 Mbps/QPSK/6MHz-BW/LHCP

2.5.2 Link budget

In a Link Budget analysis, the receiving system signal-to-noise ratio (SNR) at the output of the receiver is the parameter of most interest. The excess of SNR is called the margin, and it is related to the robustness of the system against channel or components variations. Figure 2.10 shows the main elements in an antenna link. A full model would include more components, but that would require prior knowledge about the system implementation on the transmitter side.

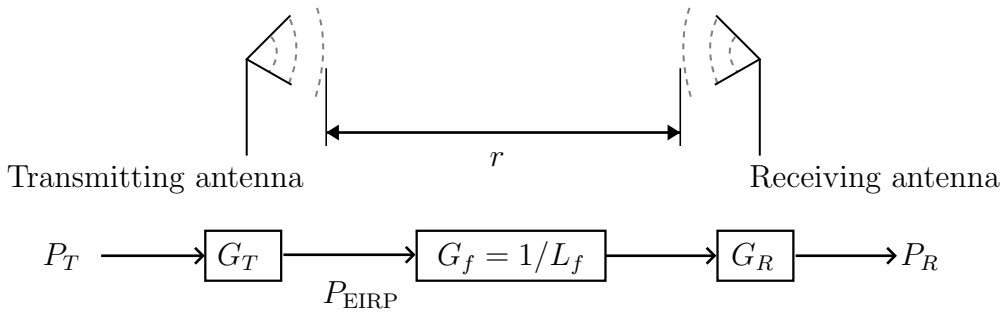

Figure 2.10: Link between antennas.

The following sections discuss the main quantities used to develop the Link Budget table presented in Section 4.

Received Power

The free-space path loss is given by the Equation 2.42.

$$L_f = \left(\frac{4\pi r}{\lambda}\right)^2. \tag{2.42}$$

where r is the distance between the antennas and λ is the wavelength at the center frequency.

The power received at the antenna output is found from the Friss transmission formula in Equation 2.43.

$$P_R = P_T G_T \left(\frac{\lambda}{4\pi r}\right)^2 G_R = \frac{P_T G_T G_R}{L_f}, \tag{2.43}$$

where P_T is the transmitter power, G_T is the transmitter antenna gain and G_R is the receiver antenna gain. These concepts follow the antenna parameters discussed in Section 2.1.

Furthermore, defining the load matching efficiency as $e_{\text{load}} = 1 - |\Gamma_{\text{load}}|^2$ and including it in the Friss formula that leads to Equation 2.44.

$$P_R = \frac{P_T G_T G_R \lambda^2}{(4\pi r)^2}(1 - |\Gamma_{\text{load}}|^2) = \frac{P_T G_T G_R \lambda^2}{(4\pi r)^2} e_{\text{load}}. \tag{2.44}$$

2.5.3 Antenna Noise Temperature

While the path of the useful signal is well defined, the other parameter of interest for characterizing the SNR is the noise power behavior throughout the system. A typical receiver antenna system is shown in Figure 2.11. The receiver antenna have the feed line with the noise temperature and gain characterized by T_{feed} and G_{feed}. The T_{sa}, T_{sb} and T_{sc} are the accumulated noise contributions after each element. G_{LNA}, T_{LNA}, G_{rec}, T_{rec} are the gain and noise temperature for the first LNA and the subsequent receiver elements, respectively.

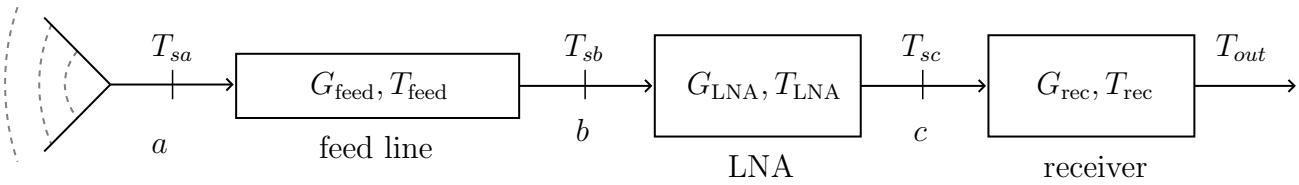

Figure 2.11: Antenna receiving system.

The noise power in a specific bandwidth is defined by Equation 2.45, where $k = 1.3803 \cdot 10^{-23}\ \text{W Hz}^{-1}\,\text{K}$ is the Boltzmann constant, T is the temperature in Kelvin and B is the signal bandwidth.

$$N = kTB. \tag{2.45}$$

The antenna noise temperature N_{ant} at the antenna terminals is determined by Equation 2.46. The antenna temperature, T_{ant}, is an averaged contribution of the brightness temperature

$T(\theta, \phi)$ over all directions, weighted by the normalized gain as described in Equation 2.47, where $\Delta\Omega$ serves as normalization factor for this average:

$$N_{\text{ant}} = kT_{\text{ant}}B, \quad \text{where} \tag{2.46}$$

$$T_{\text{ant}} = \frac{1}{\Delta\Omega}\int_0^{\pi}\int_0^{2\pi} T(\theta,\phi)g(\theta,\phi) \quad \mathrm{d}\Omega. \tag{2.47}$$

2.5.4 System Noise Temperature

Besides the antenna noise temperature, the receiver and all active and passive devices are noise generators. The propagated noise is modeled as shown in Figure 2.12, and the added noise power is described in terms of an effective noise temperature, T_e, as shown in Equation 2.48.

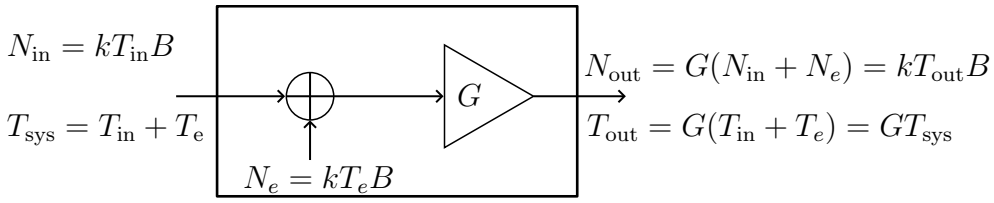

Figure 2.12: Device noise model.

$$N_e = kT_eB. \tag{2.48}$$

Following the notation of Figure 2.12, the total system noise at the input is given as:

$$N_{sys} = N_{in} + N_e = k(T_{in} + T_e)B = kT_{sys}B, \tag{2.49}$$

where the quantity $T_{sys} = T_{in} + T_e$ is called system noise temperature, N_{in} is the input noise power, N_e is the equivalent noise power added by the device, and N_{out} is the output noise power. Each noise power source have their respective noise temperature: T_{in} the input noise temperature; T_e the equivalent noise temperature; and T_{out} the output noise temperature.

After passing through a device with available power gain G, the noise power and noise temperature at the output of the device are expressed as:

$$N_{out} = G(N_{in} + N_e) = GN_{sys}, \tag{2.50}$$

$$T_{out} = G(T_{in} + T_e) = GT_{sys}, \tag{2.51}$$

Assuming the device in Figure 2.12 is noiseless, the system SNR is the same at the input and output:

$$SNR_{\text{sys}} = \frac{S_{in}}{N_{sys}} = \frac{S_{in}}{kT_{sys}B} = \frac{S_{in}}{k(T_{in} + T_e)B}. \tag{2.52}$$

where S_{in} is the signal power. Another important concept is the noise figure (NF) of a device, defined in terms of the effective noise temperature as:

$$NF = 1 + \frac{T_e}{T_0} \leftrightarrow T_e = (NF - 1)T_0, \tag{2.53}$$

where T_0 is a reference temperature, which, by standard, is adopted as T_0 =290 K.

If devices are cascaded, as shown in Figure 2.13, each contributes to the overall system temperature according to the Friss formula for noise:

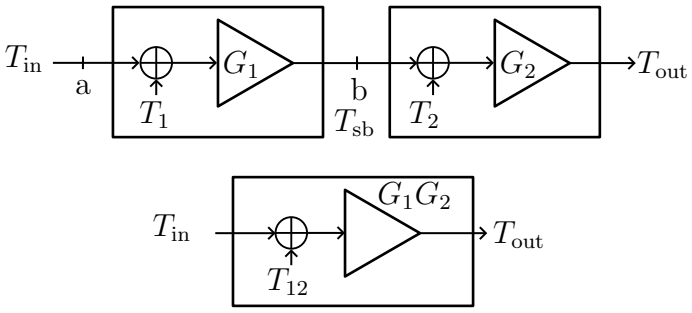

Figure 2.13: Noise in cascaded devices.

$$T_{12} = T_1 + \frac{1}{G_1}T_2, \tag{2.54}$$

where T_1 and T_2 are the contributions of the noise power for the first and second elements of Figure 2.13, and G_1 is the gain of the first device. The accumulated noise contribution from the point a to point b is given by T_{sb}.

This leads to the important conclusion that the first element of a cascaded system is the most critical to the overall system noise temperature. The gain of the first element minimizes the influence of the subsequent components. This concept also translates to the overall noise figure:

$$NF_{123} = NF_1 + \frac{NF_2 - 1}{G_1} + \frac{NF_3 - 1}{G_1G_2}. \tag{2.55}$$

Consequently, applying these concepts to the system of Figure 2.11 leads to an effective noise temperature:

$$T_{\text{eff}} = T_{\text{feed}} + \frac{1}{G_{\text{feed}}}T_{\text{LNA}} + \frac{1}{G_{\text{feed}}G_{\text{LNA}}}T_{\text{rec}}. \tag{2.56}$$

It is possible to express the feed line noise temperature, T_{feed}, in terms of its physical temperature, T_{phys}, and its loss ($L_{\text{feed}} = 1/G_{\text{feed}}$):

$$T_{\text{eff}} = \frac{1}{G_{\text{feed}}}(1 - G_{\text{feed}})T_{\text{phys}} + \frac{1}{G_{\text{feed}}}T_{\text{LNA}} + \frac{1}{G_{\text{feed}}G_{\text{LNA}}}T_{\text{rec}}. \tag{2.57}$$

Data Rate

The *SNR* is also commonly expressed in terms of the energy per bit to noise power spectral density ratio (E_b/N_0):

$$SNR = \frac{P}{N_{sys}} = \frac{P}{kT_{sys}B} = \frac{E_b}{N_0}\frac{R}{B}, \tag{2.58}$$

where R is the data rate defined by $R = 1/T_b$ and T_b is the time per transmitted bit.

2.6 Antenna arrays

Phased array antennas are used to electronically steer the main beam of radiated power towards a specific angular sector. This is achieved by controlling the phase and amplitude of the signal at each antenna element within a specific geometric configuration. This work focuses on using only the geometrical and phase variation to shape the array radiation pattern.

The phase-shift property of the Fourier transform states that a shift in the spatial domain corresponds to a phase shift in the frequency (or wave number) domain. Based on this principle, it is possible to create phase variations in antenna arrays through their geometrical distribution. Figure 2.14 shows an antenna displacement by a vector $\vec{d}$ on the left, and on the right, several antennas translated to different locations and weighted by a factor a_n.

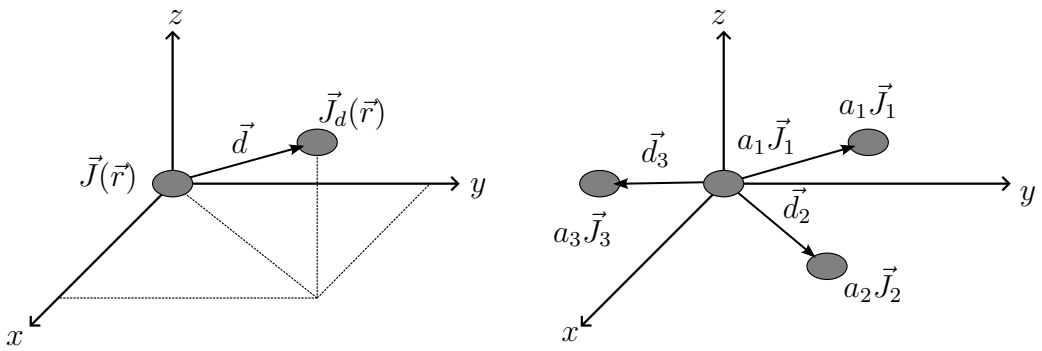

Figure 2.14: Translational antenna array.

The current density of a single translated antenna is $\vec{J}_d(\vec{r}) = \vec{J}(\vec{r}-\vec{d})$. The three-dimensional Fourier transform of the current density will be:

$$\vec{F}_d = \int e^{j\vec{k}\cdot\vec{r}}\vec{J}_d(\vec{r}) \quad \mathrm{d}^3\vec{r} = \int e^{j\vec{k}\cdot\vec{r}}\vec{J}(\vec{r}-\vec{d}) \quad \mathrm{d}^3\vec{r} = \int e^{j\vec{k}\cdot(\vec{r'}+\vec{d})}\vec{J}(\vec{r'}) \quad \mathrm{d}^3\vec{r'}$$
$$= e^{j\vec{k}\cdot\vec{d}} \int e^{j\vec{k}\cdot\vec{r'}}\vec{J}(\vec{r'}) \quad \mathrm{d}^3\vec{r'} = e^{j\vec{k}\cdot\vec{d}}\vec{F},$$

where $\vec{r'} = \vec{r} - \vec{d}$ and $\vec{F} = \int e^{j\vec{k}\cdot\vec{r'}}\vec{J}(\vec{r'}) \quad \mathrm{d}^3\vec{r'}$. Therefore, the radiation vector of the translated element can be written as:

$$\vec{F}_d(\vec{k}) = e^{j\vec{k}\cdot\vec{d}}\vec{F}(\vec{k}). \tag{2.59}$$

Now consider an array of identical antennas at the positions $\vec{d_1}, \vec{d_2} \ldots \vec{d_n}$, with relative complex weights $a_1, a_2 \ldots a_n$ as illustrated in Figure 2.14.

The current density at the n-th antenna is $\vec{J_n}(\vec{r}) = a_n\vec{J}(\vec{r} - \vec{d_n})$ and the corresponding radiation vector is:

$$\vec{F_n}(\vec{k}) = a_n e^{j\vec{k}\cdot\vec{d_n}}\vec{F}(\vec{k}). \tag{2.60}$$

The total current density of the array is the superposition of the individual currents:

$$J_{tot}(\vec{r}) = a_0\vec{J}(\vec{r} - \vec{d_0}) + a_1\vec{J}(\vec{r} - \vec{d_1}) + a_2\vec{J}(\vec{r} - \vec{d_2}) + \ldots, \tag{2.61}$$

and the total radiation vector is the sum of the individual radiation vectors:

$$\vec{F}_{\mathrm{tot}}(\vec{k}) = \vec{F_0} + \vec{F_1} + \vec{F_2} + \cdots = a_0 e^{j\vec{k}\cdot\vec{d_0}}\vec{F}(\vec{k}) + a_1 e^{j\vec{k}\cdot\vec{d_1}}\vec{F}(\vec{k}) + a_2 e^{j\vec{k}\cdot\vec{d_2}}\vec{F}(\vec{k}) + \ldots, \tag{2.62}$$

where the factor $\vec{F}(\vec{k})$ is the radiation vector for a single antenna at the origin (the element pattern). It is possible to define the array factor as:

$$A(\vec{k}) = a_0 e^{j\vec{k}\cdot\vec{d_0}} + a_1 e^{j\vec{k}\cdot\vec{d_1}} + a_2 e^{j\vec{k}\cdot\vec{d_2}} + \ldots. \tag{2.63}$$

It is now possible to express the total radiation pattern of the array as the product of the array factor and the element pattern:

$$F_{\mathrm{tot}}(\vec{k}) = A(\vec{k})\vec{F}(\vec{k}). \tag{2.64}$$

The radiation intensity and power gain of the array can be calculated by the array factor, and the radiated intensity and power gain are described in Equation 2.4 and 2.15.

$$U_{\mathrm{tot}}(\theta,\phi) = |A(\theta,\phi)|^2 U(\theta,\phi),$$
$$G_{\mathrm{tot}}(\theta,\phi) = |A(\theta,\phi)|^2 G(\theta,\phi). \tag{2.65}$$

Chapter 3

Quad-Ridge Feed Horn

Many applications require broadband operation with dual polarization, increasing the potential data volume in the channel. In an RF front-end, the first block after the antenna to deal with each polarization is the Orthomode Transducer (OMT), which separates the incoming signal into specific bands or polarizations. One of the components limiting bandwidth is the monomodal propagation of a rectangular waveguide, which can be overcome at the expense of increased manufacturing difficulty by implementing ridges to increase the monomodal bandwidth [51].

One of the techniques used for reducing the manufacturing difficulty for complex structures, at low cost, is 3D printing, but the current state of metal printing technology increases the surface roughness, resulting in accuracy losses [47], [50]. In [38], polarization combination is achieved using a septum, which demonstrates excellent simulation results but is very sensitive to manufacturing tolerances. Other computational results are also demonstrated in [14], showing promising reflection coefficients. However, they have not been manufactured, and therefore it is impossible to analyze its manufacturability.

The insertion of coaxial cables directly into the ridge structure has been observed in the field of radio astronomy [36], [25] and [41]. As observed in [21] and [17], such configuration might lead to trapped modes in the OMT, which can be mitigated through the insertion of beryllium copper shorting pins and an absorber. Nonetheless, [36] and [4] are able to mitigate the excitation of the trapped modes by using pyramidal and conical cavities back to the feed point and by keeping the ridges closely spaced to each other.

In [45] and [16], a dielectric lens structure is used within the horn. In addition to providing a reduction in (1) the return loss for wide bands and (2) in the size of the horn, it also improves efficiency by correcting the intrinsic phase error of the horns (70 %). This option, however, requires a further investigation regarding the uniformity, isotropy and adhesive layers of the dielectric material [41].

Differential excitations are common in applications that require large-bandwidth and low common-mode noise. This type of excitation can be achieved using the quadraxial feed as reported in [29], [34] in addition to an exponential sidewall profile. As observed in [22] and [23], this profile, in conjunction with straight conical, leads to a rotational symmetry and better stability of the radiation pattern over a wide frequency range when compared with rectangular and diagonal shapes.

To achieve a better manufacturability and post-fabrication tuning of the structure, the antenna is made using a modular assembly approach as described in [54]. The main difficulty is to ensure the manufacturing tolerances for each piece.

This chapter discuss the design, manufacturing and test of two Quad-Ridge Antenna (QRA) Horns with square and conical sidewalls. Also is investigated two kind of feeding systems: the coaxial feeding and the quadraxial feeding.

3.1 Square Quad-Ridge Horn Antenna

The Square Quad-Ridge Horn Antenna (SQRA) structure can be seen in Figure 3.1, divided into two main parts: the transition from a coaxial cable to a quad-ridge waveguide and the exponential transition between the waveguide and the horn.

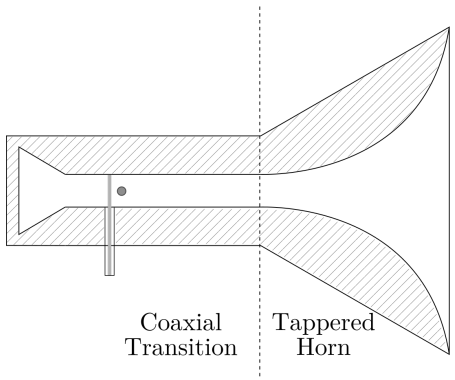

Figure 3.1: Design of the quad-ridge horn antenna.

The end of the quad-ridge waveguide is marked by a pyramidal-shaped cavity used to achieve impedance matching and prevent modes from getting trapped in the structure, leading to disturbances in the radiation pattern [21].

The ridges have a 45° chamfer with a flat part in the center, which helps prevent the formation of higher-order modes by narrowing the gap between ridges. The suppression of such high-order modes, as discussed in section 2.3, broadens the operating frequency range of the waveguide.

3.1.1 Design Procedure

The quad-ridge waveguide consists of a square waveguide with a side length of 40 mm. Since there is no closed-form analytical solution to obtain the initial parameters of the ridges, a simplified simulation of the waveguide is initially conducted. The best dimensions were then extracted from this simulation to achieve an approximate characteristic impedance of 50 Ω for the waveguide.

Similarly, quad-ridge horn antennas also lack a closed-form analytical solution. Therefore, the most effective way to obtain results is through a purely numerical analysis using Ansys

High Frequency Structure Simulator (HFSS). The key parameters varied in the analysis were the horn aperture and length, with a focus on the ratio between these two parameters.

3.1.2 Ridge waveguide characteristics

Ridge waveguides are employed when there is a need to achieve a broad bandwidth, provided that the criteria for exciting the necessary modes are met [7], [2], [51]. The first five simulated modes of the square waveguide used can be observed in Figure 3.2, illustrating the mode excitation in a 40 mm long waveguide through the transmission parameter, as shown in Figure 3.3.

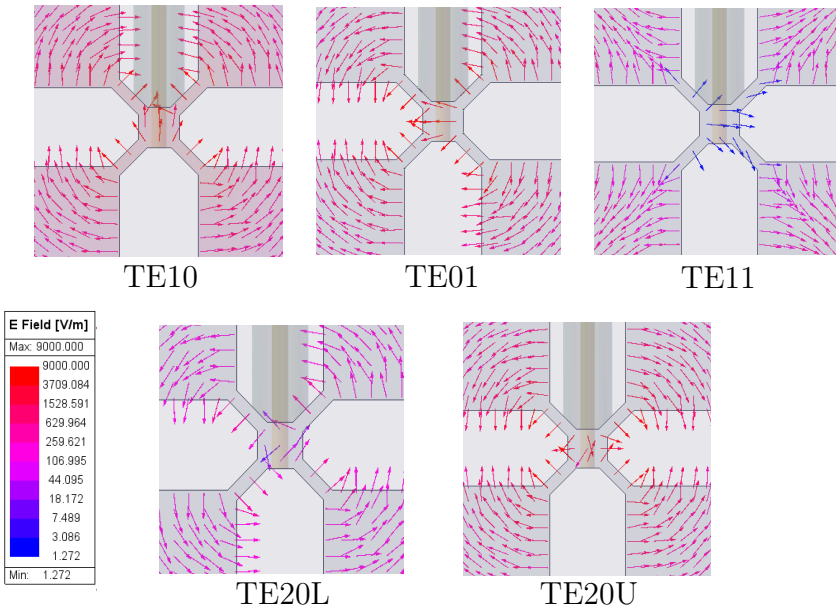

Figure 3.2: Modes in the quad-ridge waveguide by excitation from a coaxial pin with 1 V .

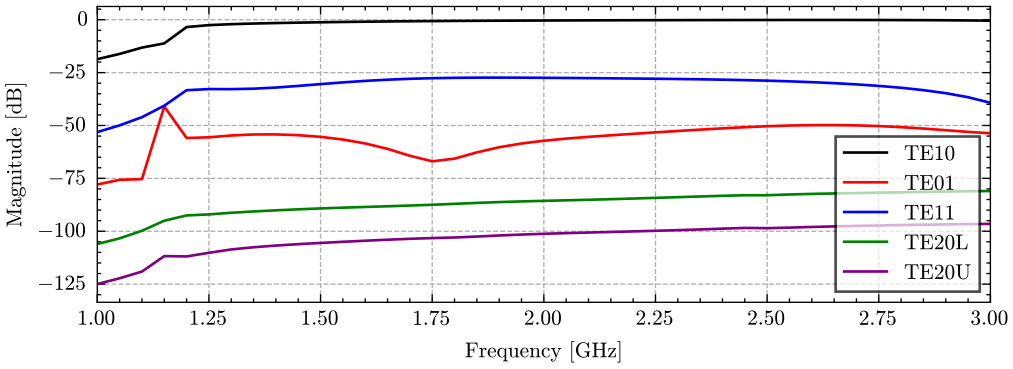

Figure 3.3: Propagation of modes in a square quad-ridge waveguide in function of frequency.

The first mode pair excited is shown in Figure 3.2, consisting of TE10 and TE01 modes. These modes are orthogonal to each other and occur in square geometries. The orthogonality enables isolation between modes, making such a waveguide model suitable for transitions with coaxial cables placed in orthogonal positions. Higher-order modes include TE20L, TE20U,

and TE11. Note that after the TE11 mode is suppressed due to the geometry of the pin, the bandwidth up to the next higher modes (TE20L) is considerably high.

3.1.3 Transition design

As mentioned in Section 3.1.2, the suppression of higher-order modes is achieved by narrowing the gap. However, this must be done while adhering to the manufacturability constraints of the model. In this regard, the initial approximation for the size of the quad-ridge is based on an analysis of the waveguide impedance in the required band. The goal is to achieve a value close to 50 Ω across the entire operating band, making the matching with the coaxial cable more efficient [36]. The dimensions found to be closest to this goal can be seen in Figure 3.4.

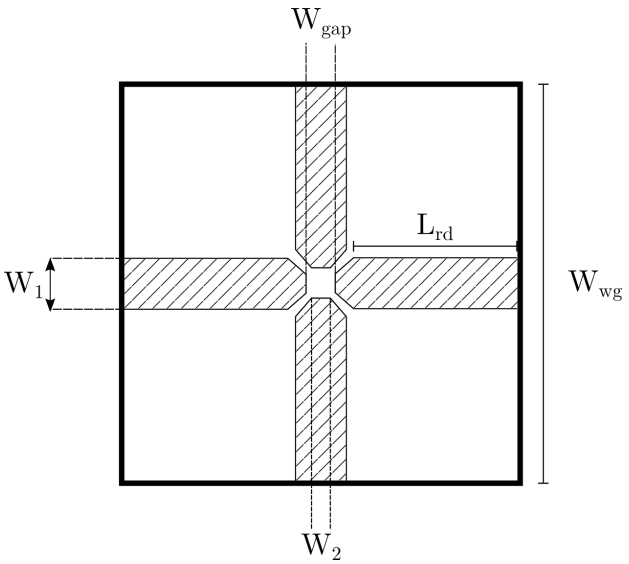

Figure 3.4: Dimensions of the quad-ridge waveguide. The variables values are $W_{wg} = 40\,\text{mm}$, $W_{gap} = 3.3\,\text{mm}$, $W_1 = 6.35\,\text{mm}$, $W_2 = 1.95\,\text{mm}$, $L_{rd} = 16.15\,\text{mm}$.

The geometric positioning of the coaxial cables forces a current distribution that favors the TE10 modes over others. The insertion of coaxial feeders into the structure can be seen in Figure 3.5.

Since this is a waveguide, it is necessary to match the wave reflected from rear wall as well. Otherwise, depending on the wavelength, the reflected wave may reach the feeder with a phase inversion, resulting in a destructive interference. The construction of this rear wall can take various forms, such as a spherical [18], a square cavity [39], an L-shaped cavity [43], conical [43], or pyramidal [36]. As the literature suggests, the pyramidal design yielded the best results, as seen in Figure 3.5.

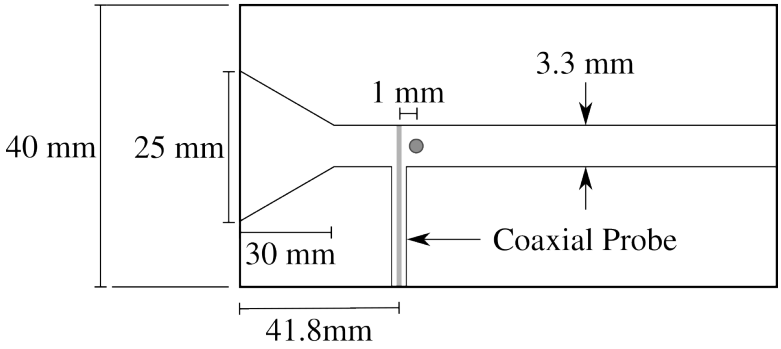

Figure 3.5: Dimensions of the length and width of the backshort.

3.1.4 Ridge Shape

Although the horn shape has a closed-form solution for finding optimal dimensions depending on the specifications, the use of a ridge waveguide also requires the insertion of a ridge into the horn, as seen in Figure 3.6. The profile must be designed to facilitate the transition between the air impedance ($377\,\Omega$) and the waveguide impedance. In this regard, various types of profiles are used to achieve a smooth transition between these impedances, as indicated in [37], [42], [23], and can also extend to the horn shape [22].

In [37], a comparison of various profiles for ridge antennas is made, where the exponential profile is observed to have better performance, given by the equation 3.1. In [27], a routine is described to find the best dimensions for the horn antenna: first, the horn aperture is determined, which directly influences the edge taper ($-11\,\mathrm{dB}$) for the parabolic reflector. After the transition length is determined, it is simulated for various values of the ratio between the aperture and the length. It is observed that values close to unity are the most reasonable.

$$y(z) = \frac{g}{2}e^{kz}, \quad k = \frac{1}{RA}\ln\left(\frac{A}{g}\right), \quad 0 \leq z \leq 1. \tag{3.1}$$

The observed angle to the edge of the parabola that will be used with the horn is approximately 27°. In this regard, an aperture of approximately 30° is established, considering that the designed horn may be larger than the original horn used in the parabola, requiring a larger angular aperture.

After the simulations using ANSYS High-Frequency System Simulation, the optimal dimensions for the horn can be seen in Figure 3.6.

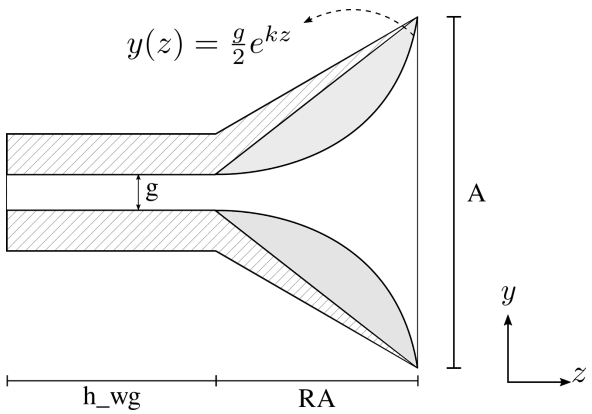

Figure 3.6: The horn and ridge dimensions are $g = 3.3\,\text{mm}$, $h_{wg} = 40\,\text{mm}$, $R_A = 355\,\text{mm}$, $A = 32\,\text{mm}$.

3.1.5 Complete simulation

Combining all the previously discussed elements into a single model in Ansys HFSS resulted in a complete horn structure. The return loss parameters feeding the antenna with the two coaxial cables can be seen in Figure 3.7. The maximum observed return value is $-18.5\,\text{dB}$ between $2.2\,\text{GHz}$ and $2.3\,\text{GHz}$. The minimum value for port isolation is $48\,\text{dB}$ at $2.3\,\text{GHz}$. The impairment observed between the S_{11} and S_{22} is due to the offset between the pins.

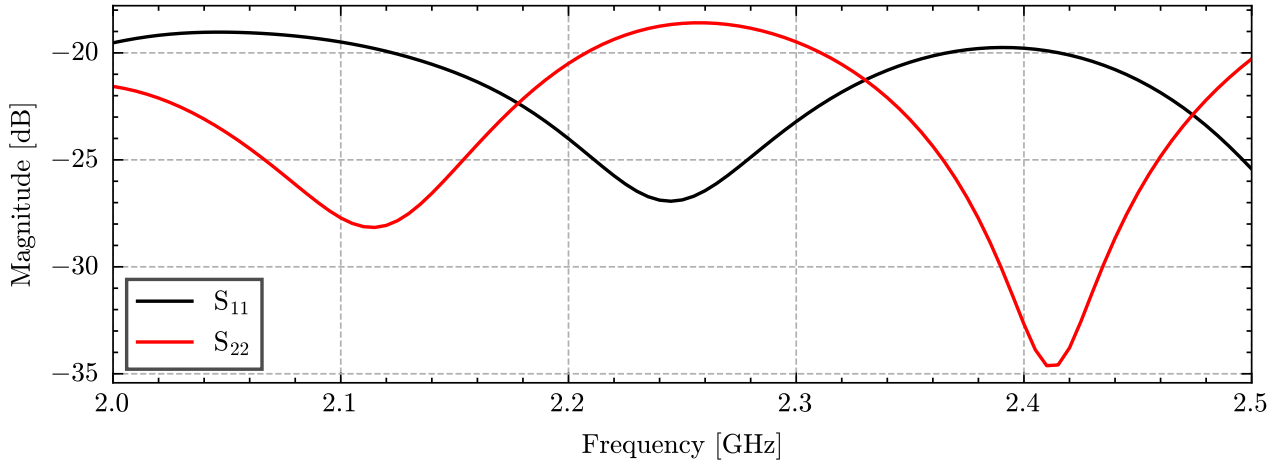

Figure 3.7: Simulated variation in S_{11} parameter in function of variation of the variable value.

The maximum observed gain of the antenna is approximately $11\,\text{dB}$ at $2.2\,\text{GHz}$, with a $-11\,\text{dB}$ beamwidth of 29.7°, as shown in Figure 3.8. The cross-polarization can be seen in blue in Figure 3.8, with a peak value of $-25\,\text{dB}$ which is approximately $15\,\text{dB}$ below the main polarization at the same angular point.

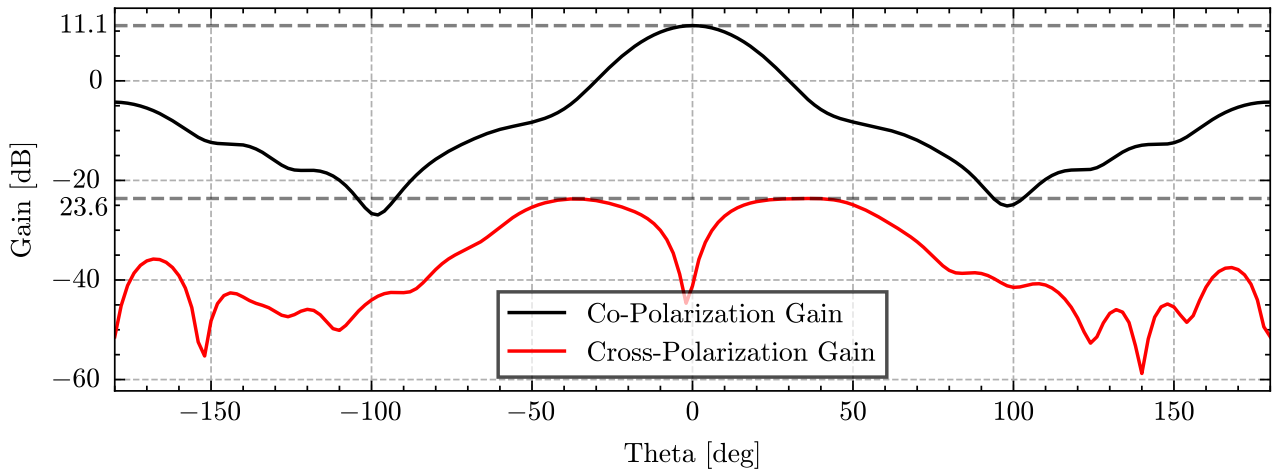

Figure 3.8: Polarization and cross polarization.

3.1.6 Yield Analysis

After the design and simulation of the horn antenna, it is necessary to establish the tolerances of the manufacturing process. For this purpose, a sensitivity analysis is conducted for each component of the structure, based on an analysis of the performance variation with respect to the deviation of the variables that model each part of the antenna. Since this involves discrete variation, the finite difference method is employed.

A second-order differentiation for three variation points is given by Equation 3.2.

$$\frac{\partial^2 f}{\partial x^2} \simeq Af(x-h) + Bf(x) + Cf(x+h), \tag{3.2}$$

where A, B, and C are weighting constants that will determine the differentiation. To find these constants, a Taylor series expansion up to the second order is performed for each sampled point, resulting in Equation 3.3.

$$\begin{aligned}\frac{\partial^2 f}{\partial x^2} =& Af(x) + Af'(x)(-h) + \frac{A}{2!}f''(x)(-h)^2 + \cdots \\ & Bf(x) + Cf(x) + Cf'(x)(h) + \frac{C}{2!}f''(x)(h)^2.\end{aligned} \tag{3.3}$$

From Equation 3.3, we want to find the values of the constants that result only in the second-order derivative. Thus, we have the matrix given by Equation 3.4, whose solution is provided in Equation 3.5.

$$\begin{bmatrix} 1 & 1 & 1 \\ -1 & 0 & 1 \\ 1 & 0 & 1 \end{bmatrix} \cdot \begin{bmatrix} A \\ B \\ C \end{bmatrix} = \begin{bmatrix} 0 \\ 0 \\ \frac{2!}{h^2} \end{bmatrix}. \tag{3.4}$$

$$\begin{bmatrix} A \\ B \\ C \end{bmatrix} = \begin{bmatrix} 1 & 1 & 1 \\ -1 & 0 & 1 \\ 1 & 0 & 1 \end{bmatrix}^{-1} \cdot \begin{bmatrix} 0 \\ 0 \\ \frac{2!}{h^2} \end{bmatrix}. \tag{3.5}$$

Generalizing in the format of Equation 3.6, where n is the power in the Taylor expansion (or the number of rows of the matrix), c_k is the coefficient to be found, s_k are the sampled points, with N being the total number of samples, and m is the order of the derivative to be found.

$$\frac{\partial f^m}{\partial x^m} = \sum_{k=1}^{N} s_k^n c_k = \frac{m!}{h^m}\delta(n-m). \tag{3.6}$$

The solution for the coefficients can be found in matrix form in Equation 3.7, which is easily implemented computationally.

$$\begin{bmatrix} c_1 \\ \vdots \\ c_N \end{bmatrix} = \frac{1}{h^d} \begin{bmatrix} s_0^0 & \dots & s_N^0 \\ \vdots & \ddots & \vdots \\ s_0^N & \dots & s_N^N \end{bmatrix}^{-1} \cdot \begin{bmatrix} 0 \\ \vdots \\ m! \\ \vdots \\ 0 \end{bmatrix}. \tag{3.7}$$

This solution is implemented in a Python script, which performs analyses of the variation in reflection coefficients and gain variations. Table 3.1 shows the most critical variables in the design. It can be seen that greater attention should be given to the variables that dictate the gap between ridges, the chamfer, the Teflon height, and the matching ring radius.

Table 3.1: S_{11} variation derivatives for the most critical variables.

Variable Name	**1° Derivative**	**2° Derivative**
Gap between ridges	$-43,45$	$5896,56$
Chamfer	$-35,70$	$7535,42$
Back short height	$-3,47$	$3607,00$
Back short weight	$-1,79$	$-935,03$
Teflon Height	$-16,52$	$536,98$
Ring match radius	$15,71$	$3464,98$
Position of coax.	$10,97$	-1238

The graph in Figure 3.9, for example, shows the prediction variation for the gap distance using the second-order Taylor series derivatives, from which it is now possible to extract tolerances for the design.

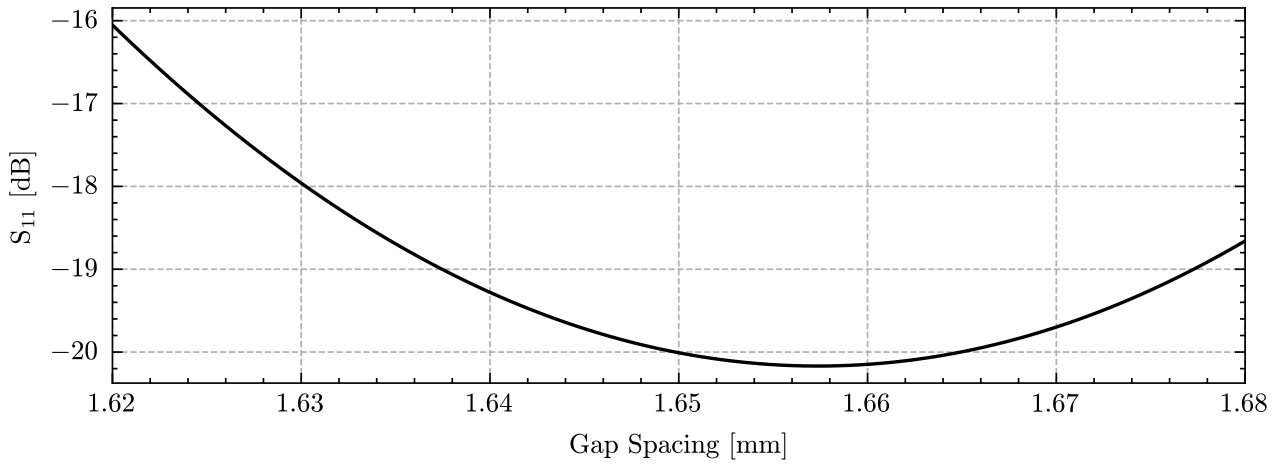

Figure 3.9: Estimated variation in S_{11} parameter at 2.2 GHz as a function of variation of the variable value.

3.1.7 Fabrication and Measurement

The manufactured square quad-ridge antenna is shown in Figure 3.10. The sidewalls were made from galvanized steel, cut with laser beam machining, and conformed with a sheet metal bending machining. The aluminium ridges were manufactured with Computer Numerical Control (CNC) milling machining. All the parts were assembled with Metal Inert Gas (MIG) welding and screws.

Although most of the processes used were automated, the welding and assembly were not. The use of sheet metal is not dimensionally stable under manufacturing and assembly stresses, which results in large deviations. The choice to use galvanized sheet metal is also a poor decision, as it is difficult to weld due the zinc coating on the surface.

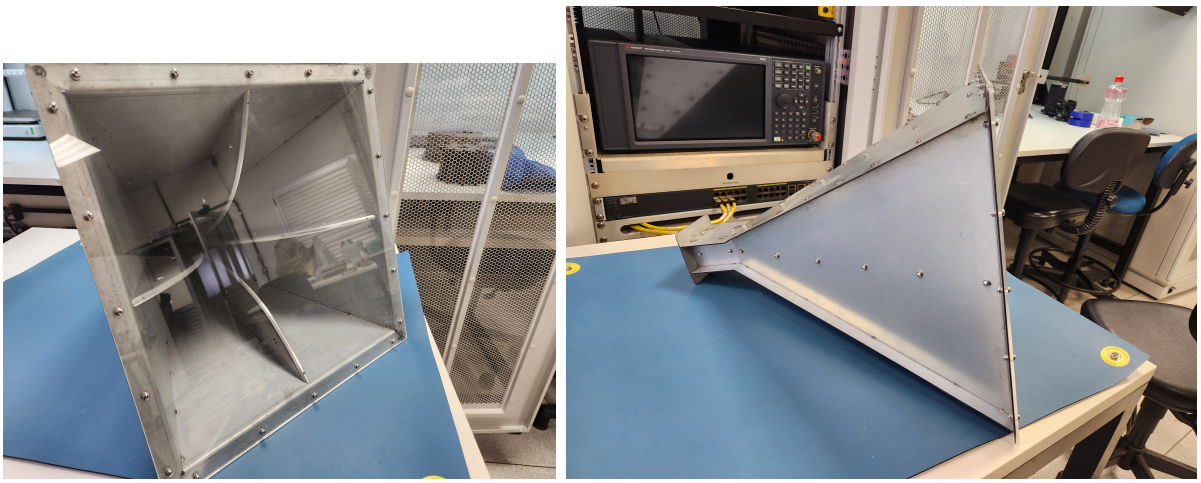

(a) (b)

Figure 3.10: Manufactured square quad-ridge horn antenna: (a) a diagonal view, and (b) a side view.

The milling machining exerts a cutting pressure on the workpiece. Aluminium 6061 is employed in the ridge construction, but it is not a dimensionally stable alloy under machining stress. This leads to a roughness surface and a dimension deviation.

As discussed in the Section 3.1.6, the antenna's impedance matching is highly sensitive to ridge tolerances. The ridge positioning is also related to the correct alignment of the sidewalls. The rear view of the antenna is shown in Figure 3.11, where is possible to see the pyramidal backshort and the coaxial feeding.

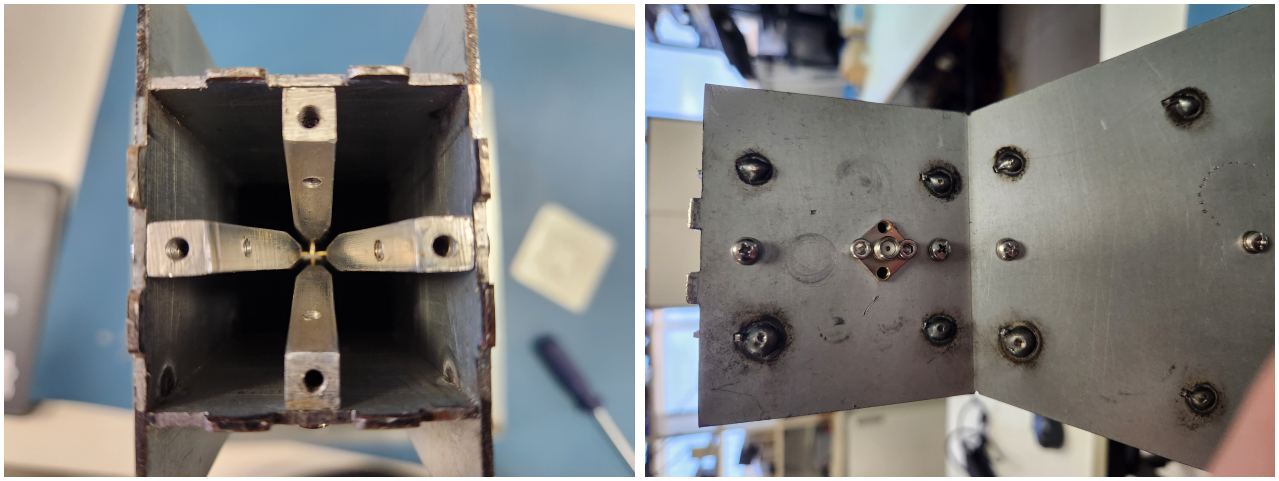

(a) (b)

Figure 3.11: Manufactured square quad ridge horn antenna: (a) a rear view, and (b) a side view.

The measured S-parameters with the Vector Network Analyzer (VNA) are seen in Figure 3.12. The return loss for both ports is better than −10 dB between 2.1 GHz-3 GHz, which corresponds to a 34 % fractional bandwidth centered at 2.55 GHz. The coupling between ports is below −20 dB over the entire band.

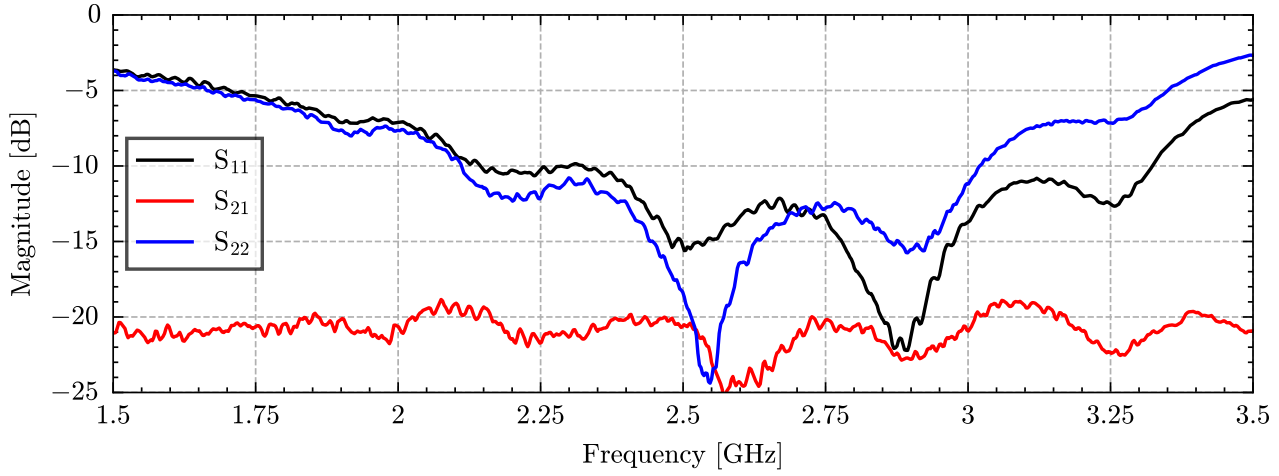

Figure 3.12: Measured S-parameters of the square quad-ridge horn.

The measurement result shows that the impedance matching for this antenna, however, is near to the limit of the −10 dB around 2.2 GHz which is the satellite's center frequency of operation. This result did not improve, even after adjustments.

3.2 Low-Cost Tunable Compact and Modular Broadband Dual-Polarization Conical Horn Antenna

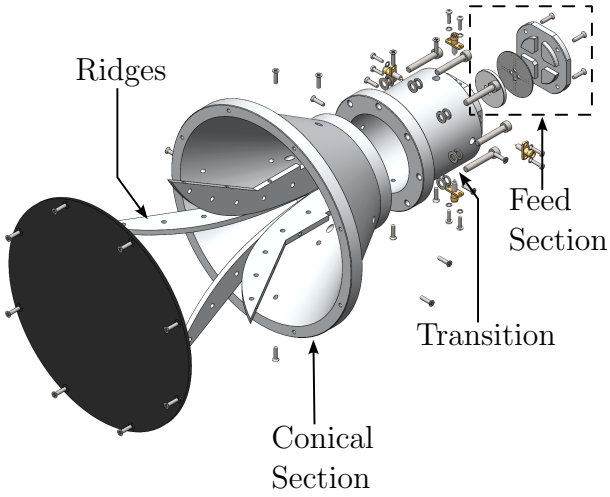

Figure 3.13: Exploded view of the modular horn antenna.

Although the pyramidal antenna described above presents a good impedance matching over the frequency band of interest for the VCUB1 satellite operation, the antenna is too large for the use as a feed for a parabolic reflector. Its large size and weight creates a large shadowing region on the parabolic reflector.

Taking that in consideration, this section presents a low-cost tunable and broadband conical horn antenna with quadraxial feeding that is a differential feeding approach. The assembly uses a modular design in order to allow further adjustments, in association with grooves for the ridges, which enables an antenna electrical tuning even after the antenna fully assembly. The first part consists in a description of the geometry of the horn, followed by the design procedures for each part of the structure. The second part is a brief discussion about the mechanical features of the structure and the methods for manufacturing. Finally, the simulation results using Ansys HFSS are compared with measured data in an anechoich chamber.

3.2.1 Design and Optimization

The design of the horn is divided into three sections: feed system, throat and flared sections. All three parts are designed to be modular and manufactured separately, as shown in Fig. 3.13. The ridge has been manufactured using a single piece and is mounted on both the flared and throat sections.

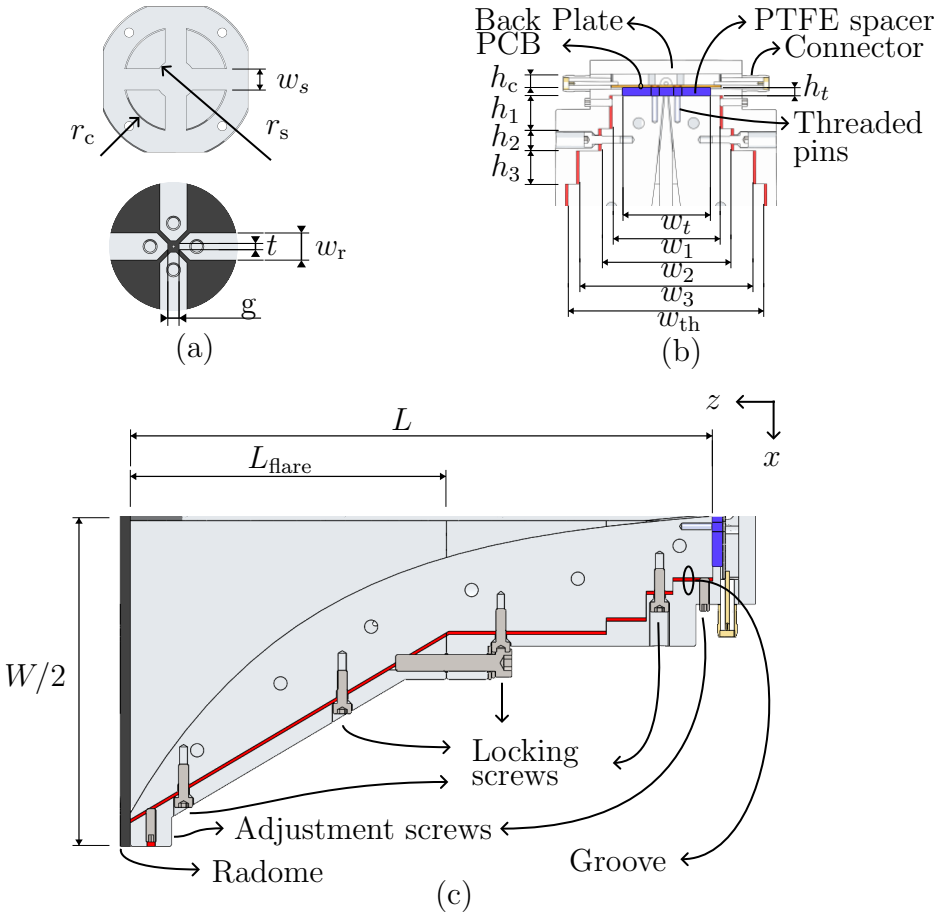

Figure 3.14: Dimensions of the horn antenna in (a) the aluminium backplate design; (b) a detailed view of the throat section; (c) a transverse section cut of the antenna. In red is the ridge groove and in blue is the PTFE spacer.

The dimensions parameters are shown in Fig. 3.14 that comprehends a section view of the antenna, a detailed view of the throat section, ridges and backplate dimensions. The dimensions of the main structure variables are listed in Tab. 3.2.

The feed system employs the quadraxial feed technique [29]. The feed consists of a Printed Circuit Board (PCB) that interfaces the SMA connector to the pins that feed the ridges differentially. The PCB uses a Arlon AD450 substrate with 0.762 mm of thickness. Edge plating is used in order to improve electrical contact and impedance transition between the PCB and the antenna body. Feed lines are designed for 50 Ω characteristic impedance as a grounded coplanar waveguide structure and the aluminium backplate as a cover. The aluminium backplate is designed to reduce the coupling the ports to avoid the excitation of resonant cavity modes.

Adding extruded paths to the aluminium backplate improves port-to-port isolation and the mode purity by confining the electromagnetic field, as shown in Fig. 3.15a with ports excited differentially with 1 V of amplitude. Without these paths, the electromagnetic field within the PCB cavity with height h_t and radius r_c tends to spread between feedlines and excite resonant cavity modes, as illustrated in Fig. 3.15b. As the aluminium backplate is removable, it expose the PCB to further adjustments as in case of cold soldering.

Table 3.2: Optimized dimension variables for the antenna.

Param.	[mm]	Param.	[mm]	Param.	[mm]
H	160	h_3	12	g	2.8
L	175	w_1	36	L_{flare}	95
W	180	w_2	44	r_{c}	68
h_c	4	w_3	66	r_{s}	40
h_{t}	3	w_{r}	4.76	w_{s}	32
h_1	12	t	1	d_{pin}	1.5
h_2	8	w_{t}	32	R	0.018

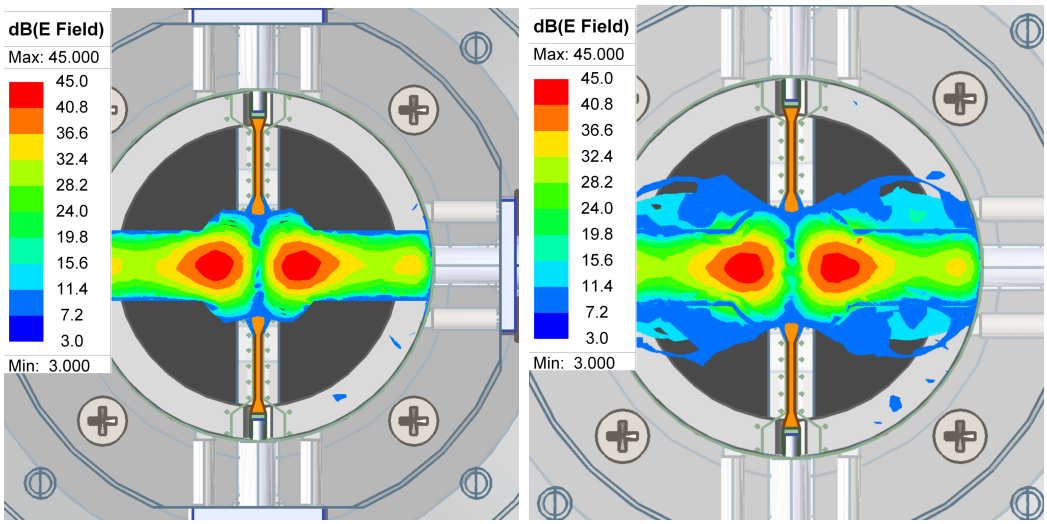

(a) (b)

Figure 3.15: Field distribution for 1 V of differential pair excitation in dB(V m^{-1}) inside the PCB cavity when (a) the cavity is guided and (b) when cavity is not guided by the aluminium backplate extruded paths.

The spacing between pins and pin radius dictates the minimum possible gap (g) in terms of manufacturability. A reasonable value of $g = 2.8$ mm is adopted, and a pin radius of 1.5 mm. The pins are made with brass to facilitate soldering; however, since brass is a soft alloy, it is necessary a Polytetrafluoroethylene (PTFE) spacer to ensure the mechanical stability and robustness as shown in blue at the Fig. 3.14b. The spacer improves the throat input impedance, since it is the interface of the ridge to PCB pins. An optimized value of $h_t = 3$ mm thick is adopted.

The throat section is designed to ensure 100 Ω of differential impedance. To improve the mode purity, at the beginning of the section there are four steps to provide a smooth impedance transition between the quadraxial feed system and the quad-ridge waveguide, as discussed in [34]. This method also improves the stability of the radiation pattern once is limited to a monomodal propagation over the band.

The flared section has a conical sidewall which simplifies manufacturing. However, the ridges that interface the quadraxial feed to make the smooth transition to free-space impedance follow the exponential profile of Eq. 3.8.

$$x = \left(\frac{W-g}{2(e^{RL}-1)}\right)e^{Rz} + \left(\frac{ge^{RL}-W}{2(e^{RL}-1)}\right), \tag{3.8}$$

where, W is the horn aperture diameter, g is the distance between the ridges, R is the opening rate, L is the total horn length and z is the axial component, following [34], where it is discussed a modal-based method to determine the parameters.

To protect internal structure of the antenna, there is a 3 mm thick polycarbonate radome of relative dielectric constant of $\varepsilon_r = 2.9$ and loss tangent of $\tan\delta = 0.0065$. Such material is widely available and is resistant to most outdoor environment conditions, as discussed in [52].

3.2.2 Manufacturing

Manufacturing follows the principle of modularity, accomplished by designing the parts to be assembled with a set of screws that ensure the alignment. The throat and flared sections are manufactured using a manual lathe machine and the backplate using a milling machine. The ridges and the grooves are machined with wire Electrical Discharge Machining. The manufactured antenna is shown in Fig. 3.16.

The antenna is entirely made of aluminium and steel except for the PCB, the PTFE spacer, PCB to ridge pins and SMA connectors, as shown in the section view of Figs. 3.14a and 3.14b. One of the challenges of manufacturing is the high sensitivity of S-parameters of the antenna to ridge dimensions and gap. The ridges are made out of steel due its dimensional stability in the Electrical Discharche Machining process compared to aluminium.

Each ridge present six holes that are used to fix the raw steel piece during the EDM process, ensuring the piece stability. The addition of these holes influences the radiation pattern and impedance matching, being compensated in the simulation steps as discussed in Section 3.2.3.

To permit the adjustment of the gap, a groove has been machined through EDM in the flare and the throat sections at the positions of the ridges as shown in red on Figs. 3.14a and 3.14b. A set of adjustment screws is also introduced to push the ridge to the right position. By moving the screws it is possible to adjust the gap spacing and the opening ratio R of the antenna. The adjustments drastically relax the tightness manufacturing tolerances while also permits a degree of freedom in the electrical proprieties including the change of the operating band limited by the throat section.

3.2.3 Simulations and Measurements

Electromagnetic simulations have been performed using Ansys HFSS, optimizing the antenna performance at 2.2 GHz. Due to the differential feeding, the S-parameters are analyzed in mixed-mode through terminal ports. Data is normalized to 100 Ω, for differential-mode, and the standard 50 Ω for the common-mode ports.

After the first iteration of simulations, the main dimensions are made available for me-

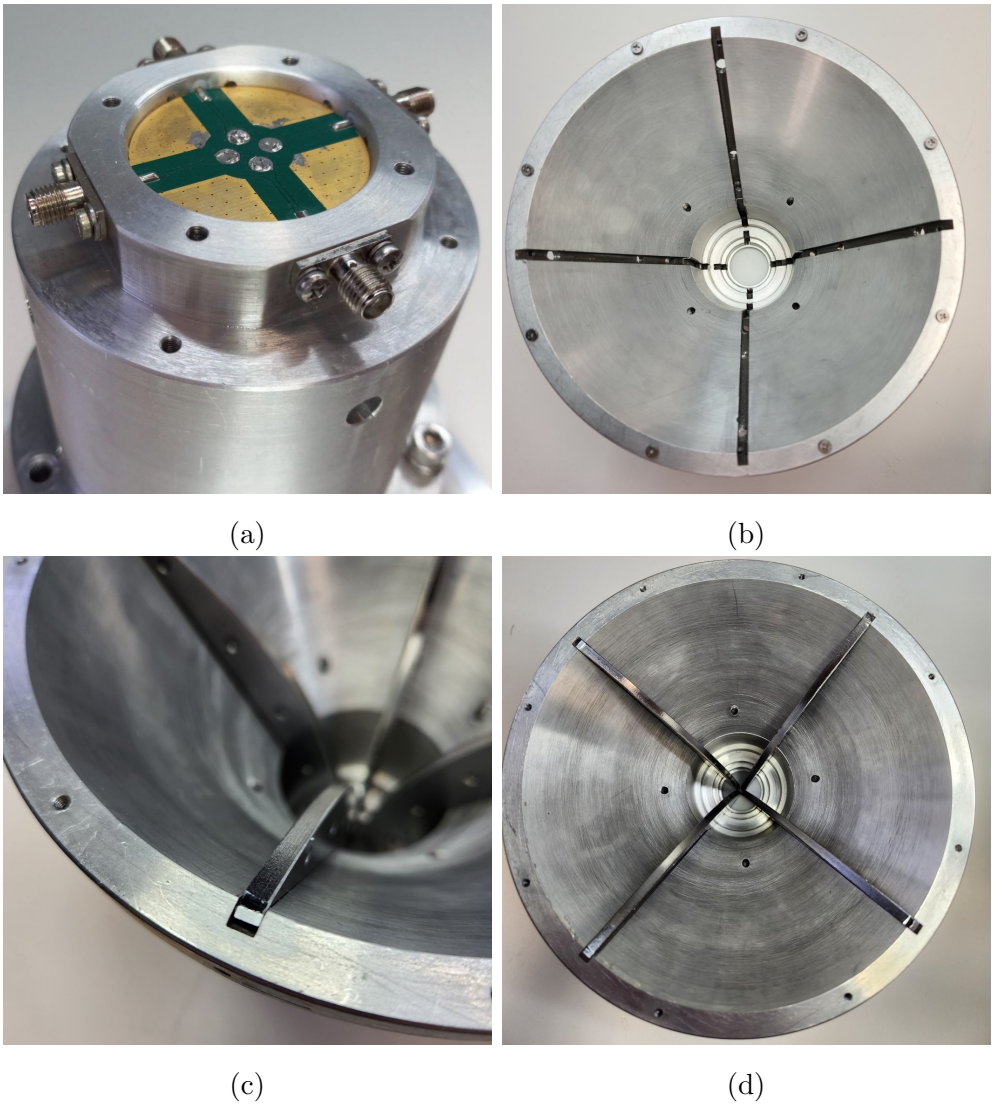

(a) (b)

(c) (d)

Figure 3.16: Pictures of the manufactured antenna (a) exposed PCB and brass pins soldered in; (b) grooves for ridge adjustment; (c) ridge after mounting and adjusting on the grooves; (d) top view of the antenna fully assembled except for the radome.

chanical design. After the mechanical adjustments are made, the 3D model is simulated and modified in a set of iterations to compensate the electrical performance of the antenna due to the influence of the screws and ridge holes. The analyzed results lie in the S-band, that covers 2 GHz to 4 GHz.

3.2.4 Simulated and Measured Results

The quad-ridge horn antenna described in section 3.2.1 is characterized using a Keysight P5024 Vector Network Analyzer using 4 ports, where it is possible to extract the mixed-mode S-parameters in real time.

The tuning iterations result in the S-parameters shown in Fig. 3.17. The faded lines are the tuning attempts by the ridge positioning adjustment, while the opaque line is the final

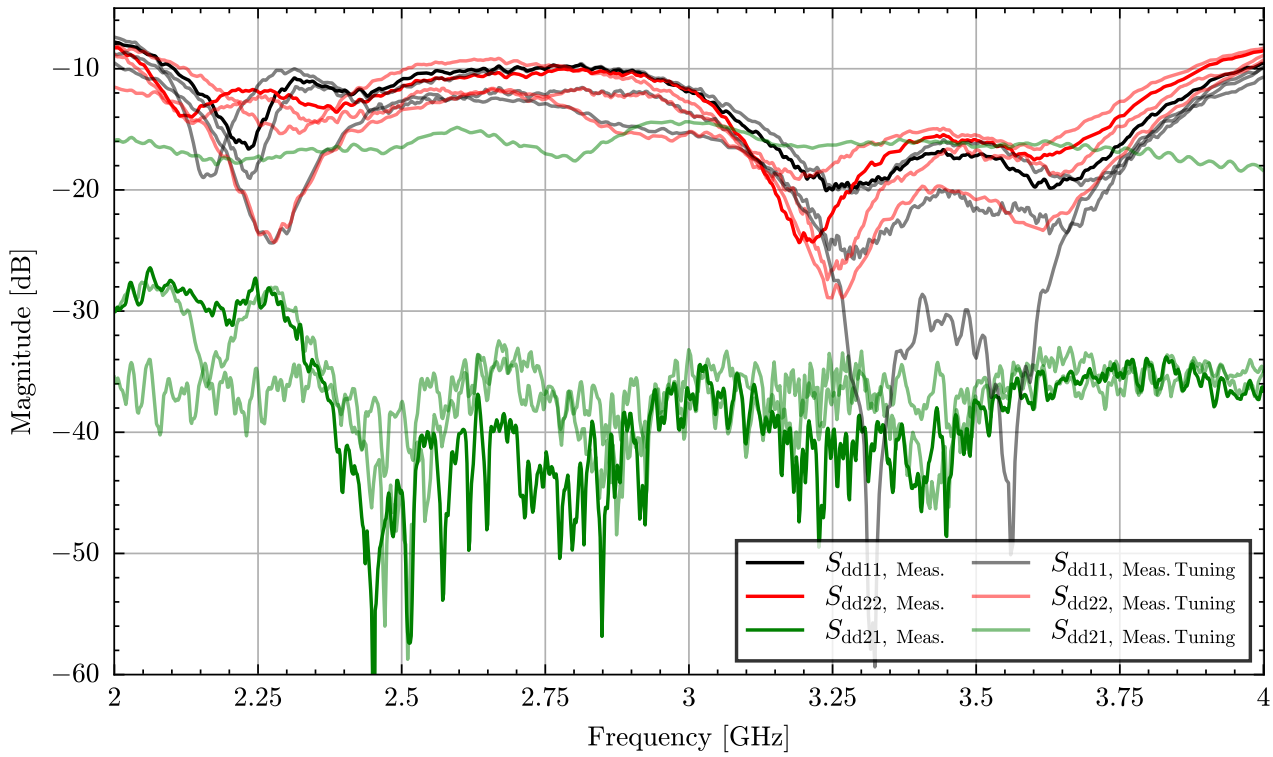

Figure 3.17: Comparison between the possible tuning attempts (faded lines) and the final adopted (opaque lines).

tuning in broadband. The measured value of return loss within the band is below −10.0 dB. The simulated isolation between each differential pair has a peak of 70.0 dB while the measured value is 26.0 dB, but in almost the entire frequency range keep the isolation below −36.0 dB. These results confer a fractional bandwidth of 63 % with the center frequency at 3.0 GHz. It is worthily highlight that this design is simulated to have a response for reflection coefficient below the −10 dB in almost all the band, however the measured value is better and attends all the band between 2.1 GHz-3.9 GHz.

The advantage of this antenna is the reconfigurability. It is shown in Fig. 3.17 the S-parameters behavior with different tunings. Notice that it is possible to enhance the impedance matching in some bands within the S-band by the ridge tuning. Also some tunings results in a better reflection coefficient at the expense of a worst port coupling around −15 dB. Therefore, is possible to have a trade-off between the port coupling and reflection coefficient.

The port asymmetry and resonance frequencies of the differential ports are due to the structural differences of the ridges and the manual adjustment. However, the overall measured values remain better than simulated.

The anechoic chamber used to perform the radiation pattern characterization is shown in Figure 3.18.

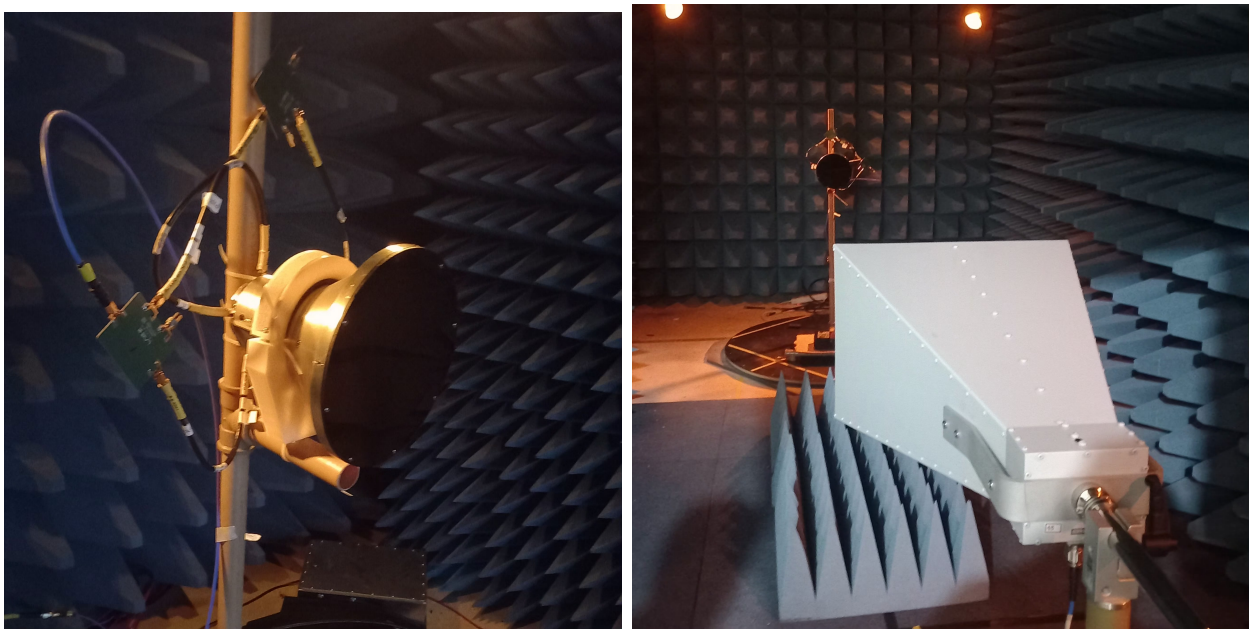

(a) (b)

Figure 3.18: Pictures of the Federal University of Campina Grande (UFCG) anechoic chamber setup:(a) the horn antenna fixed at the tripod on the rotative table and (b) measure setup using a reference horn antenna.

The normalized radiation pattern for the H-plane and E-plane are shown in Fig. 3.19a and 3.19b. In these Figs. is verified that the simulated results and measurement results match specially inside the −10 dB bandwidth, marked as the white region. The mean of the −10 dB aperture is 93° for the H-plane and 64° for E-plane. The simulated radiated peak gain is 11.0 dB, while the measured peak gain is 10.1 dB, both at 2.2 GHz. Such difference is within mechanical tolerance deviations, material roughness and oxidation. The shapes of the radiation patterns for each polarization are similar even after the adjustments.

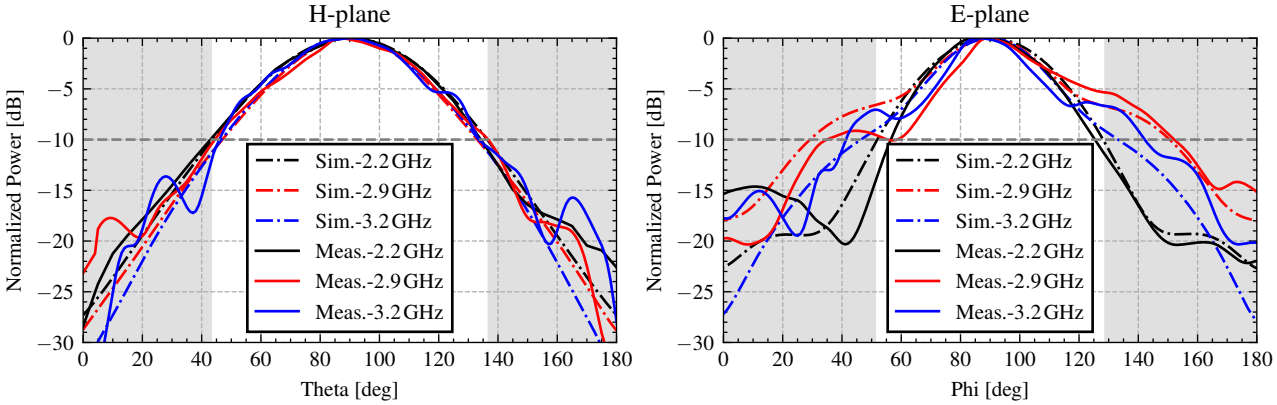

(a) (b)

Figure 3.19: Measured (red) and simulated (dashed) antenna co-polar normalized gain in (a) H-plane and (b) E-plane. The shaded area is the simulated pattern below −10 dB at 2.2 GHz.

Chapter 4

System Design

The system design is guided by two main factors: low cost and reconfigurability. The low-cost goal is achieved by using an antenna with a pre-integrated OMT and the coaxial transition. Reconfigurability is achieved by digitizing the signal within the antenna structure and transmitting it digitally.

To accomplish the second factor, a Software-Defined Radio (SDR) is used for signal digitalization and pre-processing, alongside with a low-noise RF front-end. The signal is then transmitted to a central building for further processing and storage.

In this chapter, the system design and the characterization of each block are discussed in detail. First, an overview of the system is presented, followed by a discussion of the RF front-end design, its characteristics, the SDR programming and synchronization.

4.1 System Overview

A system overview is shown in Figure 4.1. Following the signal chain, the Feed horn receives the signal, which then passes through the RF front-end, the Software Defined Radio, an Ethernet switch, an optical fiber to an indoor switch that distributes the signal to the computational cluster.

As this work aims to use the antennas in a large phased array, it is necessary to synchronize the sampling time and clock of all antenna receivers remotely so that the phase difference between them can be calculated. Such synchronization is critical due to the strong relationship between the signal phase at each antenna, as discussed in Section 2.6. Even if mismatches in signal sampling occur due the sampling time misalignment or clock offset, these deviation quantities must remain fixed over the time so that the system can be calibrated, as discussed further in Chapter 5. To accomplish this requirement, a GPS receiver is installed at each antenna to synchronize all the SDRs remotely and independently.

The SDR employed in this system is the AntSDR E200. It is cost-effective, Ethernet-based and uses the Analog Devices AD9363 transceiver, which is also the same employed in other popular SDRs like ADALM-PLUTO and USRP B205mini. Being Ethernet-based is also a strong point, since communication can be established over longer distances (up to 100 m) than with USB-based SDRs. This capability also enables the use of Ethernet switches and, therefore, the transport of raw data over optical fiber.

The data transport from all the antennas to the indoor cluster employs a pair of single-mode optical fiber using the SFP+ transceiver that can transport up to 20 Gbit/s of data. Such data rate surpasses the current rate of 10 Mbit/s for each antenna, which becomes 160 Mbit/s considering all the sixteen antennas in operation. This approach is employed mainly due to the lower price of fiber optic and its robustness over large distances. This data headroom enables the use of the same infrastructure for other future wideband data signals and/or for the addition of more antennas.

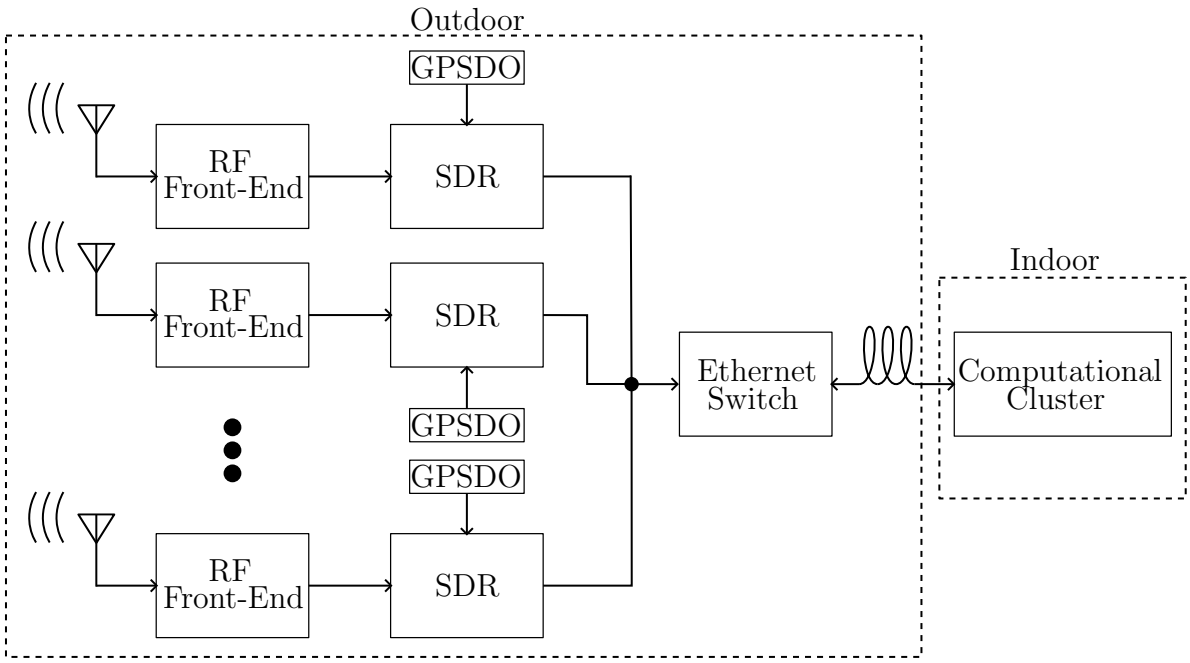

Figure 4.1: Phased array system overview.

4.2 Link Budget Analysis

The link budget is a balance sheet of gain and losses that describes the system in terms of signal and noise power. The main output of the link budget is the link margin, which represents the allowable deviation in system losses in situations where other factors contribute to degrading the useful signal. The details of the link budget analysis are discussed in Section 2.5.2.

This project aims to use the VCUB1 satellite from Visiona Espacial. The satellite works at 2.2 GHz with an EIRP of 40.5 dBm transmitting an image file with 6 MHz of instantaneous bandwidth and a 10 Mbit data rate. Further information is discussed in Section 2.5.1. The recommended E_b/N_0 is 7.5 dB for a successful reception. This information and the link budget analysis are shown in Table 4.1.

The receiver antenna gain is calculated with Equation 2.40 for a 2.4 m parabolic dish with an efficiency of 60 %. The efficiency value is not simulated; this is an estimate using a reasonable value.

The system is designed to operate in clear weather with low wind velocity to protect its

mechanical and electrical integrity. Therefore, an operating temperature of 290 K (ambient temperature) is adopted. The cosmic background noise at this operating frequency is below 10 K, as described in [46] and [40].

Considering a system operating with a maximum receiver noise figure of 2.93 dB, the system has a 3.07 dB of link margin, which is sufficient considering that the system only operates in specific weather conditions.

Table 4.1: Link budget for VCUB1 satellite specifications at 2.2 GHz.

Transmitter Power [mW/dBm]	1584.90	32
Transmitter Circuit Loss [dB]		0
Transmitter Antenna Gain [dBi]		8.50
Terminal EIRP [dBm]		40.50
Path Loss [ ]	2.14×10^{15}	153.30
Fade Allowance [ ]		4
Other Losses [ ]		4
Received Isotropic Power [mW/dBm]		-120.80
Receiver Antenna Gain [dB]	2154.38	33.33
Edge of Coverage Loss [dB]		2
Received Signal Power [dBm]		-89.46
Receiver Noise Figure at Antenna Port [dB]	1.96	2.93
Receiver Temperature [K/dB-K]	280	24.47
Receiver Antenna Temperature [K/dB-K]	290	24.62
System Temperature [K/dB-K]		27.56
System G/T [dB/K]	5.77	
Boltzmann Constant [dBm/K-Hz]	1.38×10^{-23}	-198.60
Noise Spectral Density [dBm/Hz]		-171.04
Receiver Pr/N0 [dB-Hz]		81.57
Data Rate [(bit/s)/(dB-bit/s)]	10×10^{6}	70
Signal BW [(Hz)/dB-Hz]	6000000	67.78
Received Eb/N0 [dB]		11.57502394
Implementation Loss [dB]		1
Required Eb/N0 [dB]		7.5
Margin [dB]		**3.07**

4.3 RF front-end

The simulation of the RF chain is performed in Cadence AWR in the linear domain. The main requirement is to meet the required NF of 2.93 dB. A high-level representation of the system is shown in Figure 4.2. As the antenna is designed to have a differential feed, the input of the system requires a balun to convert the signal to single-ended mode. Devices operating in single-ended mode are less expensive and plentifully available in the market, making project logistics more straightforward. Also, the balun is placed on the PCB, which allows for better control over noise on the traces. This choice is reasonable since the noise immunity of the

differential pair is most beneficial for the long cable run from the antenna. Besides the loss inserted by the balun, the attenuation of the transmission line is also taken into account. The balun IC used is the *LDB181G7BAAEA045* from Murata. The performance of the balun is shown in Figure 4.3.

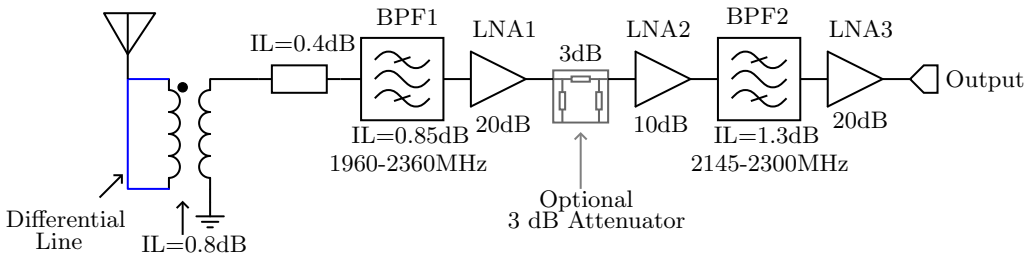

Figure 4.2: RF front-end receiver block diagram.

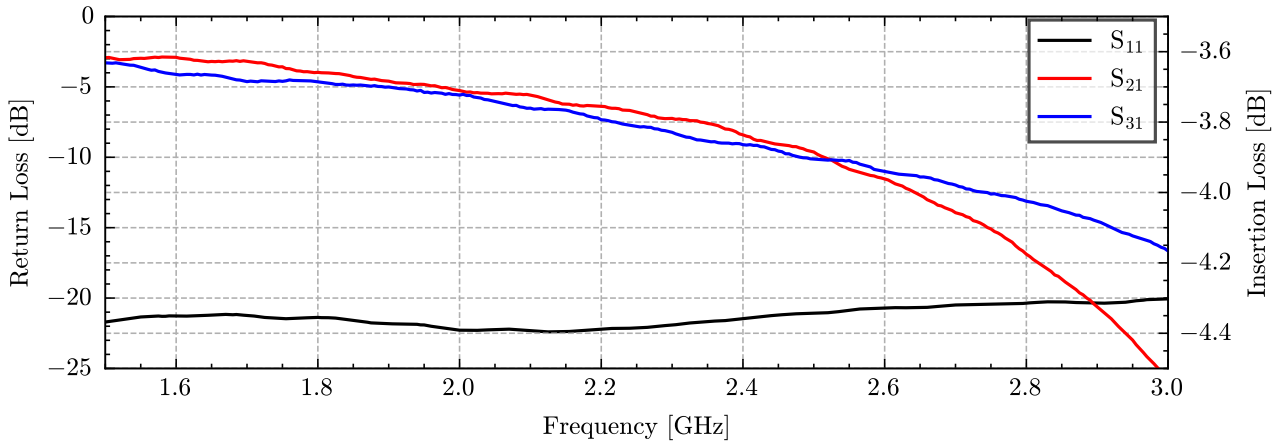

Figure 4.3: Balun S-parameters characterization.

Following the RF chain, a Band-Pass Filter (BPF) is also employed before the first Low-Noise Amplifier (LNA) for initial filtering of undesired signals. If signals outside the band of interest fall within the LNA instability region, the device may begin to oscillate. Therefore, a small filter with fewer poles is employed to minimize insertion loss. For this purpose, the Kyocera AVX *BP0805A2160ASTR* is used, which has an 0805 package and presents a maximum insertion loss of 0.85 dB in the band between 1960 MHz and 2360 MHz.

The first stage (LNA1) has two candidates for performance and implementation evaluation: the Skyworks *SKY67151* and the Qorvo *QPL9065*. The respective evaluation boards were acquired in order to perform the initial RF performance tests. The noise figure (NF) and gain graphs are shown in Figures 4.5a and 4.5b and were extracted through the Y-factor measurement using the Keysight N9020B Signal Analyzer and an N4002A noise source, as shown in the setup of Figure 4.4. For the Qorvo LNA, there are two traces since the device has two gain steps (low gain and high gain) configured externally by a digital interface. The Skyworks IC performs better in terms of noise figure, remaining below 0.35 dB in the analyzed band, while

the Qorvo IC remains around 0.75 dB. The SKY67151 gain also performs inside the informed value by the manufacturer datasheet (20 dB), while the Qorvo has a gain around 37.5 dB in high-gain mode and 17.5 dB in a low-gain mode.

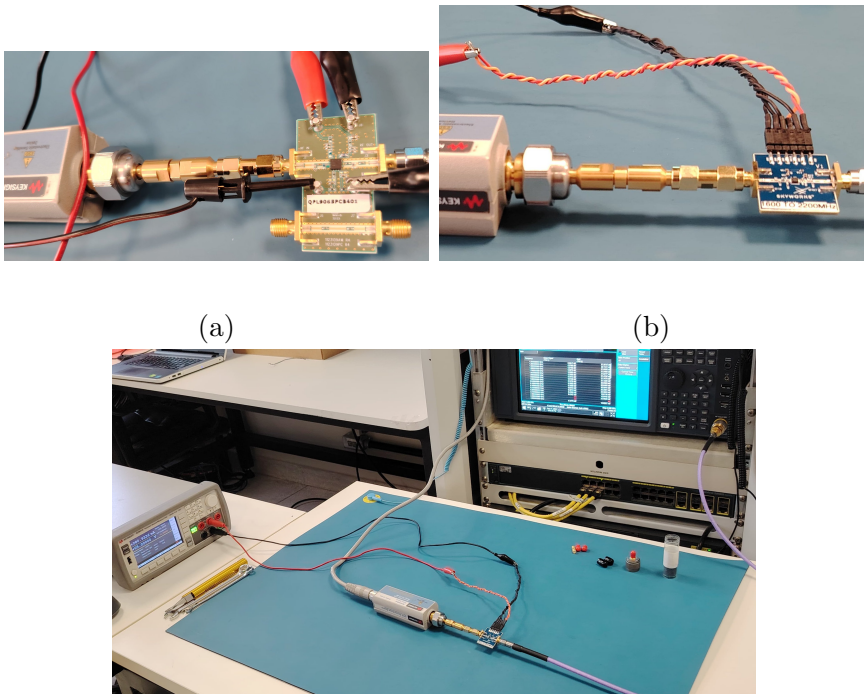

(a) (b)

(c)

Figure 4.4: Images for the LNA evaluation boards (a) Qorvo QPL9065 and (b)Skyworks SKY67151, and (c) is the testing setup for the Y-factor measurement.

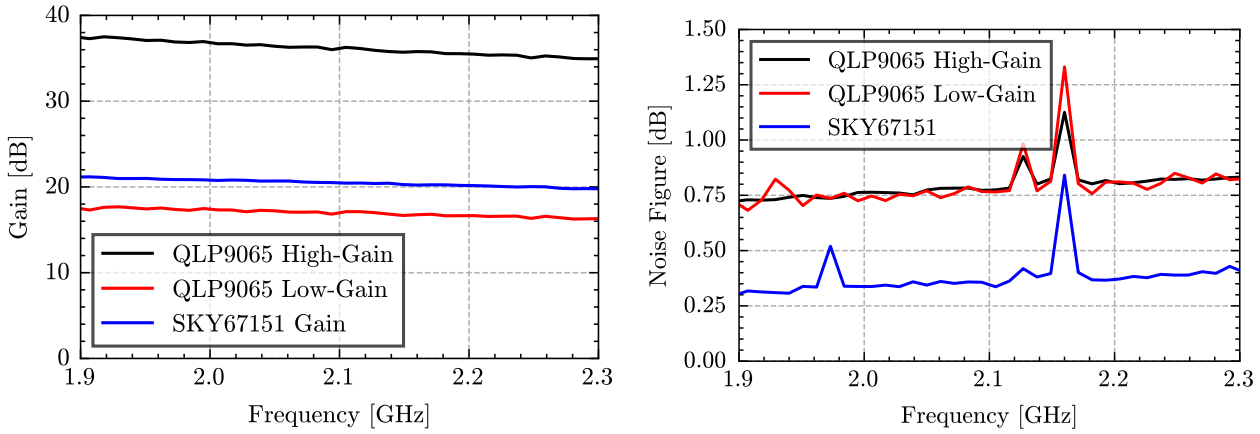

(a) (b)

Figure 4.5: Performance characterization for LNA (a) gain and (b) noise figure. As the QLP9065 have two gain steps, the circuit is characterized twice.

Between the candidates, the Skyworks SKY67151 is chosen due to its simplicity of implementation, since the *QPL9065* requires digital components to choose between the gain steps.

Furthermore, the noise figure for the Skyworks IC has a better performance than the datasheet indicates: 0.35 dB compared to the 0.5 dB provided by the manufacturer, even with a very simple evaluation board.

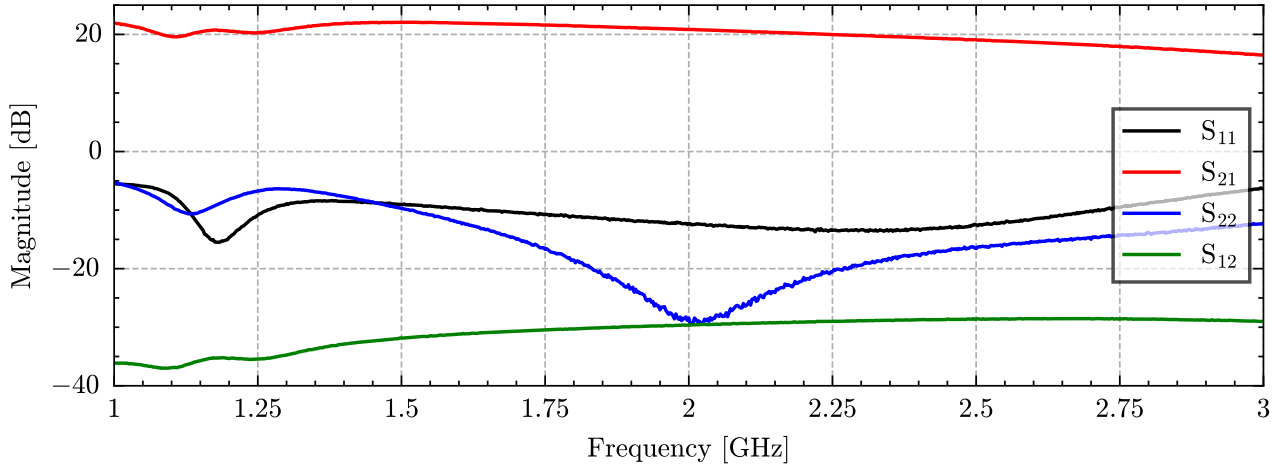

Figure 4.6: S-parameters characterization of the SKY67151 LNA.

Fortunately, the semiconductor industries are equipping new integrated circuits with pre-tuning networks, which dispenses with the usual hard work of tuning steps as when used an isolated transistor as the active element. Figure 4.6 shows the S-parameters from the SKY67151 LNA, extracted using the Keysight P5024B Streamline Vector Network Analyzer.

Table 4.2: RF specification of the active elements of the RF chain.

RF Specs.	**Sym.**	SKY67151-396LF			MAAL-010200			SKY65017-70LF		
		Min	**Typ**	**Max**	**Min**	**Typ**	**Max**	**Min**	**Typ**	**Max**
Noise Figure	NF [dB]		0,5	0,65		1.4	2		4.5	5
Gain	$\|S_{21}\|$ [dB]	17,5	19		10	11	13	19	20	22
Input return loss	$\|S_{11}\|$ [dB]		11			11			24	
Output return loss	$\|S_{22}\|$ [dB]		20			22			25	
Reverse isolation	$\|S_{12}\|$ [dB]		28						23	
3rd order intercept point	OIP3 [dBm]	33	36			36		32	33	
1 dB compress. point	OP1dB [dBm]	18	19,7			17.5		19	20	

The evaluation of the amplifiers follows three main parameters: stability, noise figure and non-linearity performance. Stability ensures that the amplifier does not operate in a positive feedback regime. Therefore, the LNA2 from the Figure 4.1 is followed by an PI attenuator whose purpose is to help in the impedance matching between the two first stage LNAs and provide a degree of isolation between them. Notice that this component is optional and should

only be used if the two amplifiers enter in resonance mode, leading to saturation. The model employed is the Macom MAAL-010200.

The third stage amplifier is focused on high linearity since it handles higher power level at its input. Also, a filter is inserted before this amplifier to filter out the harmonics produced by the first and second LNAs. For this purpose, this filter must be more selective around the central frequency. The third LNA model is the SKY67151 from Skyworks. The RF specification of all the system LNAs are listed in Table 4.2.

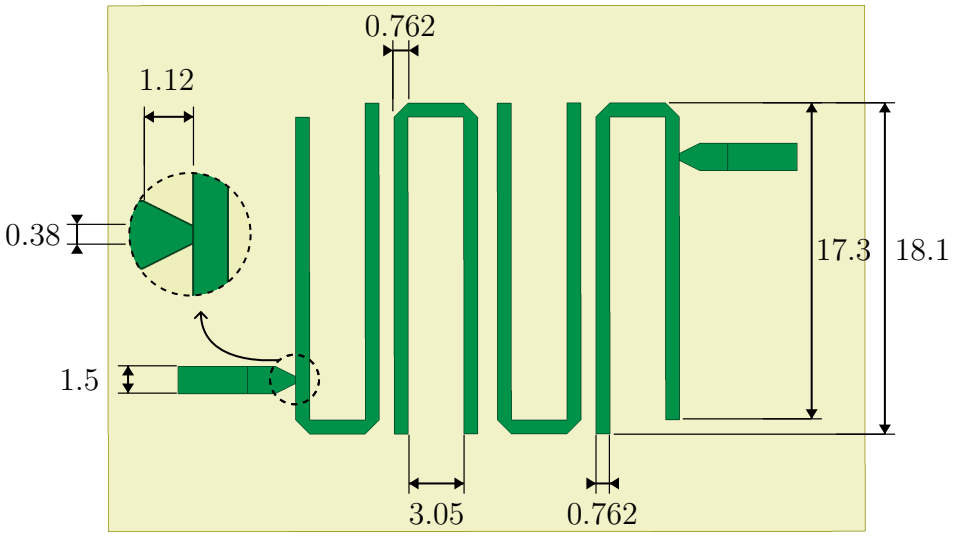

Figure 4.7: Dimensions in [mm] of the Chebyschev Hairpin Filter.

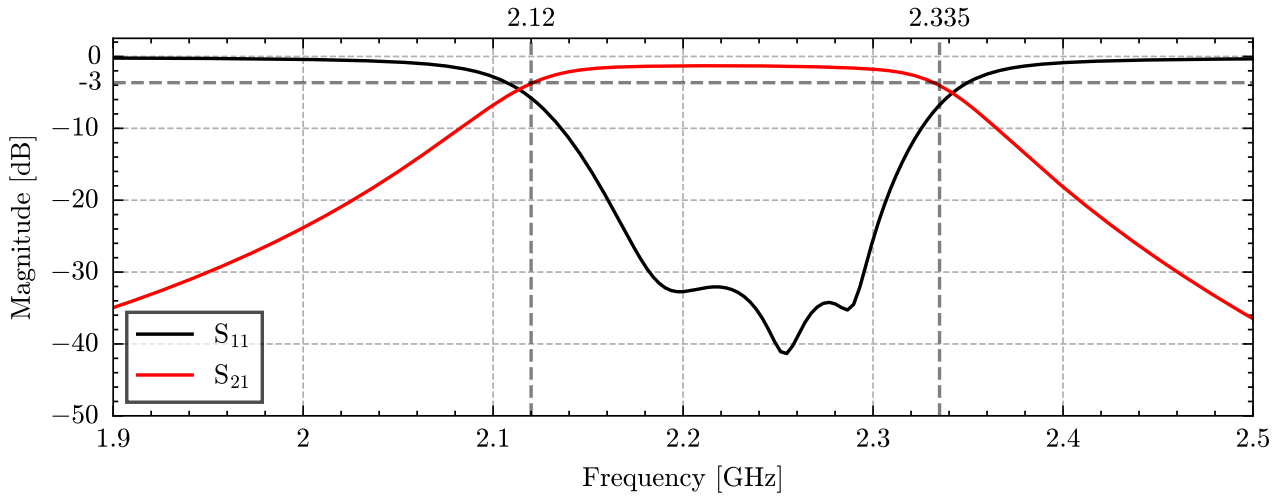

Figure 4.8: Frequency response of the 4th order hairpin filter.

The second band-pass filter (BPF2) is a 4th-order Chebyshev hairpin filter [10] with the dimensions shown in Figure 4.7. This filter is chosen specifically due its reduced length which enables the use of a high-order filter with low losses. The Figure 4.8 shows the filter performance. A return loss below −15 dB and a transmission loss of −1.3 dB were achieved in the frequency range of 2.145 GHz and 2.3 GHz. The low stop-band is around 2.02 GHz and the high stop-band

is around 2.4 GHz considering a stop band value of −20 dB. The group delay and phase for this circuit are observed in Figure 4.9; due to the Chebyshev architecture, it has two points of peak group delay, but there is a nearly constant region at the center of the band.

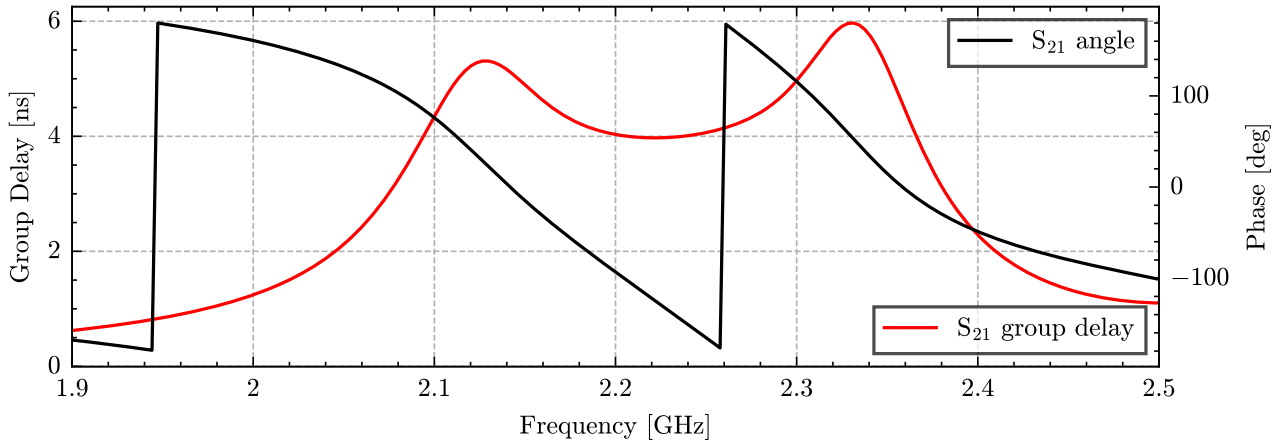

Figure 4.9: Group delay and phase behavior as a function of the frequency for the 4th order hairpin filter.

The SDR at the end of the RF chain uses an AD9363 RF-transceiver. The receiver characteristics of this transceiver is listed in Table 4.3. In this context, the main electrical parameters requested are the maximum receiver NF and the Third-Order Input Intercept Point (IIP3).

The noise figure performance of the AD9363 in this system is not a critical parameter since due to its small contribution to the overall system noise figure. The third order interception point is the most critical, since third-order harmonics are next to the central frequency, and in this transceiver, it is defined as the IIP3 parameter. This parameter indicates the maximum power at the input before the amplifiers enter a non-linear regime and start to distort the signals. To avoid such a region of operation, a maximum input power of −34 dB is established, which is 20 dB below the IIP3 value and therefore will keep the third-order harmonics at least 60 dB below the fundamental tone.

Table 4.3: Electric parameters of the AD9363 transceiver operating at 2.4 GHz.

Parameter	**Symbol**	**Min.**	**Typ.**	**Max.**	**Unit**	**Test Conditions/ Comments**
Noise Figure	NF		3		dB	Maximum Rx gain
Third-Order Input Intermodulation Intercept Point	IIP3		-14		dBm	Maximum Rx gain
Local Oscillator (LO) Leakage Quadrature			-110		dBm	At Rx front-end input
Gain Error			0.2		%	
Phase Error			0.2		Degrees	
Input Return Loss	S11		-10		dB	

Figure 4.10 shows the performance of the front-end system. Notice that the estimated transmission line losses between the elements described in Figure 4.2 are also included. The final observed noise figure is 2.65 dB, which leads to a signal-to-noise ratio margin of approximately 3.35 dB. The main contributors to the noise increase are the BPF1 filter and the line loss before the LNA1. The output power simulated in Figure 4.10b is −45.8 dB, which is a value well within the dynamic range of the AD9363 transceiver.

The Third-Order Output Intercept Point (OIP3) remains above 30 dB at the end of the chain, and the 1 dB compression point has a value of roughly 20 dBm. Both values are well below the final node power of -45.8 dBm which ensures that the LNAs are operating in a linear region. The linear gain at the output of the circuit is around 43 dB.

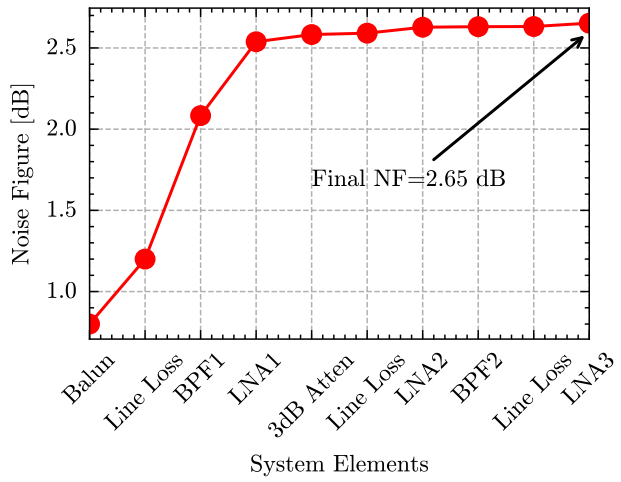

(a) Cascaded noise figure as a function of the system chain elements.

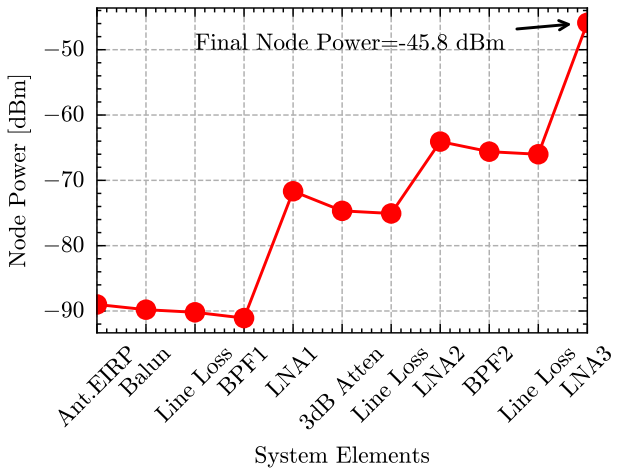

(b) Cascaded signal power as a function of the system chain elements.

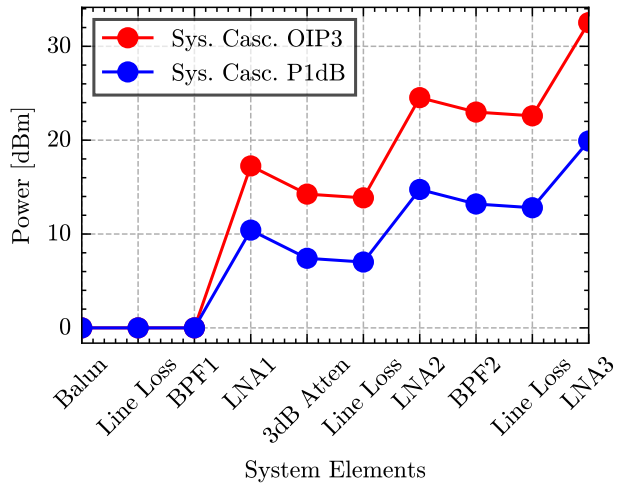

(c) Cascaded Third-Order Output Intercept Point (OIP3) and 1dB Compression Point (P1dB) as a function of the system chain elements.

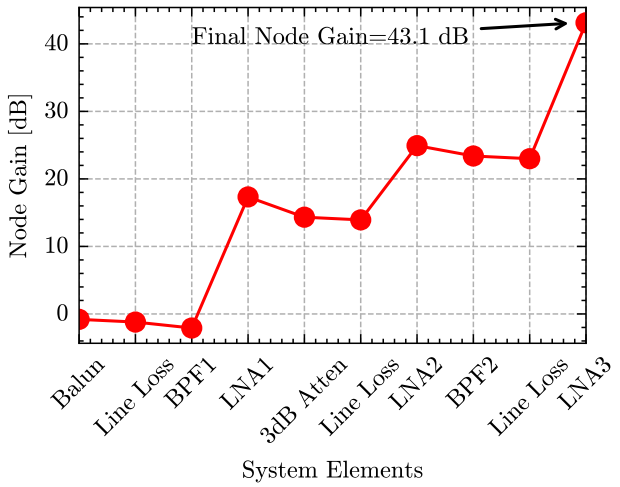

(d) Cascaded linear gain over the system chain elements.

Figure 4.10: System-level simulation of the elements shown in Figure 4.2, including implementation losses.

4.4 Software Defined Radio

The SDR is implemented using the UHD firmware, which is the open source firmware for USRP devices. The ANTSDR E200 uses a derived version of the UHD firmware for B205mini device, with the improvement of using an Ethernet interface.

The advantage of using the UHD firmware is the package of pre-processing and calibration features implemented in the Field-Programmable Gate Array (FPGA). Moreover, as the system requires the use of multiple devices, it includes integrated tools for handling data transport and estimating latency, which accelerates implementation.

As seen in Figure 4.1, the design requires a clock and time synchronization. As such, a GPS Disciplined Oscillator device is used at each antenna to provide the 10 MHz reference clock and the sample timing reference through a Pulse Per Second (PPS) waveform triggered by the received Global Positioning System (GPS) data.

Other methods of synchronization are possible, mainly by using a single clock reference and then distributing it through coaxial cables. This method ensures that all the devices are synchronized using a master and stable clock. The main disadvantage of this method is the use of a pair of coaxial cables for the synchronization signals. For phased array with large distances, the cable length must be compensated physically to ensure that all the signals arrive at the receiver with the same phase. Furthermore, the phase stability of coaxial cables is sensitive to room temperature changes, leading to phase mismatching in synchronization systems, as well discussed in [3] and [24]. Therefore, the distributed and standalone solution as the GPSDO is the most conservative approach.

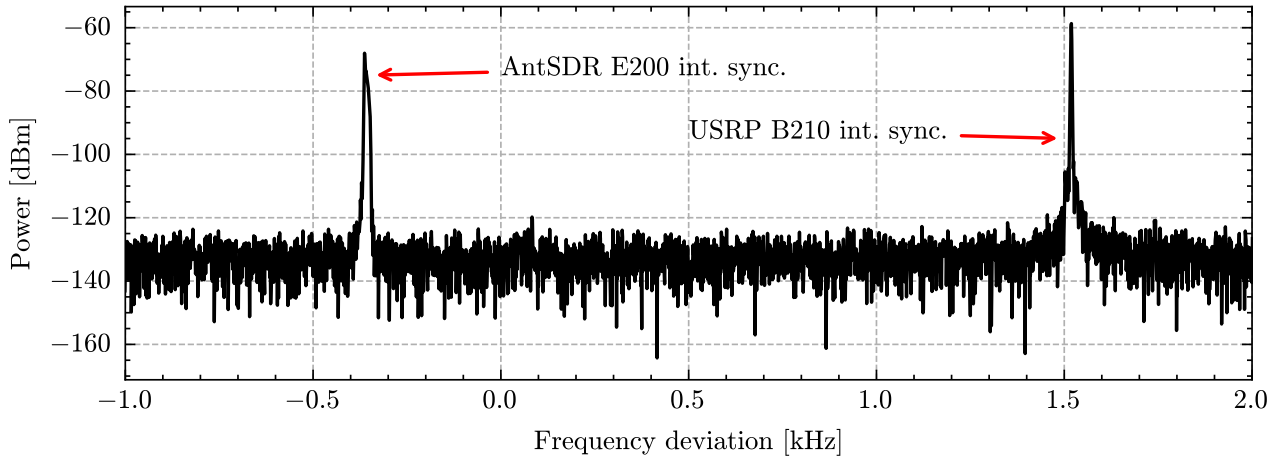

Figure 4.11: USRP B210 and ANTSDR E200 with internal frequency clock reference.

In Figure 4.11, a single frequency tone centered at 1 GHz provided by the ANTSDR E200 and the USRP B210 is shown. The B210 device is used just for the sake of comparison since it is a high-performance (and consequently more expensive) device. The measurement is made with the Keysight B2901B Signal Analyzer with IF bandwidth of 1 Hz. Both SDRs are unsynchronized, and in this configuration, it is possible to see the frequency deviation caused by

their internal reference clocks. For the ANTSDR E200, the frequency exhibits a deviation of 0.35 kHz, while the USRP B210 presents a deviation of approximately 65 kHz. However, this deviation value changes every time the SDRs are restarted, leading to an unpredictable state. This work does not aim to quantify this kind of deviation, but rather to correct it through reference clock synchronization.

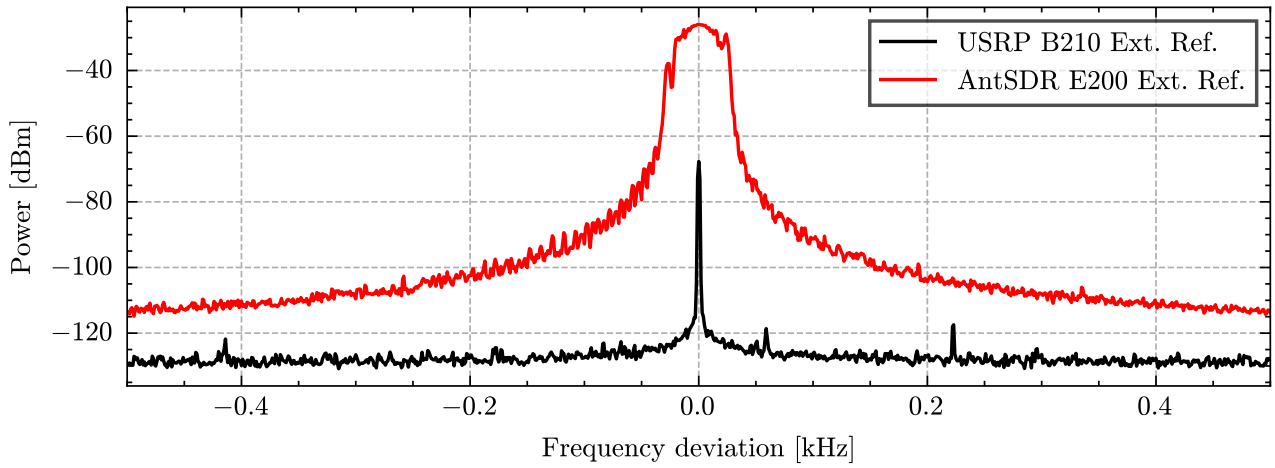

Figure 4.12: USRP B210 and ANTSDR E200 synchronized with an external reference provided by the Keysight N9020B Signal Analyzer.

Both SDRs are now synchronized with the same 10 MHz reference clock provided by the Signal Analyzer and the center frequency deviation over time is shown in Figure 4.12. To capture the frequency hopping values, the maximum hold function of the spectrum analyzer is used. Note that the USRP B210 has a deviation of 1 ppb from the central frequency, while the ANTSDR E200 has a deviation of 50 ppb. Compared to the satellite signal bandwidth of 6 MHz, the variation of 50 Hz can be corrected through digital PLL algorithms. The most important result is that both SDRs are centered at the same frequency of 1 GHz.

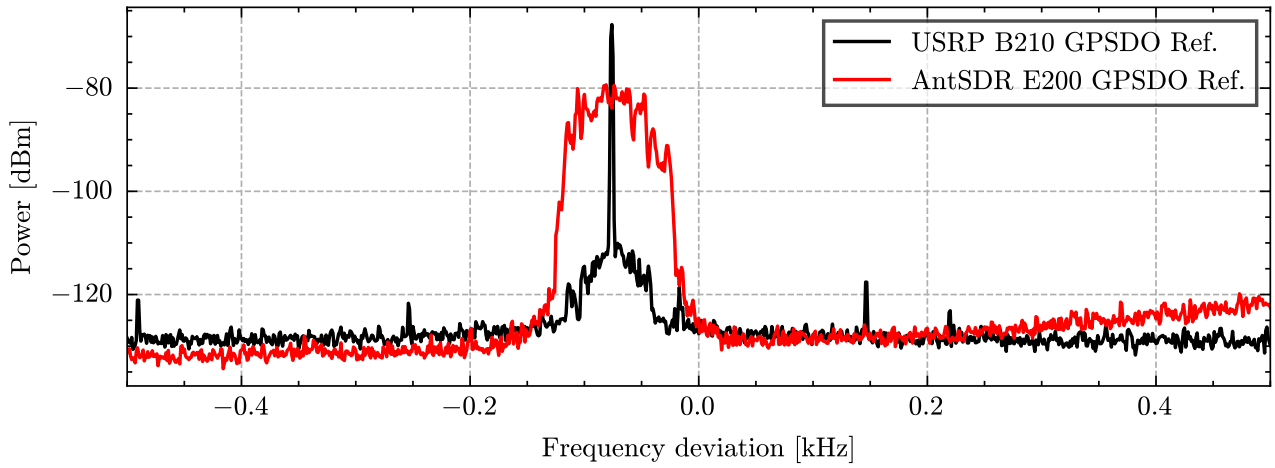

Figure 4.13: USRP B210 and ANTSDR E200 synchronized with GPSDO reference clock.

Finally, SDRs are tested, each synchronized with different GPSDO clock reference. The

measured offset from central frequency is −76 Hz from central frequency for both SDRs. The offset remains fixed throughout the entire test, which indicates a fixed and quantifiable variation across all units. Such deviation can be corrected by shifting the central frequency by the offset amount. A dynamic central frequency variation of approximately 100 ppb is observed for the ANTSDR, while for the USRP is around 5ppb.

The comparison between the ANTSDR E200 and USRP B210 with unsynchronized clock, synchronized with the Signal Analyzer 10 MHz reference, and with the GPSDO is summarized in Table 4.4.

Table 4.4: Comparison between the synchronization performance for ANTSDR E200 and USRP B210.

Parameter	ANTSDR E200 Reference			USRP B210 Reference		
	Int.	Ext.	GPSDO	Int.	Ext.	GPSDO
Dyn. offset variation [ppb]	Undefined	50	100	Undefined	1	3
Freq. offset [Hz]	Undefined	0	-76	Undefined	0	-76

Chapter 5

Array Calibration

Once mounted, the array's positioning can deviate from the ideal due to the factors such as soil erosion and structural degradation. As shown in [6], even small positioning errors can result in inaccurate array steering and erroneous signal Direction-of-Arrival (DoA).

The RF front-end suffers from non-idealities, introducing variations in signal amplification and phase. Key sources include gain and phase imbalances, IQ imbalances in receivers (generally small), internal system leakages, and quantization errors in phase shifters, attenuators, and Analog-to-Digital Converters (ADCs). Additional errors may arise from antenna mutual coupling and near-field scattering.

Array calibration mitigates these errors. Most studies focus on mitigating mutual coupling, as summarized in [26], [28] and [32]. However, as shown in Fig. 1.1, the array elements are spaced far apart, and the antennas are highly directive, minimizing mutual coupling effects enough to a negligible level.

Calibration of gain and phase imbalances employs various techniques. For example, [44] generates the calibration matrix, which depends from the direction of arrival, by using a fine grid of calibration points, while [48] reduces the number of calibration grid points but still requires 3°-step polar grid. Though effective, this grid-based method of calibration is impractical for arrays without dense calibration points that are performed usually in an anechoic chamber.

A successful subspace approach in radio astronomy applications involves pointing antennas at a signal source and subtracting the signal covariance matrix from the noise covariance matrix [19], [15]. Other methods use a known modulated signal to analyze calibration with biased and unbiased array errors [5], [8]. This article exploits a simulation of the rectangular antenna array architecture of Fig. 1.1 with known two points of calibration pilots using a least squares solution to find the parameters errors from the array.

This chapter is organized as follows: Section 5.1 specifies the mathematical model for the rectangular uniform array employed. Section 5.2 presents the calibration method, including position and amplitude and phase calibration based on [5] and [8]. Section 5.3 discusses the simulation results.

5.1 System Model

The array consists of $M = 16$ parabolic antennas, each with a diameter of 2.4 m, distributed uniformly in a rectangular configuration with spacings $d_x = 6\,\text{m}$ and $d_y = 12.66\,\text{m}$, as shown in Fig. 5.1. The array response to incoming signals from different directions is modeled as follows:

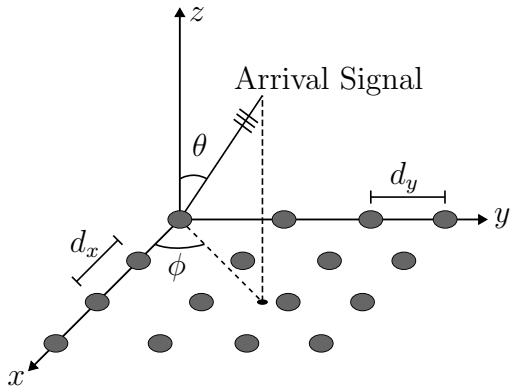

Figure 5.1: Antenna array coordinate system and its layout.

$$\mathbf{X} = \mathbf{HS} + \mathbf{N}, \tag{5.1}$$

where $\mathbf{X} \in \mathbb{C}^{M\times L}$ is the matrix of received antenna signals, $\mathbf{H} \in \mathbb{C}^{M\times D}$ is the channel matrix, $\mathbf{S} \in \mathbb{C}^{D\times L}$ is the signal vector, $\mathbf{N} \in \mathbb{C}^{M\times L}$ is the additive gaussian noise, and L is the number of signal samples.

The channel matrix $\mathbf{H}$ models the initial phase, amplitude and fixed channel difference between antennas for each arriving signal, as follows:

$$\mathbf{H} = [\mathbf{h}_1 \dots \mathbf{h}_D], \tag{5.2}$$

where $\mathbf{h_i} \in \mathbb{C}^{M\times 1}$ models the array behavior for each incoming signal and D is the number of incoming signals.

Each $\mathbf{h_i}$ is a Kronecker product of the Steering Vectors $\mathbf{a}(v_i)$ and $\mathbf{a}(u_i)$ at directions $\hat{x}$ and $\hat{y}$, respectively. Furthermore, it is multiplied by the initial phase and amplitude $\beta_i = a_i e^{-j\psi_i}$ and antenna gain at the signal's DoA, as shown in Eq. 5.3.

$$\mathbf{h_i} = \beta_i G(\theta_i, \phi_i)\mathbf{a}(v_i) \otimes \mathbf{a}(u_i). \tag{5.3}$$

The steering vectors are defined as:

$$\begin{cases} \mathbf{a}(u_i) = [1, e^{ju_i} \dots e^{j(M/2-1)u_i}]^T, \\ \mathbf{a}(v_i) = [1, e^{jv_i} \dots e^{j(M/2-1)v_i}]^T, \end{cases} \tag{5.4}$$

$$\begin{cases} u_i = kd_x \sin(\theta_i)\cos(\phi_i),\ i = 1 \dots D \\ v_i = kd_y \sin(\theta_i)\sin(\phi_i),\ i = 1 \dots D \\ k = \frac{2\pi c}{f}, \end{cases} \tag{5.5}$$

where c is the light velocity, f is the signal frequency, ϕ and θ are the elevation and azimuth angles as described in Fig. 5.1.

5.2 Array Calibration

Eq. 5.1 models the behavior of the received antenna signals over an Additive White Gaussian Noise (AWGN) channel with an initial uniform phase and amplitude. This models assumes ideal positioning and an RF front-end free from errors [44]. However, the real array implementations deal with errors that modify each antenna's amplitude and phase, leading to inaccurate array beamforming. This article addresses antenna position estimation and compensation of amplitude and phase imbalances.

The error correction is achieved through the array calibration. Calibration can be global, with one calibration matrix correcting all array directions, or local, with separate matrices for each direction. In this work, global calibration is used, as it requires fewer calibration points, while local calibration requires a dense grid of calibration points [6]. Global calibration is modeled by:

$$\hat{\mathbf{h}}_i = \mathbf{Q}\mathbf{h}_i(\theta_i, \phi_i), \tag{5.6}$$

where $\mathbf{Q} \in \mathbb{C}^{M \times M}$ is the calibration matrix and can be a full matrix, that models the channel and antenna mutual coupling, or a diagonal matrix modeling only the antenna receiving imbalance. Antenna mutual coupling is minimized in this design due the large space between elements and the high directivity of antennas.

5.2.1 Position Correction

Once the parabolic antennas are mounted, their exact positions must be determined to ensure that global calibration primarily corrects amplitude and phase imbalances. This correction method is based on antenna distance measurements.

The ideal position vector is $\mathbf{V} = [\mathbf{v}_1, \mathbf{v}_2 \dots \mathbf{v}_M]$, with each $\mathbf{v}_i = (x_i, y_i)$, $i = 1 \dots M$. The measurement position vector is $\mathbf{M} = \mathbf{V} + \delta$, where $\delta = [\delta_\mathbf{1} \dots \delta_\mathbf{M}]$, $\delta_\mathbf{i} = (\delta_{xi}, \delta_{yi}) \in \mathbb{R}^2$. The goal is to find the measurement error corresponding to ideal position using the Euclidean Distance Matrix in Eq. 5.7 [31].

$$\begin{aligned} M_{ij}^2 &= ||M_j - M_i||^2 \\ &= (x_{ij} + \delta_{xi} - \delta_{xj})^2 + (y_{ij} + \delta_{xi} - \delta_{xj})^2 \\ &= x_{ij}^2 + y_{ij}^2 + 2x_{ij}(\delta_{xi} - \delta_{xj}) + \cdots \\ &+ 2y_{ij}(\delta_{yi} - \delta_{yj}) + (\delta_{xi} - \delta_{xj})^2 + (\delta_{yi} - \delta_{yj})^2, \end{aligned} \tag{5.7}$$

where $x_{ij} = (x_j - x_i)$ and $y_{ij} = (y_j - y_i)$.

Supposing $|\delta_{xi}| \ll x_i$ and $|\delta_{yi}| \ll y_i$ which immediately results in $|\delta_{xj} - \delta_{xi}|^2 \ll |\delta_{xj} - \delta_{xi}| \ll x_{ij}$ and $|\delta_{yj} - \delta_{yi}|^2 \ll |\delta_{yj} - \delta_{yi}| \ll y_{ij}$ it is possible accomplish a linearization of the problem by suppressing the quadratic terms, as described in Eq. 5.8.

$$M_{ij}^2 = x_{ij}^2 + y_{ij}^2 + 2x_{ij}(\delta_{xi} - \delta_{xj}) + 2y_{ij}(\delta_{yi} - \delta_{yj}). \tag{5.8}$$

Since the objective is to find the position error relative to the ideal position, the equation of measured errors can be set up in Eq. 5.9.

$$\Delta_{ij} = M_{ij}^2 - (x_{ij}^2 + y_{ij}^2) = 2x_{ij}(\delta_{xi} - \delta_{xj}) + 2y_{ij}(\delta_{yi} - \delta_{yj}), \tag{5.9}$$

where the left side is known while the right side is estimated in matrix form as in Eq. 5.10.

$$\mathbf{A}\delta = \mathbf{\Delta}, \tag{5.10}$$

where $\mathbf{A} \in \mathbb{R}^{K \times 2M}$, K being the number of measurements, $\boldsymbol{\delta} = [\delta_{x_1} \ldots \delta_{xM}, \delta_{y_1}, \delta_{yM}]^T$, and $\mathbf{\Delta} \in \mathbb{R}^{K \times 1}$. The Eq. 5.10 is written explicitly in Eq. 5.11.

The matrix $\mathbf{A}$ is non-square, so it does no have a direct inverse. If the matrix $rank\{\mathbf{A}\} = min\{K, 2M\}$, the pseudo-inverse matrix can be used as $A^\dagger = (A^H A)^{-1} A^H$.

The solution for estimating position deviations is given by 5.12.

$$\hat{\delta} = (A^H A)^{-1} A^H \mathbf{\Delta} + \alpha \mathbf{I}, \tag{5.12}$$

where $\hat{\delta}$ are the estimated deviation values and α is a regularization constant.

$$\begin{bmatrix} \vdots & \vdots & \vdots & \vdots & \vdots & \vdots & \vdots & \vdots & \vdots \\ \cdots & 2x_{ij} & \cdots & -2x_{ij} & \cdots & 2y_{ij} & \cdots & -2y_{ij} & \cdots \\ \vdots & \vdots & \vdots & \vdots & \vdots & \vdots & \vdots & \vdots & \vdots \end{bmatrix}_{K \times 2M} \cdot \begin{bmatrix} \delta_{x1} \\ \vdots \\ \delta_{xn} \\ \delta_{y1} \\ \vdots \\ \delta_{yn} \end{bmatrix}_{2M \times 1} = \begin{bmatrix} \vdots \\ \Delta_{ij} \\ \vdots \end{bmatrix}_{K \times 1}. \tag{5.11}$$

5.2.2 Phase and Amplitude Correction

After performing initial position calibration using the EDM, the remaining errors are primarily in phase and amplitude. The steering vector now depends on antenna error parameters, $\boldsymbol{\rho} \in \mathbb{C}^{M\times 1}$, as

$$\mathbf{h}_i(\boldsymbol{\rho}) = \beta_i \boldsymbol{\rho} \odot (\mathbf{a}_i(v_i) \otimes \mathbf{a}_i(u_i)), \tag{5.13}$$

where $\odot$ is the Hadamard product. Though other errors parameters could be considered, this work focuses on phase and amplitude. These parametric errors are assumed independent of the signal DoA.

When sources at known physical positions emit also known signals, the steering vector can be estimated as

$$\hat{\mathbf{h}}_c = \frac{\mathbf{X_c}\mathbf{S}^H}{||\mathbf{S}||_F^2},\ c = 1 \dots C, \tag{5.14}$$

where C is the number of sources positions. The perturbation parameters are determined by least-squares approach:

$$\hat{\boldsymbol{\rho}} = \text{argmin}_\rho ||\hat{\mathbf{h}}_\mathbf{c} - \mathbf{h}_c(\boldsymbol{\rho})||_F^2. \tag{5.15}$$

Consequently, the global calibration matrix $\mathbf{Q}$ assumes the form:

$$\mathbf{Q} = \text{diag}(\hat{\boldsymbol{\rho}}), \tag{5.16}$$

because the calibration matrix only consider the channel effects and the mutual coupling is neglected.

5.3 Simulation Results

The first calibration performed is the position calibration. To simulate, an ideal EDM matrix with perturbed noise is generated. To examine bias effects, colored noise (white, pink, and blue) is also used to evaluate the algorithm under a biased and unbiased perturbation. Pink noise and blue noise are a white noise after passing a high-pass filter and a low-pass filter, respectively. The average Root Mean Square Error (RMSE) for various noise types and standard deviations (in meters) is presented in Fig. 5.2. At standard deviation of 0.2 m, the estimated error is approximately 0.25 %, which is a reasonable performance for signals operating in S-band. Fig. 5.3 demonstrates the correction.

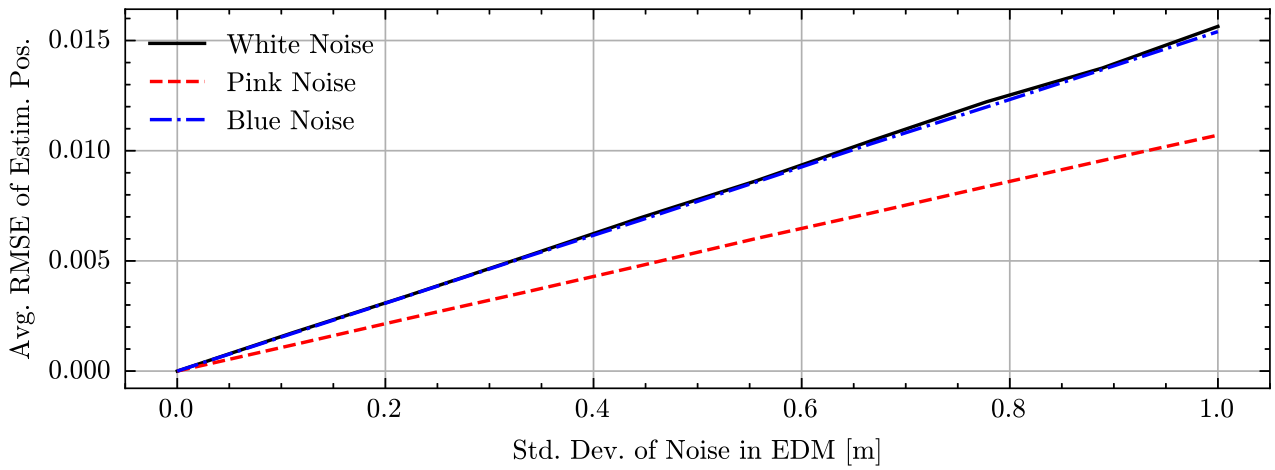

Figure 5.2: Performance evaluation of position correction algorithms over variations in noise standard deviation in EDM.

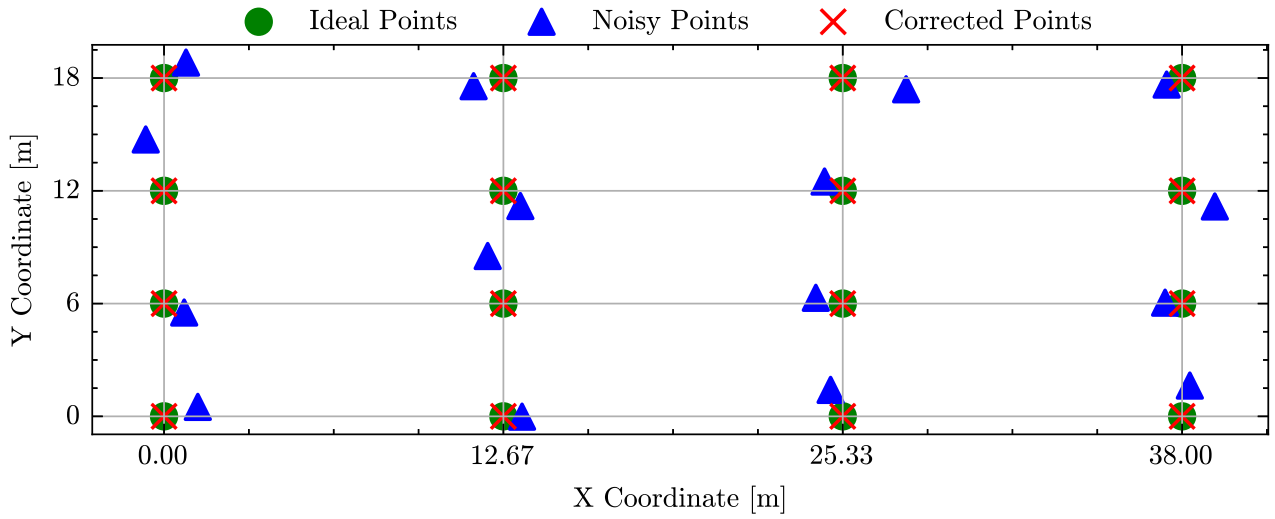

Figure 5.3: Position estimation after applying noise with 1 m of standard deviation.

The array phase and amplitude calibration are evaluated using all 16 antennas, following the distances and specifications in Sec. 5.1. It is also used two pilot signals at a signal-to-noise ratio (SNR) of 20 dB to perform the calibration benchmark. The perturbation is focused in the signal phase and amplitude.

For perturbations independent of the signal's DoA, the result are shown in Fig. 5.4. The averaged RMSE between the calibrated and ideal steering vector achieves a reasonable performance below a standard deviation of 0.1. Once the array is fixed and steered synchronously, the perturbation is not highly direction-dependent.

Finally, for array calibration independent of DoA, Fig. 5.5 shows that the presented method (Section 5.2.2) achieves a maximum averaged RMSE of −33 dB (approximatelly 0.005 %).

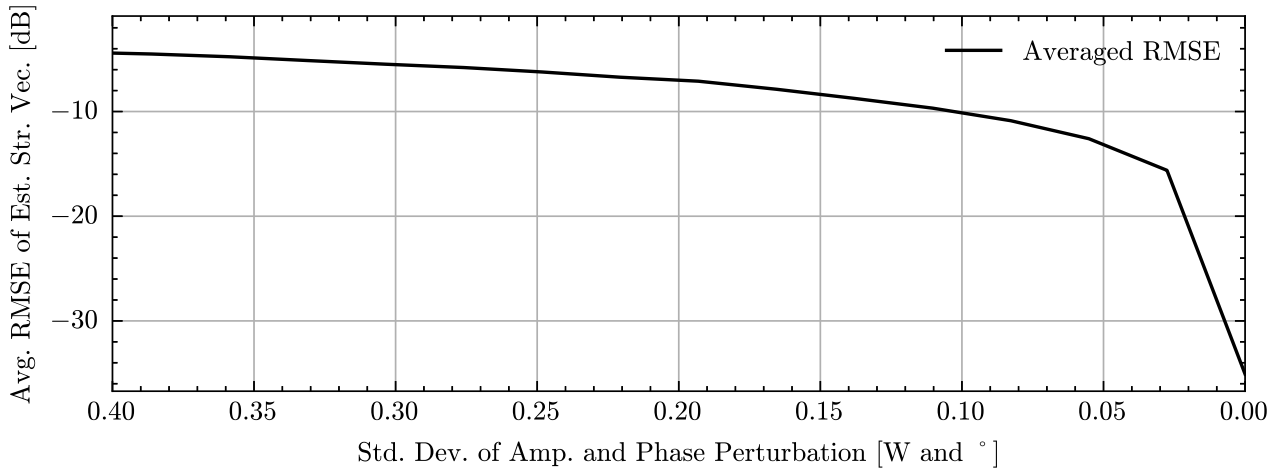

Figure 5.4: Averaged RMSE between estimated and real steering vectors under direction-independent perturbations. Deviation perturbations applied uniformly to the relative amplitude and phase.

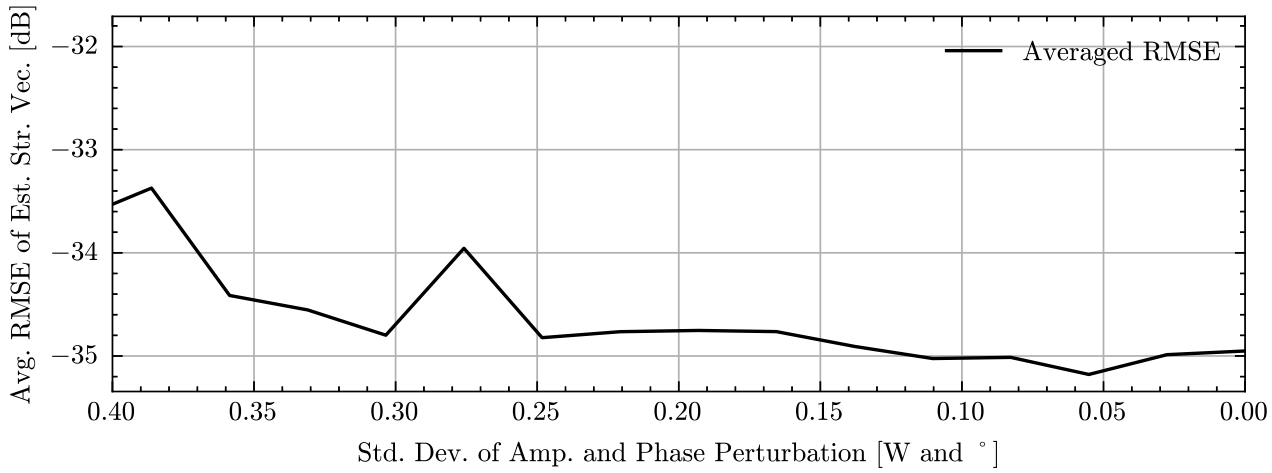

Figure 5.5: Averaged RMSE between estimated and real steering vector direction-independent perturbations. Deviation perturbations applied uniformly to the relative amplitude and phase.

Chapter 6

Conclusion

This dissertation detailed the development of a low-cost, reconfigurable phased array ground station for tracking LEO satellites, focusing on the design and validation of its core components. Firstly was designed of a high-performance, dual-polarized feed horn. An initial square quad-ridge prototype revealed significant manufacturing and performance challenges, leading to the design of a novel, compact conical horn. This second iteration incorporated a modular assembly, a quadraxial feed, and an innovative tuning mechanism that successfully relaxed manufacturing tolerances. The final conical horn was fabricated and validated through measurements, achieving a 63% fractional bandwidth and a 10.1 dBi peak gain.

The complete system architecture was designed around standalone Software-Defined Radios (SDRs) and custom RF front-ends for each antenna, with synchronization achieved via distributed GPS Disciplined Oscillators (GPSDOs). The effectiveness of this synchronization scheme was experimentally verified, demonstrating its capability to maintain time and clock synchronization across the large array. The link budget analysis verified the system viability the link with the VCUB1 satellite with a link margin of over 3 dB.

To address the mechanical and electronic implementation deviations in terms of positioning and imbalance of amplitude and phase, a two-stage calibration methodology was developed and validated through simulation. The first stage corrects for physical antenna position errors using a practical method based on antenna euclidean distance measurements. The second stage then calibrates the gain and phase imbalances of each RF chain using a minimal number of pilot signals. Simulations confirmed that these algorithms can accurately compensate for array errors. Collectively, this work provides a comprehensive and validation, from hardware fabrication and system architecture to phased array calibration algorithms, for the successful implementation of the proposed LEO satellite ground station.

This project is granting by the Brazilian National Council of Research and Technology (CNPq) with title *Estação Terrena Autônoma Distribuída de Baixo Custo e Alta Taxa de Download*, N. 405635/2022-2, 20/2022 - Faixa A.

Future works

The immediate next steps will focus on transitioning the validated components of this research into a fully operational system. In the electronic and mechanical domains, this involves

fabricating the custom RF front-end board designed in this work and completing the motor control system for automated satellite tracking. Concurrently, in the software domain, the SDR data acquisition modules must be integrated with the main base station control software to create a unified operational platform.

Publications

1. F. R. Sobrinho, E. R. Bortolotto, G. W. S. De Mendonça, H. Silva, and S. R. M. J. Rondineau, "Low-Cost Tunable Compact and Modular Broadband Dual-Polarization Conical Horn Antenna", Submitted to IEEE Antennas and Wirelles Propagation Letters.

2. F. R. Sobrinho, G. W. S. De Mendonça, D. C. Araújo, E. R. Bortolotto and S. R. M. J. Rondineau, "Parabolic Antenna Array Position Estimation and Calibration Techniques," 2024 Workshop on Communication Networks and Power Systems (WCNPS), Brasilia, Brazil, 2024, pp. 1-5, doi: 10.1109/WCNPS65035.2024.10814155.

3. G. W. S. De Mendonça, F. R. Sobrinho, D. C. Araújo, A. Reis and S. R. M. J. Rondineau, "Cross-Protocol Repeater for Sigfox and LoRa Networks Using Cognitive Software Defined Radio Techniques," 2024 Workshop on Communication Networks and Power Systems (WCNPS), Brasilia, Brazil, 2024, pp. 1-5, doi: 10.1109/WCNPS65035.2024.10814198.

Appendix

Appendix A

Quad Ridge PCB Schematics

Revisions	
REV	Description

H - POL

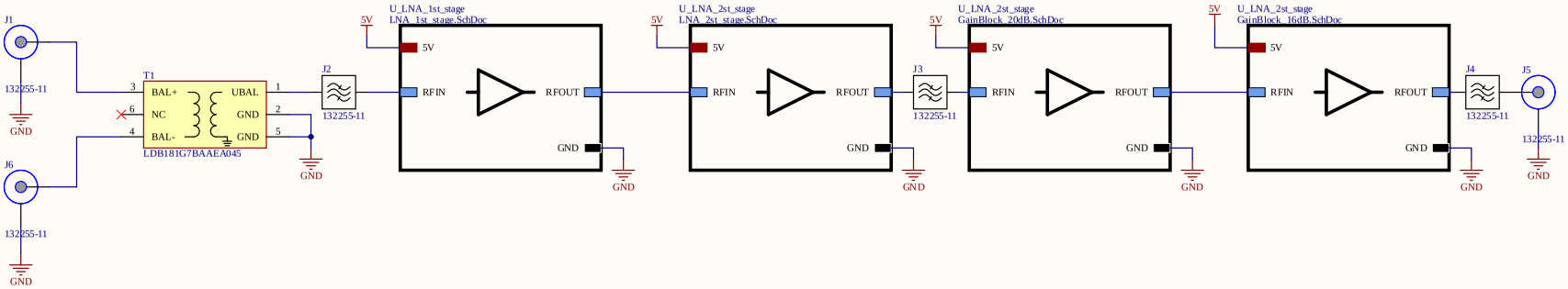

V - POL

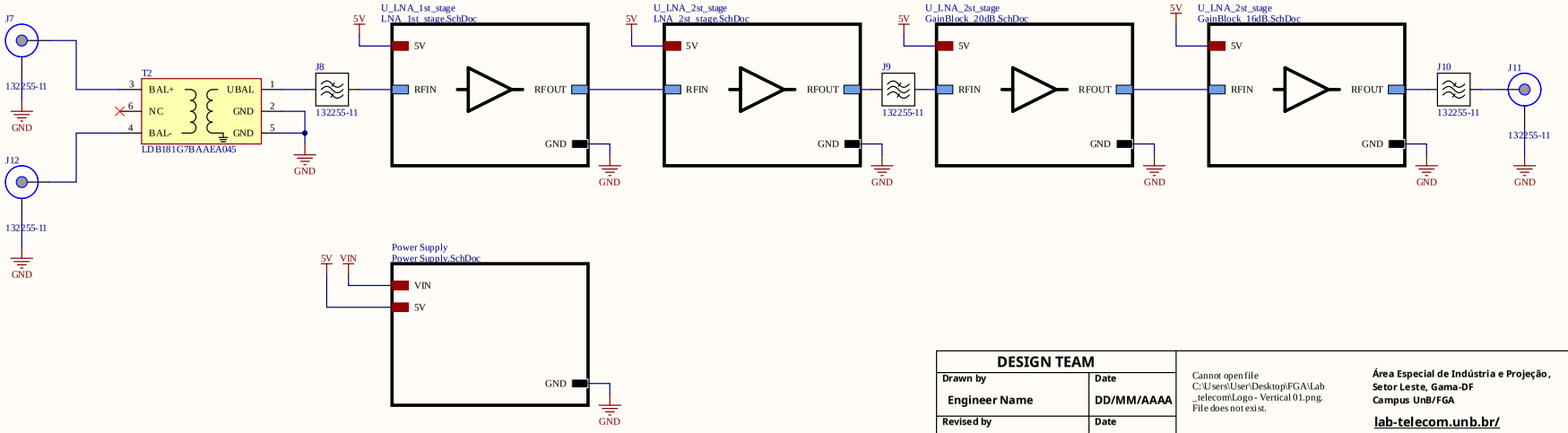

DESIGN TEAM			
Drawn by	Engineer Name	Date	DD/MM/AAAA
Revised by	Revisor Name	Date	DD/MM/AAAA
Verified by	Verifier name		
Technician	Technician Name		
Release date	DD/MM/AAAA		

Cannot open file
C:\Users\User\Desktop\FGA\Lab_telecom\Logo - Vertical 01.png.
File does not exist.

Área Especial de Indústria e Projeção,
Setor Leste, Gama-DF
Campus UnB/FGA
lab-telecom.unb.br/

PUT THE TITLE

Key Words

Size	Document Number	Rev
A3	*.	X.X

Filename	Block Diagram.SchDoc	Sheet 1 of 10

Revisions	
REV	Description

Power Supply

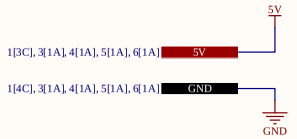

LNA Stage 1

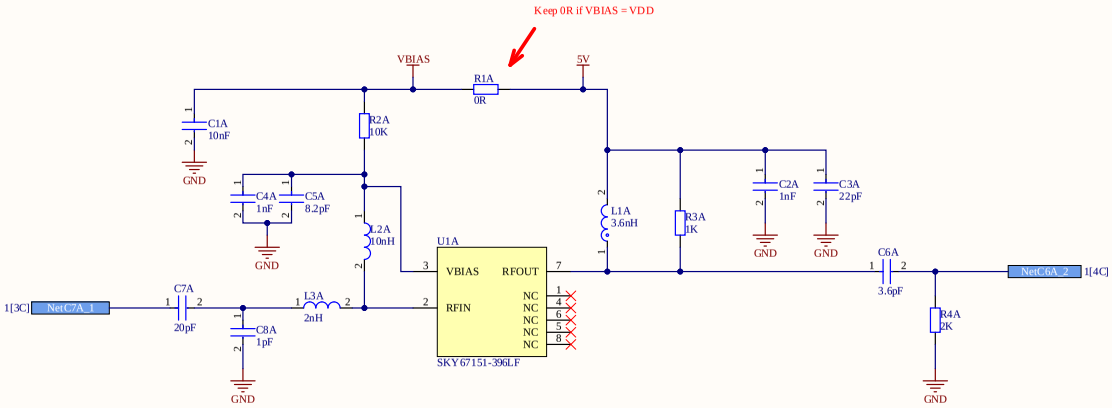

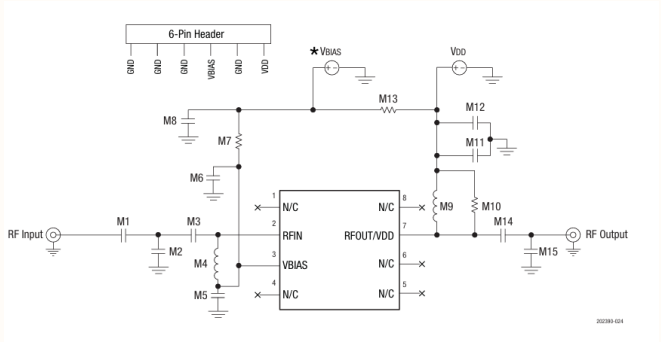

Table 10. SKY67151-396LF Evaluation Board Bill of Materials (1600 to 2200 MHz Tuning)

Component	Description	Value	Size	Manufacturer	Part Number
M1	Capacitor	20 pF	0402	Murata	GJM1555C1H200JB01
M2	Capacitor	1 pF	0402	Murata	GJM1555C1H1R0CB01
M3	Inductor	2 nH	0402	Coilcraft	0402HP-2N0XJL
M4	Inductor	10 nH	0402	Coilcraft	0402HP-10NX_L
M5	Capacitor	8.2 pF	0402	Murata	GJM1555C1H8R2DB01
M6, M12	Capacitor	1000 pF	0402	Murata	GRM155R71H102KA01
M7	Resistor	10 kΩ	0402	Kamaya	RMC1/16S-103JTH
M8	Capacitor	10000 pF	0402	Murata	GRM155R71H103KA88
M9	Inductor	3.6 nH	0402	Murata	LQG15HS3N6S02
M10	Resistor	1 kΩ	0402	Kamaya	RMC1/16S-102JTH
M11	Capacitor	22 pF	0402	Murata	GRM1555C1H220JZ01
M13	Resistor	0 Ω	0402	Kamaya	RMC1/16SJPTH
M14	Capacitor	3.6 pF	0402	Murata	GJM1555C1H3R6CB01
M15	Resistor	2 kΩ	0402	Kamaya	RMC1/16S-202JTH

DESIGN TEAM			
Drawn by	Engineer Name	Date	DD/MM/AAAA
Revised by	Revisor Name	Date	DD/MM/AAAA
Verified by	Verifier name		
Technician	Technician Name		
Release date	DD/MM/AAAA		

Cannot open file C:\Users\User\Desktop\FGA\Lab_telecom\Logo - Vertical 01.png. File does not exist.

Área Especial de Indústria e Projeção, Setor Leste, Gama-DF
Campus UnB/FGA
lab-telecom.unb.br/

PUT THE TITLE

Key Words

Size	Document Number	Rev
A3	*.2	X.X

Filename	LNA_1st_stage.SchDoc	Sheet 2.1 of 10

Revisions	
REV	Description

Power Supply

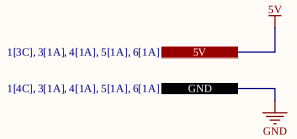

LNA Stage 1

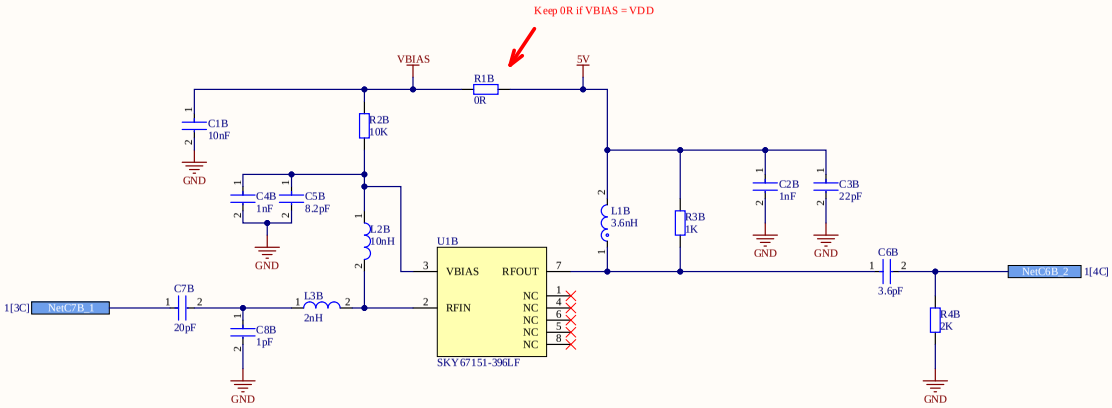

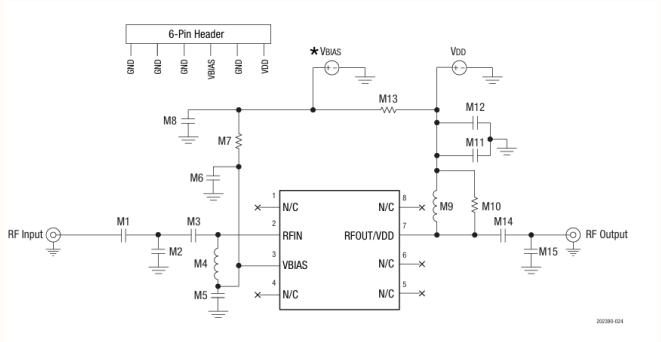

Table 10. SKY67151-396LF Evaluation Board Bill of Materials (1600 to 2200 MHz Tuning)

Component	Description	Value	Size	Manufacturer	Part Number
M1	Capacitor	20 pF	0402	Murata	GJM1555C1H200JB01
M2	Capacitor	1 pF	0402	Murata	GJM1555C1H1R0CB01
M3	Inductor	2 nH	0402	Coilcraft	0402HP-2N0XJL
M4	Inductor	10 nH	0402	Coilcraft	0402HP-10NX_L
M5	Capacitor	8.2 pF	0402	Murata	GJM1555C1H8R2DB01
M6, M12	Capacitor	1000 pF	0402	Murata	GRM155R71H102KA01
M7	Resistor	10 kΩ	0402	Kamaya	RMC1/16S-103JTH
M8	Capacitor	10000 pF	0402	Murata	GRM155R71H103KA88
M9	Inductor	3.6 nH	0402	Murata	LQG15HS3N6S02
M10	Resistor	1 kΩ	0402	Kamaya	RMC1/16S-102JTH
M11	Capacitor	22 pF	0402	Murata	GRM1555C1H220JZ01
M13	Resistor	0 Ω	0402	Kamaya	RMC1/16SJPTH
M14	Capacitor	3.6 pF	0402	Murata	GJM1555C1H3R6CB01
M15	Resistor	2 kΩ	0402	Kamaya	RMC1/16S-202JTH

DESIGN TEAM			
Drawn by	Engineer Name	Date	DD/MM/AAAA
Revised by	Revisor Name	Date	DD/MM/AAAA
Verified by	Verifier name		
Technician	Technician Name		
Release date	DD/MM/AAAA		

Cannot open file C:\Users\User\Desktop\FGA\Lab_telecom\Logo - Vertical 01.png. File does not exist.

Área Especial de Indústria e Projeção, Setor Leste, Gama-DF
Campus UnB/FGA
lab-telecom.unb.br/

PUT THE TITLE

Key Words

Size	Document Number	Rev
A3	*.1	X.X

Filename	LNA_1st_stage.SchDoc	Sheet 2.2 of 10

Revisions	
REV	Description

Power Supply

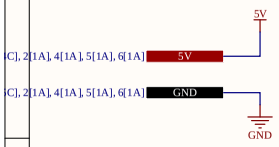

LNA Stage 2

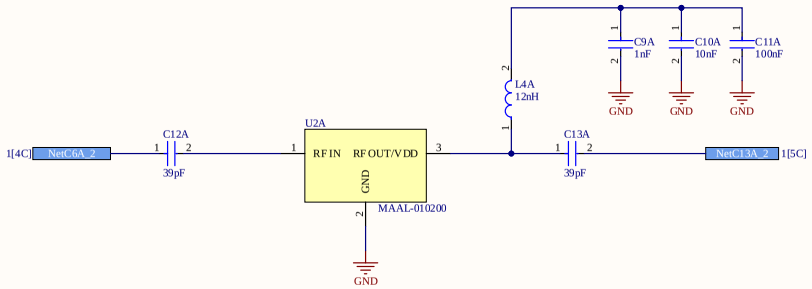

Baseline Application Schematic @ 3V, 5V

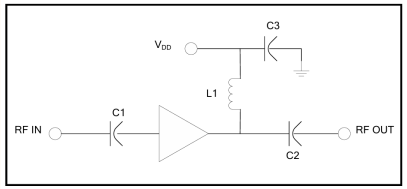

Component List @ 3V, 5V

Part	Value	Case Style	Purpose
C1,C2	39 pF	0402	DC Block
C3	0.1 µF	0402	RF Bypass
L1	12 nH	0402	RF Choke/Tuning

DESIGN TEAM			
Drawn by	Engineer Name	Date	DD/MM/AAAA
Revised by	Revisor Name	Date	DD/MM/AAAA
Verified by	Verifier name		
Technician	Technician Name		
Release date	DD/MM/AAAA		

Cannot open file C:\Users\User\Desktop\FGA\Lab_telecom\Logo - Vertical 01.png. File does not exist.

Área Especial de Indústria e Projeção, Setor Leste, Gama-DF
Campus UnB/FGA
lab-telecom.unb.br/

PUT THE TITLE

Key Words

Size	Document Number	Rev
A3	*.2	X.X

Filename	LNA_2st_stage.SchDoc	Sheet 3.1 of 10

Revisions	
REV	Description

Power Supply

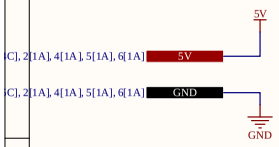

LNA Stage 2

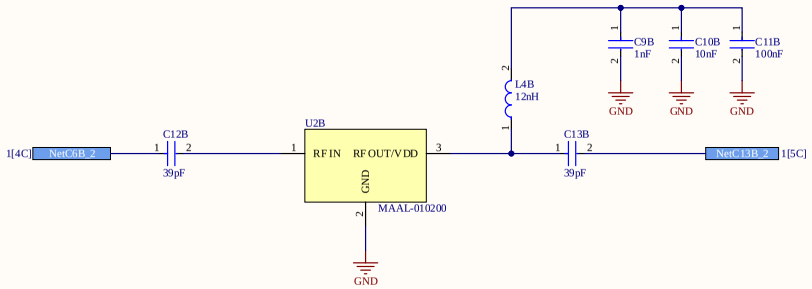

Baseline Application Schematic @ 3V, 5V

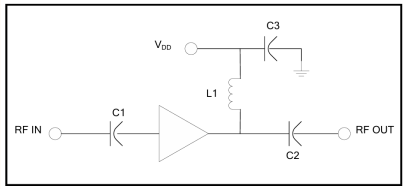

Component List @ 3V, 5V

Part	Value	Case Style	Purpose
C1,C2	39 pF	0402	DC Block
C3	0.1 µF	0402	RF Bypass
L1	12 nH	0402	RF Choke/Tuning

DESIGN TEAM			
Drawn by	Engineer Name	Date	DD/MM/AAAA
Revised by	Revisor Name	Date	DD/MM/AAAA
Verified by	Verifier name		
Technician	Technician Name		
Release date	DD/MM/AAAA		

Cannot open file C:\Users\User\Desktop\FGA\Lab_telecom\Logo - Vertical 01.png. File does not exist.

Área Especial de Indústria e Projeção, Setor Leste, Gama-DF
Campus UnB/FGA
lab-telecom.unb.br/

PUT THE TITLE

Key Words

Size	Document Number	Rev
A3	*.1	X.X

Filename	LNA_2st_stage.SchDoc	Sheet 3.2 of 10

Revisions	
REV	Description

Power Supply

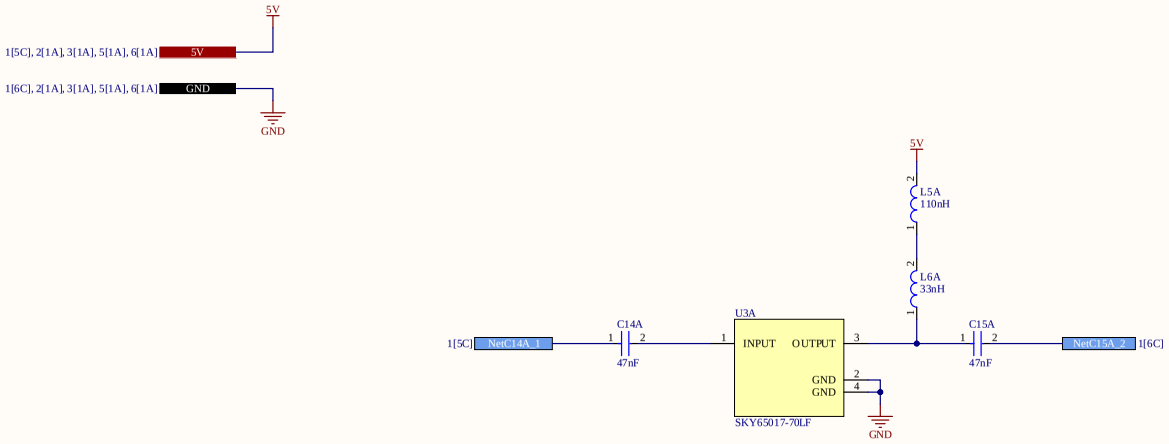

Table 5. Current Limiting Resistor Values

Supply Voltage (V)	Value of R1 (Ω)	Minimum Power Dissipation Rating (mW)
5[1]	0	-
6	10	250
7	20	500
8	30	500
9	40	1000
10	50	1000
12	70	2000

1 To ensure that the supply current does not exceed the recommended value, a regulated current source should be used to supply the device under this condition.

Table 4. SKY65017-70LF Evaluation Board Bill of Materials (BOM)

Component	Value	Size	Part Number	Manufacturer
C1, C2, C4	47 nF	0603	GRM188R71E473K	Murata
L1	33 nH	0603	0603CS-33NX_LU	Coilcraft
L2	1600 Ω	1810	FBMH4525HM162N-T	Taiyo-Yuden
L3	110 nH	0805	0805CS-111X_L	Coilcraft
R1	See Table 5	0603	Variable	Variable

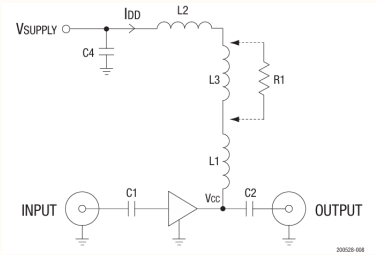

DESIGN TEAM		
Drawn by: Engineer Name	Date: DD/MM/AAAA	
Revised by: Revisor Name	Date: DD/MM/AAAA	
Verified by: Verifier name		
Technician: Technician Name		
Release date: DD/MM/AAAA		

Cannot open file C:\Users\User\Desktop\FGA\Lab_telecom\Logo - Vertical 01.png. File does not exist.

Área Especial de Indústria e Projeção, Setor Leste, Gama-DF
Campus UnB/FGA
lab-telecom.unb.br/

PUT THE TITLE

Key Words

Size	Document Number	Rev
A3	*.2	X.X

Filename	GainBlock_20dB.SchDoc	Sheet 4.1 of 10

Revisions	
REV	Description

Power Supply

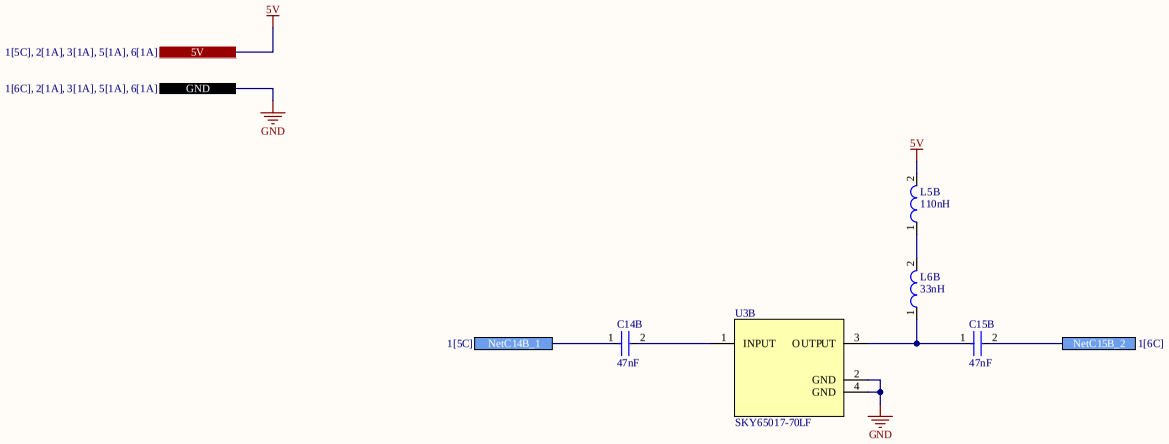

Table 5. Current Limiting Resistor Values

Supply Voltage (V)	Value of R1 (Ω)	Minimum Power Dissipation Rating (mW)
5[1]	0	-
6	10	250
7	20	500
8	30	500
9	40	1000
10	50	1000
12	70	2000

1 To ensure that the supply current does not exceed the recommended value, a regulated current source should be used to supply the device under this condition.

Table 4. SKY65017-70LF Evaluation Board Bill of Materials (BOM)

Component	Value	Size	Part Number	Manufacturer
C1, C2, C4	47 nF	0603	GRM188R71E473K	Murata
L1	33 nH	0603	0603CS-33NX_LU	Coilcraft
L2	1600 Ω	1810	FBMH4525HM162N-T	Taiyo-Yuden
L3	110 nH	0805	0805CS-111X_L	Coilcraft
R1	See Table 5	0603	Variable	Variable

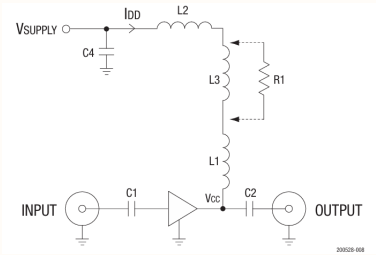

DESIGN TEAM			
Drawn by: Engineer Name	Date: DD/MM/AAAA	Cannot open file C:\Users\User\Desktop\FGA\Lab_telecom\Logo - Vertical 01.png. File does not exist.	Área Especial de Indústria e Projeção, Setor Leste, Gama-DF, Campus UnB/FGA
Revised by: Revisor Name	Date: DD/MM/AAAA		lab-telecom.unb.br/
Verified by: Verifier name		PUT THE TITLE	
Technician: Technician Name		Key Words	
Release date: DD/MM/AAAA		Size: A3	Document Number: *.1	Rev: X.X
		Filename: GainBlock_20dB.SchDoc	Sheet 4.2 of 10

Revisions	
REV	Description

Power Supply

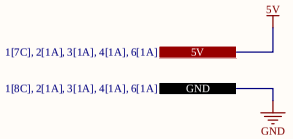

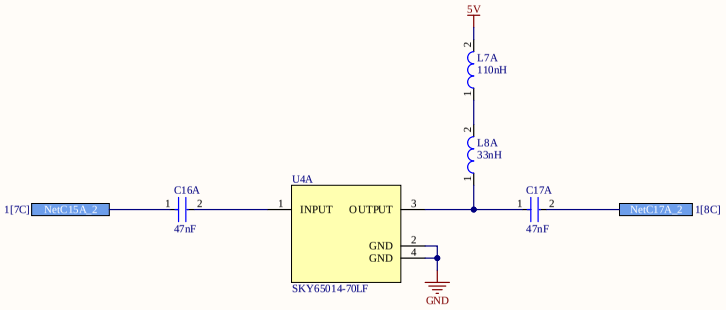

Table 5. Current Limiting Resistor Values

Supply Voltage (V)	Value of R1 (Ω)	Minimum Power Dissipation Rating (mW)
5[1]	0	-
6	10	250
7	20	500
8	30	500
9	40	1000
10	50	1000
12	70	2000

[1] To ensure that the supply current does not exceed the recommended value, a regulated current source should be used to supply the device under this condition.

Table 4. SKY65017-70LF Evaluation Board Bill of Materials (BOM)

Component	Value	Size	Part Number	Manufacturer
C1, C2, C4	47 nF	0603	GRM188R71E473K	Murata
L1	33 nH	0603	0603CS-33NX_LU	Coilcraft
L2	1600 Ω	1810	FBMH4525HM162N-T	Taiyo-Yuden
L3	110 nH	0805	0805CS-111X_L	Coilcraft
R1	See Table 5	0603	Variable	Variable

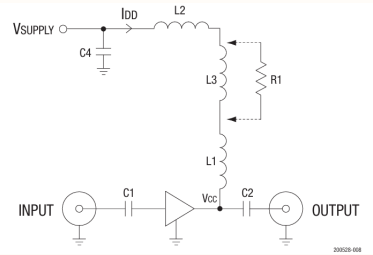

DESIGN TEAM			
Drawn by: Engineer Name	Date: DD/MM/AAAA	Cannot open file C:\Users\User\Desktop\FGA\Lab_telecom\Logo - Vertical 01.png. File does not exist.	Área Especial de Indústria e Projeção, Setor Leste, Gama-DF, Campus UnB/FGA
Revised by: Revisor Name	Date: DD/MM/AAAA		lab-telecom.unb.br/
Verified by: Verifier name		PUT THE TITLE	
Technician: Technician Name		Key Words	
Release date: DD/MM/AAAA		Size: A3 | Document Number: *.2 | Rev: X.X	
		Filename: GainBlock_16dB.SchDoc	Sheet 5.1 of 10

Revisions	
REV	Description

Power Supply

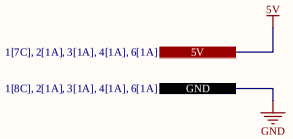

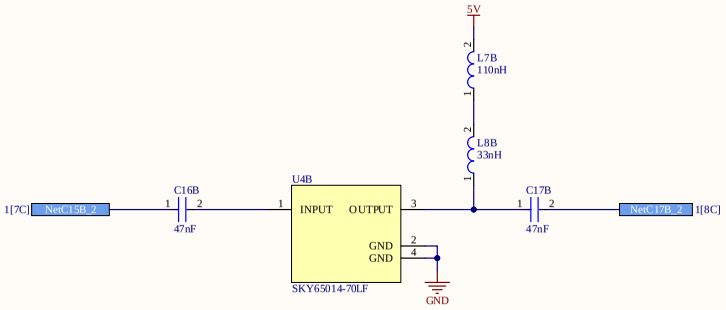

Table 5. Current Limiting Resistor Values

Supply Voltage (V)	Value of R1 (Ω)	Minimum Power Dissipation Rating (mW)
5[1]	0	-
6	10	250
7	20	500
8	30	500
9	40	1000
10	50	1000
12	70	2000

[1] To ensure that the supply current does not exceed the recommended value, a regulated current source should be used to supply the device under this condition.

Table 4. SKY65017-70LF Evaluation Board Bill of Materials (BOM)

Component	Value	Size	Part Number	Manufacturer
C1, C2, C4	47 nF	0603	GRM188R71E473K	Murata
L1	33 nH	0603	0603CS-33NX_LU	Coilcraft
L2	1600 Ω	1810	FBMH4525HM162N-T	Taiyo-Yuden
L3	110 nH	0805	0805CS-111X_L	Coilcraft
R1	See Table 5	0603	Variable	Variable

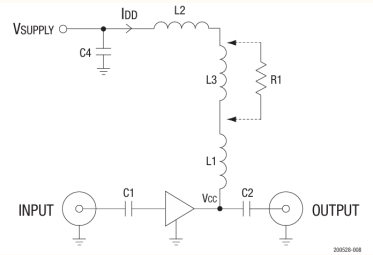

DESIGN TEAM			
Drawn by: Engineer Name	Date: DD/MM/AAAA	Cannot open file C:\Users\User\Desktop\FGA\Lab_telecom\Logo - Vertical 01.png. File does not exist.	Área Especial de Indústria e Projeção, Setor Leste, Gama-DF, Campus UnB/FGA
Revised by: Revisor Name	Date: DD/MM/AAAA		lab-telecom.unb.br/
Verified by: Verifier name		PUT THE TITLE	
Technician: Technician Name		Key Words	
Release date: DD/MM/AAAA		Size: A3	Document Number: *.1	Rev: X.X
		Filename: GainBlock_16dB.SchDoc	Sheet 5.2 of 10

Revisions	
REV	Description

Power Supply

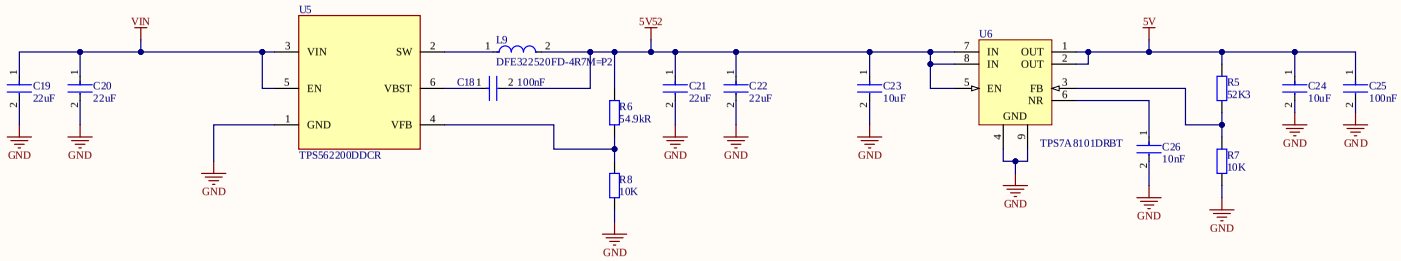

Component	Qtd.	Voltage (V)		Current (mA)	
Total Current (mA)	Power (mW)				
SKY67151-396LF	2	5	80	160	400
SKY65014-70LF	2	5	120	240	600
SKY65017-70LF	2	5	120	240	600
MAAL-010200	2	5	100	200	500
Total		420	840	2100	

DESIGN TEAM		
Drawn by: Engineer Name	Date: DD/MM/AAAA	
Revised by: Revisor Name	Date: DD/MM/AAAA	
Verified by: Verifier name		
Technician: Technician Name		
Release date: DD/MM/AAAA		

Cannot open file C:\Users\User\Desktop\FGA\Lab_telecom\Logo - Vertical 01.png. File does not exist.

Área Especial de Indústria e Projeção, Setor Leste, Gama-DF
Campus UnB/FGA
lab-telecom.unb.br/

PUT THE TITLE

Key Words

Size	Document Number	Rev
A3	*.	X.X
Filename: Power Supply.SchDoc		Sheet 6 of 10

References

[1] M.H. Chen, G.N. Tsandoulas, and F.G. Willwerth. "Modal Characteristics of Quadruple-Ridged Circular and Square Waveguides (Short Papers)". In: *IEEE Transactions on Microwave Theory and Techniques* 22.8 (1974), pp. 801–804. DOI: 10.1109/TMTT.1974.1128341.

[2] MH Chen, GN Tsandoulas, and FG Willwerth. "Modal characteristics of quadruple-ridged circular and square waveguides (short papers)". In: *IEEE Transactions on Microwave Theory and Techniques* 22.8 (1974), pp. 801–804.

[3] S.K. Dhawan. "Understanding effect of teflon room temperature phase transition on coax cable delay in order to improve the measurement of TE signals of deuterated polarized targets". In: *Conference Record of the 1991 IEEE Nuclear Science Symposium and Medical Imaging Conference*. 1991, 449–453 vol.1. DOI: 10.1109/NSSMIC.1991.258937.

[4] S.J. Skinner and G.L. James. "Wide-band orthomode transducers". In: *IEEE Transactions on Microwave Theory and Techniques* 39.2 (1991), pp. 294–300. DOI: 10.1109/22.102973.

[5] M.H. Er and B.C. Ng. "A new approach to robust beamforming in the presence of steering vector errors". In: *IEEE Transactions on Signal Processing* 42.7 (1994), pp. 1826–1829. DOI: 10.1109/78.298291.

[6] N. Fistas and A. Manikas. "A new general global array calibration method". In: *Proceedings of ICASSP '94. IEEE International Conference on Acoustics, Speech and Signal Processing*. Vol. iv. 1994, IV/73–IV/76 vol.4. DOI: 10.1109/ICASSP.1994.389873.

[7] Weimin Sun and Constantine A Balanis. "Analysis and design of quadruple-ridged waveguides". In: *IEEE Transactions on Microwave Theory and Techniques* 42.12 (1994), pp. 2201–2207.

[8] Boon C. Ng and Arye Nehorai. "Active array sensor localization". In: *Signal Processing* 44.3 (1995), pp. 309–327. ISSN: 0165-1684. DOI: https://doi.org/10.1016/0165-1684(95)00032-9. URL: https://www.sciencedirect.com/science/article/pii/0165168495000329.

[9] U. Balaji and Vahldieck. "Radial mode matching analysis of ridged circular waveguides". In: *IEEE Transactions on Microwave Theory and Techniques* 44.7 (1996), pp. 1183–1186. DOI: 10.1109/22.508660.

[10] Jia-Shen G Hong and Michael J Lancaster. *Microstrip filters for RF/microwave applications*. John Wiley & Sons, 2004.

[11] Harry L Van Trees. *Optimum array processing: Part IV of detection, estimation, and modulation theory*. John Wiley & Sons, 2004.

[12] Mary Ann Ingram et al. "LEO Download Capacity Analysis for a Network of Adaptive Array Ground Stations". In: *SERP* (2005).

[13] Sébastien Rondineau et al. "Ground stations of arrays to increase the LEO download capacity". In: *Proceedings of the 36th European Microwave Conference, EuMC* 0.September (2006), pp. 874–877. DOI: 10.1109/EUMC.2006.281059.

[14] R. Dehdasht-Heydari, H. R. Hassani, and A. R. Mallahzadeh. "A new 2-18 GHZ quad-ridged horn antenna". In: *Progress in Electromagnetics Research* 81.January 2008 (2008), pp. 183–195. ISSN: 15598985. DOI: 10.2528/PIER08010103.

[15] Brian D. Jeffs et al. "Signal Processing for Phased Array Feeds in Radio Astronomical Telescopes". In: *IEEE Journal of Selected Topics in Signal Processing* 2.5 (2008), pp. 635–646. DOI: 10.1109/JSTSP.2008.2005023.

[16] Robert J. Bauerle et al. "The use of a dielectric lens to improve the efficiency of a dual-polarized quad-ridge horn from 5 to 15 GHz". In: *IEEE Transactions on Antennas and Propagation* 57.6 (2009), pp. 1822–1825. ISSN: 0018926X. DOI: 10.1109/TAP.2009.2019929.

[17] Gordon M. Coutts, Hollis Dinwiddie, and Paul Lilie. "S-band octave-bandwidth orthomode transducer for the Expanded Very Large Array". In: *2009 IEEE Antennas and Propagation Society International Symposium*. 2009, pp. 1–4.

[18] D. I.L. De Villiers, P. Meyer, and K. D. Palmer. "Broadband offset quad-ridged waveguide orthomode transducer". In: *Electronics Letters* 45.1 (2009), pp. 60–62. ISSN: 00135194. DOI: 10.1049/el:20092887.

[19] Jonathan Landon et al. "PHASED ARRAY FEED CALIBRATION, BEAMFORMING, AND IMAGING". In: *The Astronomical Journal* 139.3 (Feb. 2010), 1154–1167. ISSN: 1538-3881. DOI: 10.1088/0004-6256/139/3/1154. URL: http://dx.doi.org/10.1088/0004-6256/139/3/1154.

[20] "ANALYSIS OF A QUADRUPLE CORNER-CUT RIDGED/VANE-LOADED CIRCULAR WAVEGUIDE USING SCALED BOUNDARY FINITE ELEMENT METHOD". In: *Progress In Electromagnetics Research M* 17 (2011), pp. 113–133. DOI: 10.2528/PIERM10122407.

[21] Gordon M. Coutts. "Wideband diagonal quadruple-ridge orthomode transducer for circular polarization detection". In: *IEEE Transactions on Antennas and Propagation* 59.6 PART 1 (2011), pp. 1902–1909. ISSN: 0018926X. DOI: 10.1109/TAP.2011.2122219.

[22] O. B. Jacobs, J. W. Odendaal, and J. Joubert. "Elliptically shaped quad-ridge horn antennas as feed for a reflector". In: *IEEE Antennas and Wireless Propagation Letters* 10.August (2011), pp. 756–759. ISSN: 15361225. DOI: 10.1109/LAWP.2011.2163050.

[23] O. B. Jacobs, J.W. Odendaal, and J. Joubert. "Quad ridge horn antenna with elliptically shaped sidewalls". In: *2011 International Conference on Electromagnetics in Advanced Applications*. 2011, pp. 259–262. DOI: 10.1109/ICEAA.2011.6046354.

[24] Krzysztof Czuba, Dominik Sikora, ISE Zembala, et al. "Overview of the RF Synchronization System for the European XFEL". In: *Proceedings of IPAC2013, Shanghai, China* (2013), pp. 3001–3003.

[25] Alex Dunning, Mark Bowen, and Yoon Chung. "Offset quad ridged ortho-mode transducer with a 3.4:1 bandwidth". In: *Asia-Pacific Microwave Conference Proceedings, APMC* (2013), pp. 146–148. DOI: 10.1109/APMC.2013.6695219.

[26] Simon Henault et al. "A Methodology for Mutual Coupling Estimation and Compensation in Antennas". In: *IEEE Transactions on Antennas and Propagation* 61.3 (2013), pp. 1119–1131. DOI: 10.1109/TAP.2012.2229955.

[27] Ockert B. Jacobs, Johann W. Odendaal, and Johan Joubert. "Quad-Ridge Horn Antenna With Elliptically Shaped Sidewalls". In: *IEEE Transactions on Antennas and Propagation* 61.6 (2013), pp. 2948–2955. DOI: 10.1109/TAP.2013.2254436.

[28] Hema Singh, H. L. Sneha, and R. M. Jha. "Mutual Coupling in Phased Arrays: A Review". In: *International Journal of Antennas and Propagation* 2013.1 (2013), p. 348123. DOI: https://doi.org/10.1155/2013/348123.

[29] Theunis S. Beukman et al. "A quadraxial feed for ultra-wide bandwidth quadruple-ridged flared horn antennas". In: *The 8th European Conference on Antennas and Propagation (EuCAP 2014)*. 2014, pp. 3312–3316. DOI: 10.1109/EuCAP.2014.6902537.

[30] Theunis Steyn Beukman. "Modal-based design techniques for circular quadruple-ridged flared horn antennas". PhD thesis. Stellenbosch: Stellenbosch University, 2015.

[31] Ivan Dokmanic et al. "Euclidean Distance Matrices: Essential theory, algorithms, and applications". In: *IEEE Signal Processing Magazine* 32.6 (2015), pp. 12–30. DOI: 10.1109/MSP.2015.2398954.

[32] Simon Henault and Yahia Antar. "Unifying the Theory of Mutual Coupling Compensation in Antenna Arrays". In: *IEEE Antennas and Propagation Magazine* 57.2 (2015), pp. 104–122. DOI: 10.1109/MAP.2015.2414514.

[33] Constantine A Balanis. *Antenna theory: analysis and design*. John wiley & sons, 2016.

[34] Theunis S. Beukman et al. "Modal-Based Design of a Wideband Quadruple-Ridged Flared Horn Antenna". In: *IEEE Transactions on Antennas and Propagation* 64.5 (2016), pp. 1615–1626. DOI: 10.1109/TAP.2016.2537363.

[35] Orfanidis Sophocles. *Electromagnetic Waves and Antennas*. 2016.

[36] Jin Fan et al. "Design of wideband quad-ridged waveguide orthomode transducer at L-band". In: *Progress In Electromagnetics Research C* 72.January (2017), pp. 115–122. ISSN: 15309681. DOI: 10.2528/PIERC17010802.

[37] Abdullah Genc et al. "The comparison of the characteristics of the double-ridged horn antennas depending the geometry of ridge profiles for wideband application". In: *Progress in Electromagnetics Research Symposium* October 2020 (2017), pp. 1553–1557. ISSN: 19317360. DOI: 10.1109/PIERS.2017.8261994.

[38] Ghoncheh Jazani and Abbas Pirhadi. "Design of dual-polarised (RHCP/LHCP) quad-ridged horn antenna with wideband septum polariser waveguide feed". In: *IET Microwaves, Antennas and Propagation* 12.9 (2018), pp. 1541–1545. ISSN: 17518733. DOI: 10.1049/iet-map.2017.0611.

[39] Alexander W. Pollak and Michael E. Jones. "A Compact Quad-Ridge Orthogonal Mode Transducer with Wide Operational Bandwidth". In: *IEEE Antennas and Wireless Propagation Letters* 17.3 (2018), pp. 422–425. ISSN: 15361225. DOI: 10.1109/LAWP.2018.2793465.

[40] Bernard F Burke, Francis Graham-Smith, and Peter N Wilkinson. *An introduction to radio astronomy*. Cambridge University Press, 2019.

[41] Christophe Granet et al. "A wide-band 4-12.25 GHz feed system for the Australia telescope 22m-diameter antenna". In: *Proceedings of the 2019 21st International Conference on Electromagnetics in Advanced Applications, ICEAA 2019* (2019), pp. 600–605. DOI: 10.1109/ICEAA.2019.8879140.

[42] Falin Oktafiarri et al. “Dual-polarized wideband horn antenna with lower frequency extension for microwave imaging application”. In: *2019 PhotonIcs & Electromagnetics Research Symposium-Spring (PIERS-Spring)*. IEEE. 2019, pp. 930–934.

[43] Yue Ma et al. “A 10: 1 bandwidth cryogenic quadruple-ridged flared horn design for reflector antennas in radio astronomy”. In: *IEEE Access* 8 (2020), pp. 81101–81115.

[44] Claudia Vasanelli et al. “Calibration and Direction-of-Arrival Estimation of Millimeter-Wave Radars: A Practical Introduction”. In: *IEEE Antennas and Propagation Magazine* 62.6 (2020), pp. 34–45. DOI: 10.1109/MAP.2020.2988528.

[45] Laila Marzall et al. “Broadband Small-Aperture High-Gain Ridge Horn Antenna Array Element”. In: *IEEE Antennas and Wireless Propagation Letters* 20.5 (2021), pp. 708–712. ISSN: 15485757. DOI: 10.1109/LAWP.2021.3060779.

[46] Bernard Sklar. *Digital communications: fundamentals and applications*. Pearson, 2021.

[47] Folin Oktafiani, Effrina Yanti Hamid, and Achmad Munir. “Wideband Dual-Polarized 3D Printed Quad-Ridged Horn Antenna”. In: *IEEE Access* 10 (2022), pp. 8036–8048. ISSN: 21693536. DOI: 10.1109/ACCESS.2022.3143164.

[48] Peng Yang, Bei Hong, and Wei Zhou. “Theory and Experiment of Array Calibration via Real Steering Vector for High-Precision DOA Estimation”. In: *IEEE Antennas and Wireless Propagation Letters* 21.8 (2022), pp. 1678–1682. DOI: 10.1109/LAWP.2022.3177468.

[49] Téssio Perotti Arruda, Rafael R. L. Benevides, and Sébastien R. M. J. Rondineau. “Minimization of Ground Stations Distribution that Maximizes LEO Satellite Link Coverage Over Any Given Territory”. In: *2023 Workshop on Communication Networks and Power Systems (WCNPS)*. 2023, pp. 1–7. DOI: 10.1109/WCNPS60622.2023.10344834.

[50] Ian Goode and Carlos E. Saavedra. “3D printed variable aperture horn with modular ridges”. In: *Journal of Physics Communications* 7.5 (2023). ISSN: 23996528. DOI: 10.1088/2399-6528/acd167.

[51] Doug Henke et al. “A Turnstile Quad-Ridge Orthomode Transducer (OMT) for Octave-Bandwidth Receiver Front-Ends (24–51 GHz)”. In: *IEEE Transactions on Microwave Theory and Techniques* 71.11 (2023), pp. 4906–4921. DOI: 10.1109/TMTT.2023.3267544.

[52] Thomas Whittaker et al. “3D Printing Materials and Techniques for Antennas and Metamaterials: A survey of the latest advances”. In: *IEEE Antennas and Propagation Magazine* 65.3 (2023), pp. 10–20. DOI: 10.1109/MAP.2022.3229298.

[53] Téssio Perotti Arruda, Sébastien R. M. J. Rondineau, and Rafael R. L. Benevides. “Optimizing Static Antenna Arrays for Constant Power Levels in Satellite Communications”. In: *2024 Workshop on Communication Networks and Power Systems (WCNPS)*. 2024, pp. 1–7. DOI: 10.1109/WCNPS65035.2024.10814225.

[54] Óscar García-Pérez et al. “A Modular Approach for the Design of Quadruple Ridged Flared Horn Antenna Feeds”. In: *IEEE Access* 12 (2024), pp. 69642–69651. DOI: 10.1109/ACCESS.2024.3401410.